MODELING THE VACUUM ASSISTED RESIN TRANSFER MOLDING (VARTM) PROCESS FOR FABRICATION OF FIBER/METAL HYBRID LAMINATES

By

Goker Tuncol

A DISSERTATION

Submitted to
Michigan State University
in partial fulfillment of the requirements
for the degree of

DOCTOR OF PHILOSOPHY

Mechanical Engineering

2010

ABSTRACT

MODELING THE VACUUM ASSISTED RESIN TRANSFER MOLDING (VARTM) PROCESS FOR FABRICATION OF FIBER/METAL HYBRID LAMINATES

By

Goker Tuncol

Fiber metal laminates (FMLs) are hybrid materials consisting of alternating layers of metallic sheets and fiber-reinforced polymeric-resin composites. FMLs combine some of the best properties of the metal and the composite parts making them highly attractive for aerospace applications. FMLs are currently being manufactured under elevated temperatures and pressures in a compression press or an autoclave. These fabrication processes are expensive and the part size is limited by the size of the press or autoclave. NASA Langley Research Center has developed a process which can be used to manufacture FMLs by the cost effective Vacuum Assisted Resin transfer Molding (VARTM) process. The objective of this study was to investigate the manufacturability of the FMLs using low cost liquid composite molding techniques but with the same level of quality of FMLs fabricated in an autoclave.

A flow visualization fixture of the VARTM/FML process was constructed and used to observe the resin infiltration process. The results of the flow visualization experiments were analyzed and compared with the predictions of a VARTM process simulation model. The simulation model of the hybrid preform structure of the FMLs was developed using the commercial software package FLUENT. The model used a transient two phase volume of fluid (VOF) method to track the resin

progression. The model was used to predict the resin flow patterns and infiltration times of the hybrid FML structure during the resin infusion stage of the VARTM process. A variation of the VARTM process, the Controlled Atmospheric Pressure Resin Infusion (CAPRI) process, was also considered.

Compaction and permeability characterization studies were performed for the preform materials used in the FML structures under different testing conditions. The pressure vs. fiber volume fraction data was fit to mathematical models. Similarly, the permeabilities in the principal material directions were measured and the fiber volume fraction vs. permeability data was fit to mathematical models. The mathematical models were used to determine the input parameters of the simulation model such as initial volume fraction, permeability and the model constants for a developed user defined compaction model.

Parametric studies were performed with the simulation model to explore the effects of various model inputs on the flow patterns of the FML structures. An attempt was made to further improve the model by the integration of a compaction model that could dynamically update the permeability and thickness of the preform with time. The flow patterns and the infiltration times predicted by the simulation model agreed very well with the flow patterns and times recorded during the infiltration and manufacture of an actual FML panel. The results of this study showed that FML parts can be successfully infiltrated when flow pathways were included in the hybrid preform structure. Thus, this study demonstrates the manufacturability of high quality FML parts using the VARTM and CAPRI processes.

I dedicate this work to the love of my life B.T. despite all the tough times.
Whatever the life brings, I believe that we can make it through.

ACKNOWLEDGEMENTS

I would like to preeminently thank my advisor Dr. Alfred Loos for his help and guidance in my Ph.D. research study. I would also like to thank Dr. Dahsin Liu, Dr. K. Jayaraman and Dr. Sharon Xiao for their participation in the thesis committee; Dr. Rehan Umer and Kai Long for sharing their valuable knowledge with me and for all kind of support they gave during the laboratory experiments and the simulation studies.

Finally, I want to thank my parents, Tülay and Vural Tunçol, my sister and brother in law, Gökçen and Melih İşliel and my dearest nephew Göksun İşliel for their endless love and support.

TABLE OF CONTENTS

LIST OF TABLES

LIST OF FIGURES

Chapter 1

INTRODUCTION

1.1 Fiber Metal Laminates

Fiber metal laminates (FMLs) are fabricated by stacking alternate layers of metallic sheets and fiber-reinforced polymeric-matrix prepreg plies [1]. A typical lay-up is shown in Figure 1.1. The hybrid layup is then processed under elevated temperature and pressure to consolidate the laminate and cure the polymer resin which bonds the fiber layers to the metallic sheets [1-2]. FMLs have mechanical and environmental properties that are superior compared with monolithic metal alloys or fiber reinforced polymer matrix composite laminates [1].

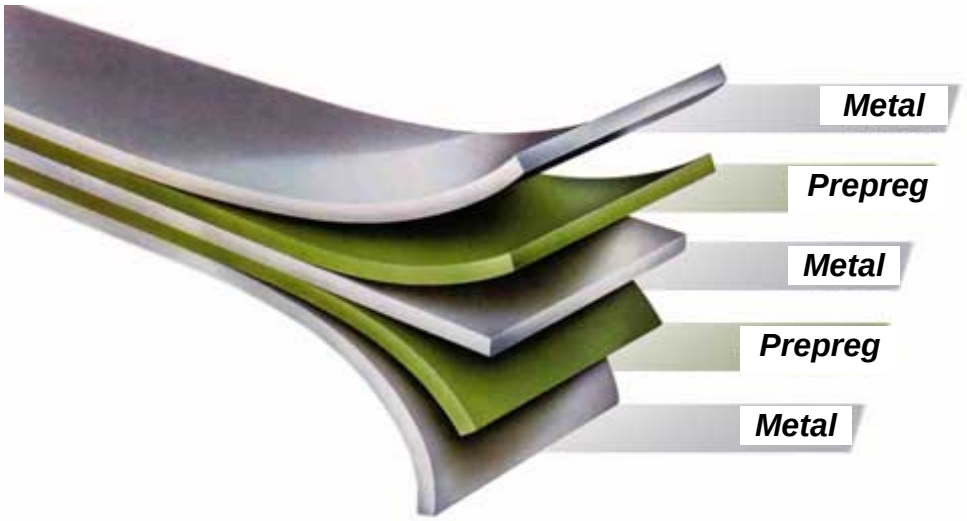

Figure 1.1 A typical lay-up of a Fiber Metal Laminate (FML). (For interpretation of the references to color in this and all other figures, the reader is referred to the electronic version of this dissertation).

Two common FMLs include ARALL™ and GLARE™. ARALL™ uses unidirectional aramid fibers while GLARE™ uses either unidirectional or biaxial high strength glass fibers. Both laminates use aluminum alloys for the metallic sheets. GLARE™ is one of the most successful FMLs, patented by Akzo Nobel in 1987 and is being currently used in the manufacture of the Airbus A380 [3]. It has also recently been certified and approved by the Federal Aviation Administration (FAA) and by European Aviation Authorities.

FMLs are currently manufactured by placing the layup of metallic sheets and prepreg plies in a mold and exposing the structure to elevated temperature and pressure in a compression press or an autoclave. These manufacturing methods result in well consolidated structures with good bonding between the metallic sheets and the fiber-reinforced composite [1]. However, these fabrication processes are expensive and the part size is limited by the size of the press or autoclave. The objective of this study is to investigate the manufacture of Fiber Metal Laminates (FMLs) by the low-cost Vacuum Assisted Resin Transfer Molding (VARTM) process. The overall goal is to produce FMLs at a reduced cost but with the same level of quality as FMLs fabricated in an autoclave.

NASA LaRC has developed a process for the manufacture of FMLs by VARTM [5, 6]. A hybrid preform is created by stacking alternating layers of the metal sheets and dry woven fabrics. The preform is placed on the tool and bagged as shown in Figure 1.2.

Resin is infused into the dry woven fabric and will bond the metal sheets to the reinforcing fiber layers when cured. A distribution medium is commonly incorporated on top the lay up to

enhance the resin infiltration process. This variation of the VARTM process is known as the SCRIMP® process [7,8]. With the addition of the highly permeable distribution medium, resin rapidly flows over the surface of the part and is pulled into the hybrid preform by the vacuum source. Since resin flow is primarily in the through-the-thickness or transverse direction, resin pathways must be inserted into the metal sheets to allow resin to infiltrate into the dry woven fabric layers as depicted in Figure 1. The size and shape of the pathways must be large enough to permit resin to flow into and wet-out the woven fabrics, but small enough as to not comprise the structural performance of the FML.

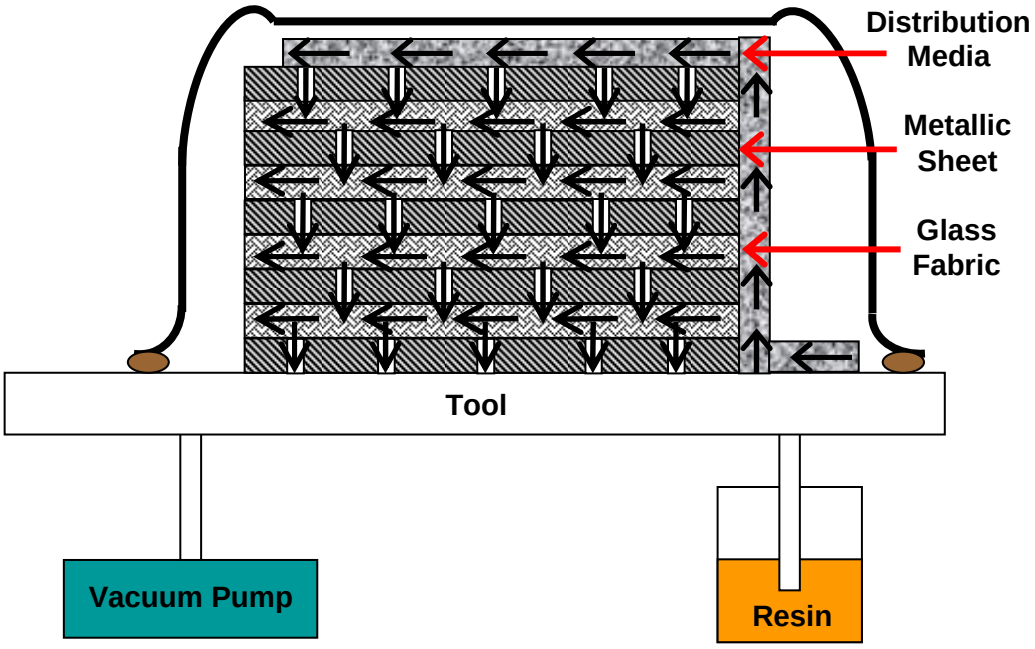

Figure 1.2 Diagram of the FML VARTM process

1.2 Research Objectives

In this study, a combined experimental and numerical study was performed to investigate the manufacture of FMLs by the Vacuum Assisted Resin Transfer Molding (VARTM) process. A simulation model of the hybrid preform structure of the FMLs was developed using the commercial software package FLUENT. The model was used to predict the resin flow into the glass fabrics of the hybrid perform during the resin infusion stage of the VARTM process.

A flow visualization fixture was constructed to allow resin flow patterns to be observed at the both top and bottom surfaces of the preform during infiltration. The visualization fixture is identical to the VARTM fixture currently used to manufacture FMLs except for the changes noted below which were necessary to observe the fluid during infiltration. A clear, scratch resistant, polycarbonate tool plate was used in place of the metal tool plate. Acetate, clear plastic film was used in place of the aluminum sheet. Resin pathways were machined into the acetate films to permit resin flow through the films during processing. The remaining components and all dimensions of the visualization fixture were identical to the VARTM fixture. Mounted below the polycarbonate tool was a mirror which was used to observe the resin flow along the bottom surface of the preform. Use of the mirror allows the video camera to simultaneously record the flow fronts on both the top and bottom surfaces of the preform. The flow visualization data were compared with the results of the simulation model and were used to assess if FMLs can be successfully manufactured by the VARTM process.

The objectives of this study are:

- Developing a science based simulation model of the VARTM process for fabrication of FMLs
- Characterizing fabric preforms and preform materials
    - Measuring the compaction behavior under several test conditions and fit data to mathematical models
    - Measuring the permeabilities in the principal material directions and fit data to mathematical models
- Performing flow visualization studies to verify model predictions

1.3 Organization of the Thesis

In this study, the manufacture of fiber metal laminates by the low-cost Vacuum Assisted Resin Transfer Molding (VARTM) process was investigated by performing experimental characterization tests and using the resulting data as inputs to the developed simulation model. The organization of the chapters can be given as follows: A general introduction to FMLs and the VARTM process is given in the current Chapter 1. The literature survey on preform modeling, compaction and permeability is given in Chapter 2.

Flow visualization tests are discussed in Chapter 3. In this chapter, flow visualization fixture components and the procedure for machining resin pathways are described. The test procedures are described in detail and the results of the flow visualization experiments are presented with different testing configurations. Infiltration of FMLs using the VARTM technique and the flow characteristics are analyzed.

Preform compaction characterization is discussed in Chapter 4. Results of the compaction tests performed for S2 glass fabrics are presented and verified with the compaction data of multi axial warp knit (MAWK) carbon fabrics. Static and dynamic compaction test procedures and analysis of compaction tests under different testing conditions are discussed in Chapter 4. Mathematical models fit to the compaction data of several preform materials are shown. In Chapter 5, preform permeability characterization is discussed. Permeability measurement and calculation procedures for several preform materials including hybrid preforms are described. Mathematical models based on the permeability measurements are shown.

In Chapter 6, a flow simulation model of the VARTM process that was developed for the manufacture of FMLs is presented. Mathematical models suggested in Chapters 4 and 5 are used to determine the input parameters for the flow simulation model. The simulation model results are compared and verified with the results of the flow visualization tests given in Chapter 3. The findings and conclusions of this study are summarized in Chapter 7.

Chapter 2

Literature Survey

2.1 VARTM Process

Liquid Composite Molding (LCM) is one of the most cost effective and commonly used composite materials manufacturing techniques [9]. In LCM processes, the basic principle is to inject resin into stationary fabric preform and saturate all gaps between the fibers with resin before the curing (gelation) starts. Resin Transfer Molding (RTM) is a typical LCM process, in which a fabric preform is placed inside a mold cavity and then the mold is sealed and closed. Resin is injected into the mold cavity to saturate the fabric preform. After the resin cures, the mold is opened and the composite part is taken out [9].

Vacuum Assisted Resin Transfer Molding (VARTM) is a variation of the RTM process. Originally, vacuum was introduced to the RTM mold to lessen the required injection pressure and remove air voids in the final processed composite laminate [10]. The process was developed further by marine composite hull manufacturers at Seemann Composites, Inc. by eliminating the rigid top portion of the mold and replacing it with a flexible polymer vacuum bag. The woven preform could be placed on a rigid tool having the shape of the desired composite part. The fabric is sealed to the tool with the vacuum bag and a sealant tape. The bagged part is then evacuated via a vacuum port which protrudes from the sealed bag. A typical VARTM lay up is shown in Figure 2.1.

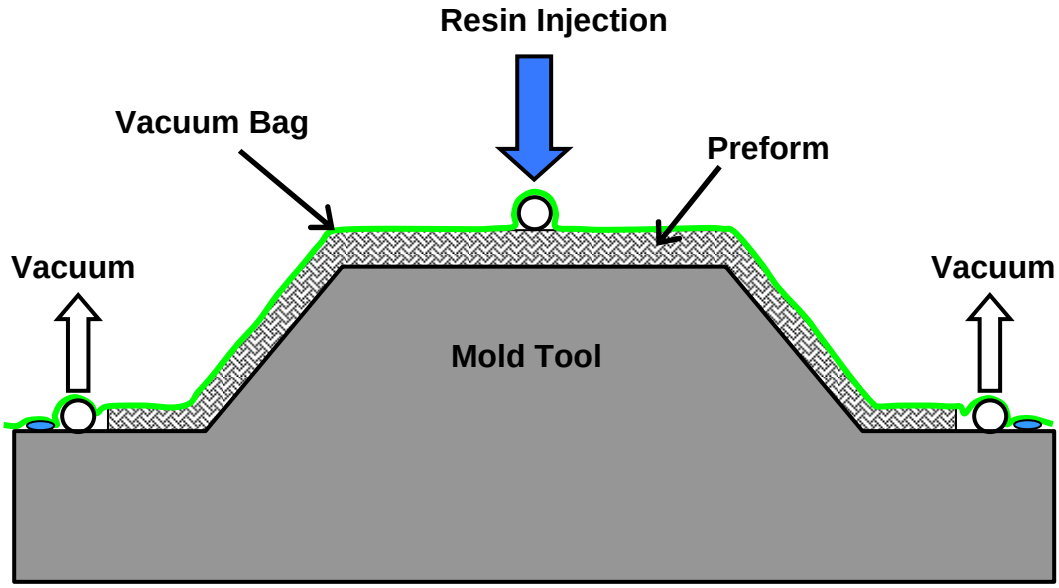

Figure 2.1 Schematic diagram of the VARTM process.

With the part fully evacuated, the compaction pressure on the preform is approximately 1 atm. Using low viscosity resins, typically less than 0.5 Pa·s, the resin is introduced to the evacuated preform via a resin port, or multiple resin ports depending on the size and shape of the part. The resin is forced into the preform using only atmospheric pressure, due to the difference in pressure between the evacuated preform and the resin contained outside of the bag at 1.0 atm (101.5 kPa).

Because of the low injection pressure and resulting long fill-times, Seemann™ invented a means by which the resin could be transferred more quickly into the compacted preform. A distribution media layer, or SCRIMP® cloth for Seemann Composite Resin Injection Molding Process [7,8], is placed on the top surface of the fiber preform within the vacuum bag. The SCRIMP® cloth has a high permeability compared to typical fiber preforms or reinforcing fibers. This allows resin to flow quickly across the surface of the part and then filter down through the thickness of the dry fabric. This is ideally suited for many composite parts, such as boat hulls or the skin of an

aircraft wing, because the thickness dimension is much smaller than the length and width dimensions. This allowed entire boat hulls to be fabricated in one infusion step with resin entering the part from various resin port locations [11]. The composites are infused without any externally supplied pressure and the part can be cured either at room temperature or in an oven, depending on the resin system. The cost of matched metal tooling is eliminated and, since the entire part is contained within a vacuum bag, there is little exposure to the volatiles involved in handling of other raw materials, such as prepreg. Proper degassing of the resin system and a leak-free vacuum bag ensures high quality, void-free laminate fabrication. Because VARTM is an infusion process, a high level of part integration can be achieved without the tremendous tooling costs associated with prepreg and autoclave manufactured composites [12]. This also reduces the number of fasteners that are necessary in the assembly of the same metallic structure. These advantages found in the SCRIMP® process make it attractive for the fabrication of large composite structures [11].

For many years, VARTM has been used to fabricate structural composites for the marine and infrastructure industries [11, 12]. These composites were often fabricated using woven glass preforms infiltrated with vinyl ester resin and the resulting structures had fiber volume fractions around 50% and void contents of 2 – 3%. Recent investigations have shown that it is possible to fabricate aircraft-quality composite structures by the VARTM process [10]. The high performance composite parts were manufactured using carbon fiber preforms and low viscosity epoxy resins to produce structures having fiber volume fractions approaching 60% and void contents less than 1% [13].

2.2 VARTM Modeling

Composite fabrication processes for new materials and applications are commonly designed empirically by trial-and-error methods. This approach to process development is time-consuming and expensive. In addition, with an empirical approach it is impossible to evaluate all the resin and preform material properties that must be known for successful completion of the process. Analytical simulation models are clearly far superior alternatives for determination of a processing cycle that will result in a void free and fully consolidated composite structure. Accurate inputs are essential for successful simulation models that are capable of relating processing conditions and the constituent material properties to the thermal, physical, chemical, rheological and mechanical processes that occur in the composite during fabrication.

Johnson et al. [14] developed an active control system that relies on locally heating resin to decrease its viscosity and increase the preform permeability. By doing so, a more uniform flow front, higher flow front velocity and lower filling time were achieved. Heating of resin was adjusted by inductions coils placed inside the mold. At any time instant, the flow front location was sensed by a camera and was fed to the controller. This information was used to determine the target coil position and amount of heating to be supplied to the resin. This strategy for coil positioning was shown to be most effective in locally reducing the viscosity and improving flow uniformity and flow rate. The method was shown to be useful in fabricating composite panels without void entrapment or premature resin gelation, while reducing the fill time and resin wastage.

Correia et al. [15] discussed the similarities between the RTM and VARTM processes. RTM simulations were coupled with auxiliary compaction and permeability models to estimate the filling time and the fiber volume fraction distribution in the VARTM process. LIMS [16] software was used in their analysis. Using LBASIC script, the RTM LIMS model was modified to locally update thickness, porosity and permeability as a function of compaction pressure. This was done by employing an iterative finite difference method. Apart from the simulation model, a power law compaction model relating compaction pressure to volume fraction and a permeability model based on Kozeny-Carman equation to relate permeability to volume fraction were used. 1D flow comparisons for VARTM and RTM processes were made and a proportionality constant for the VARTM case was introduced since it was found out that the filling times in the one dimensional VARTM filling case were directly proportional to those in the RTM case by a constant.

Chen et al. [17] introduced an equivalent permeability method to reduce the computation cost of 3D CV/FEM VARTM simulations for large parts. It was noted that in many cases, the distribution media (high permeable medium-HPM) used in the VARTM process is much thinner than the preform, causing a high aspect ratio in the 3D CV/FEM simulations, which results in long computation times and poor convergence. To avoid this, Chen and coworkers increased the thickness of the HPM layer and determined an equivalent permeability while keeping the flow pattern and pressure gradients same as in the original case. The equivalent permeability values for the thicker HPM layers were found to be smaller than the original case and when the results were compared for the original and equivalent systems, the CPU time diminished as much as 96% while the filling time varied by 3% only.

Dong [18] noted that 3D models are needed when modeling the VARTM process due to the existence of the distribution or high permeable medium (HPM) in the process. However, it was noted that 3D models are limited due to their computational cost especially when used for the fabrication of large parts. A set of dimensionless process variables (e.g. filling time) were introduced for computational purposes and a statistical model (response surface method) was used to identify significant process variables. Validated with experiments show that the model accuracy was not very high (within 15%), however, the computation time was reduced by 99%. Thus, it was concluded that the proposed statistical model can be used as a guideline in the early stages of the VARTM process design and optimization.

Grujicic et al. [19] noted that tool plate heating can be useful to increase infiltration and reduce preform infiltration time compared to room temperature (isothermal) infiltration. A CV/FEM analysis of the preform infiltration was made by the simultaneous solution of the continuity equation, energy conservation equation and evolution equation for the degree of polymerization. The model was applied to simulate the infiltration of a rectangular carbon fiber based preform with an epoxy resin and to optimize the VARTM process with respect to minimizing the preform infiltration time. The results suggested that by proper selection of the ramp/hold thermal history of the tool plate, the preform infiltration time can be reduced relative to the room-temperature infiltration time. It was concluded that this infiltration time reduction was due to the thermal-thinning and thus the decrease in viscosity of the ungelled resin.

Li et al. [20] studied the effects of thickness gradient and local material variations in the VARTM process. An existing RTM simulation code was modified and implemented with an

auxiliary compaction model to account for the thickness change in the VARTM process at the moment the infusion stage is finished. The suggested model covered all VARTM stages including the infusion and curing stages. The computational procedure was as follows: First, the initial conditions (resin viscosity, porosity and permeability) were entered. The flow model calculated the time and compaction pressure for the next time step. Then, using the previous step result, viscosity and degree of cure were calculated from the resin model, and the compaction model determined the thickness, volume fraction, porosity and permeability to be used in the next iteration. If the viscosity or cure degree exceeded the limit values, the model outputs the final thickness, or if not the model moves on to the next step until the resin stops flowing.

Song et al. [21] studied analytical modeling of resin infusion in the VARTM process. The model targeted predicting the pressure and thickness distribution during resin infusion. Compaction behavior of the preform was investigated experimentally and was utilized in the modeling. Besides the analytical modeling, experimental and numerical studies were carried out to validate the analytical results. It was found that the analytic results compare reasonably well with the numerical and experimental results, however with some limitations. The analytical model predicted a slower flow front advancement in the bottom preform layer when compared to the experiments. This was due to the fact that the model considered the transverse flow only in the flow front region. In reality, the transverse flow took place throughout the whole preform since a pressure difference existed between the neighboring layers behind the flow front region.

Yoon et al. [22] used a homogeneous preform system to reduce the complexity of flow modeling in the VARTM process with a distribution media and enabling the application of similar models

for large scale parts. First, a mass-average approach was developed to reduce the number of dimensions that needs to be modeled (e.g., 3D was reduced to 2D in-plane and 2-D cross section was reduced to a 1-D flow problem). The total mass of resin to be infused in each case (2D and 1D cases) was made equal to each other. Here, D is the length of the saturated region where the flow is 1D in the x direction with Darcy velocities of U_1 in high permeable media (HPM) and U_2 in low permeable media (LPM), respectively. d is the length of the flow front region where there is transverse flow (y direction) from HPM to LPM. S is the length of average resin progression in the flow front region. To determine the flow front locations on the HPM top and LPM bottom surfaces, a reconstruction method was followed after the mass average approach. In this method, the flow patterns were reconstructed using the flow data obtained from the homogenous model with an analytic solution of the flow front shape in the out-of-plane direction. Average flow front locations and the flow front patterns were investigated by numerical analysis, which validated the two methods employed. The mass-average and reconstruction approaches successfully estimated the resin flow locations and patterns with respect to time and significantly reduced complexity in modeling complex geometries as well as computational costs. However, the application of the two methods was quite involved and limited to the setup/configuration used.

Govignon et al. [23] used a one dimensional Finite Element simulation of the resin infusion process addressing the pre-filling, filling and post-filling stages during the VARTM process. The results showed potential for accurately predicting the fiber volume fraction in the final part, as well as simulating different injection strategies (i.e. clamping of the inlet before the flow front reaches the end of the preform, or changing vacuum pressures during post-filling). It was noted that the ability to simulate applied post-filling conditions may lead to an optimization of the

pressure parameters and choice of brake material (i.e. placed between the end of the preform and the vent), increasing part quality and control of fiber volume fraction while reducing cycle times. The simulation model included a compaction model for the chopped strand mat (CSM) preform which was generated using the empirical multiple power law model previously developed by Robitaille [24].

Thus, a successful VARTM simulation model requires the compaction and permeability behavior of the reinforcing fiber as one of the major inputs so that it can accurately predict the change in preform thickness, fiber volume content and preform permeability throughout the process. In the following sections, a summary of the literature regarding the experimental techniques used to measure preform compaction and permeability will be presented.

2.3 Compaction

Two important characterization experiments, *preform compaction characterization* and *preform permeability characterization*, are required in order to construct an accurate model of the VARTM process. These are material dependent properties and must be measured for the preforms used in the process. In this section, a summary of the literature regarding the experimental techniques used to measure preform compaction will be presented.

In literature, there are numerous studies about compaction of fabrics used in the composite materials manufacturing. Earlier studies on fiber bundles by Gutowski and colleagues [25-28] suggested a useful analytical compaction model that served as a reference point to many other

following researchers. Their model revealed that the compaction response of a lubricated fiber bundle is a combination of both elastic and viscous deformation. They've found out that a unique relationship exists between applied load on the fibers and their resulting deformation. This relationship holds at a particular state or at an equilibrium state. Fiber deformation significantly affects the process parameters such as permeability and resin pressure as well as it also affects the resulting characteristics such as fiber volume fraction and the void content.

Li et al. [29] proposed a method to measure the compaction curve and the saturated transverse permeability as a function of fiber volume fraction. The fiber bed between two platens was compressed with a constant compaction pressure rate. Change in fiber bed thickness was measured using dial indicators and then converted into fiber volume fraction. The effects of type of the impregnating fluid, initial fiber volume fraction, and the lay-up type on the compaction behavior were investigated. It's been concluded that higher initial volume fractions result in higher overall compressibility and different lay-up configurations have a significant impact on the compaction behavior. In addition, it's been found that Gutowski's compaction model [25-28] can be used to adequately fit the experimental data for compaction.

Hubert et al. [30], following a similar approach to Li et al. [29], used a servo hydraulic testing machine to compact saturated fiber beds under applied temperature and resin flow. Displacement and load were measured at specified increments to get the fiber bed compaction curve. Load relaxation was also considered. A finite element model was used to simulate the uniaxial compaction of the preforms at different temperatures and it's been found that simulation results closely match with the experimental results.

Schuster et al. [31] investigated the effects of different sewing parameters on the compaction behavior of preforms. For the compaction experiments, they used a steel frame and a stamp attached to it acting as the crosshead. Force and strain were monitored by the load cell and an LVDT. The compaction test device was controlled by LabVIEW. A digital camera with a microscopic lens was used for monitoring the deformation of stitch holes under compression. It was shown that preform compaction behavior changes with the density of the seam patterns and compaction causes a reduction in the size of stitch holes, which in turn affects the lateral elasticity of the preforms. The extent of reduction was correlated with the sewing parameters and stress-strain curves gathered from the compaction experiments.

Buntain and Bickerton [32] used a two piece circular mold attached to an Instron testing machine to monitor the molding (tooling) forces during resin transfer molding (RTM) and injection/compression molding (I/CM) processes. The thickness of the mold cavity was monitored using an L-Gage laser sensor. Both wet and dry tests were performed at constant compaction speeds. A schematic diagram of their setup is shown in Figure 2.2. They noted that the L-Gage measurements were necessary since the crosshead displacement data recorded by the machine was unable to record and take the deformation of the load cell into account whereas the L-Gage sensor can. Force data was analyzed and compared by changing the process parameters; compression speed and resin injection rate for two types of E-glass. Results varied depending on the preform and process type. Clamping forces were dominated by the fluid pressure in one preform type whereas they were dominated by preform compaction forces in the other type.

Relaxation and lubrication phenomena were also discussed and were attributed to the non-elastic nature of the fabrics.

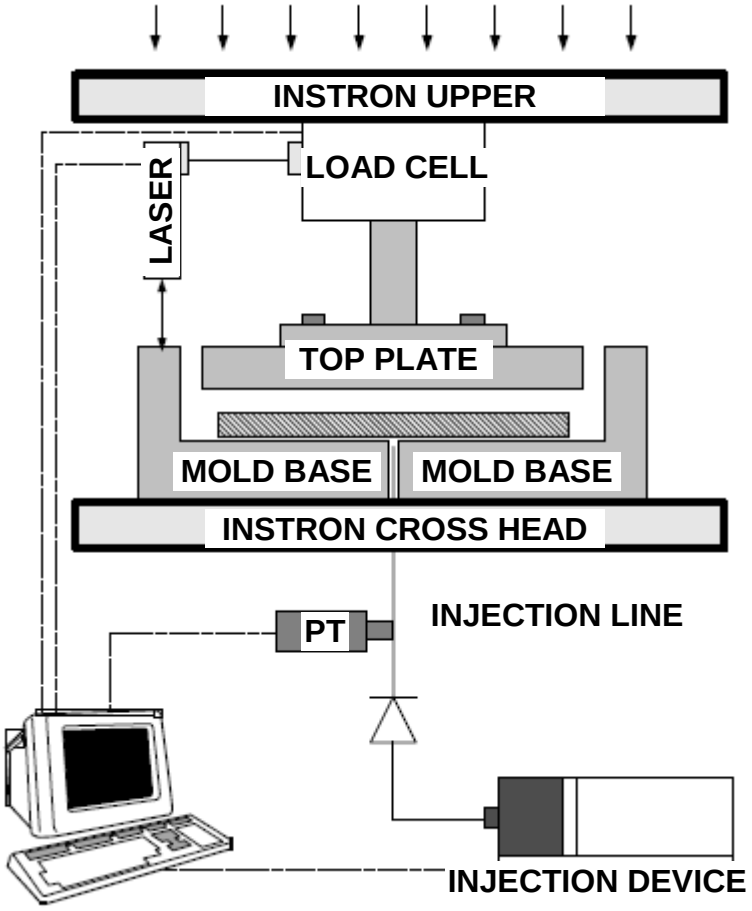

Figure 2.2 The experimental set up of Buntain and Bickerton [32].

In a similar study, Bickerton and Buntain [33] performed tests on wet and dry fabrics to investigate the compaction response. They performed dynamic tests by compressing preform samples at a constant speed. It was shown that compaction response is composed of elastic, viscous and plastic components. These involve stress relaxation, lubrication by the wetting fluid and permanent deformation. They concluded that an accurate force analysis requires the characterization of the compaction response with these components and this is especially

significant for flexible molding processes such as the Vacuum Assisted Resin Transfer Molding (VARTM).

Kelly et al. [34] studied the viscoelastic response of saturated and dry fibrous materials using a similar approach to that of Buntain and Bickerton [32-33]. Sample preforms were placed between two parallel plates mounted in a testing machine. The upper plate was fixed while the lower plate mounted on the moving crosshead holds the specimens to be compacted. The applied force and deflection of the upper plate were recorded simultaneously. Both circular and square preforms were tested. Stress was calculated and plotted with respect to time at different fiber volume fractions. A single non-linear viscoelastic model that takes compaction and relaxation phases into account was developed and was verified with experimental data. However, this model did not cover the hysteresis (permanent deformation) phenomenon.

Somashekar et al. [35] focused on the non-elastic compression deformation of dry glass fiber reinforcements and proposed an alternative approach to viscoelastic models. The experimental compaction setup is shown in Figure 2.3. Sample preforms were placed on top of a moving crosshead and were compacted against a fixed platen mounted on the load cell of a testing machine. An aluminum plate was placed on top of the preforms to create an initial preload and also a reference to determine the thickness change. Thickness recordings were made using two L-gage laser sensors. Tests were performed at constant crosshead speed. Somashekar et al. [35] concluded that there is a significant amount of permanent deformation in the preforms due to the non-elastic nature of the compaction process. Measured compaction deformation data were broken down into different phases, namely: elastic spring back, time dependent recovery and

permanent deformation. The total amount of deformation was plotted for each of the three phases with respect to other variables such as compaction stress, material type, fiber volume fraction, number of compaction cycles, number of layers and compaction speed.

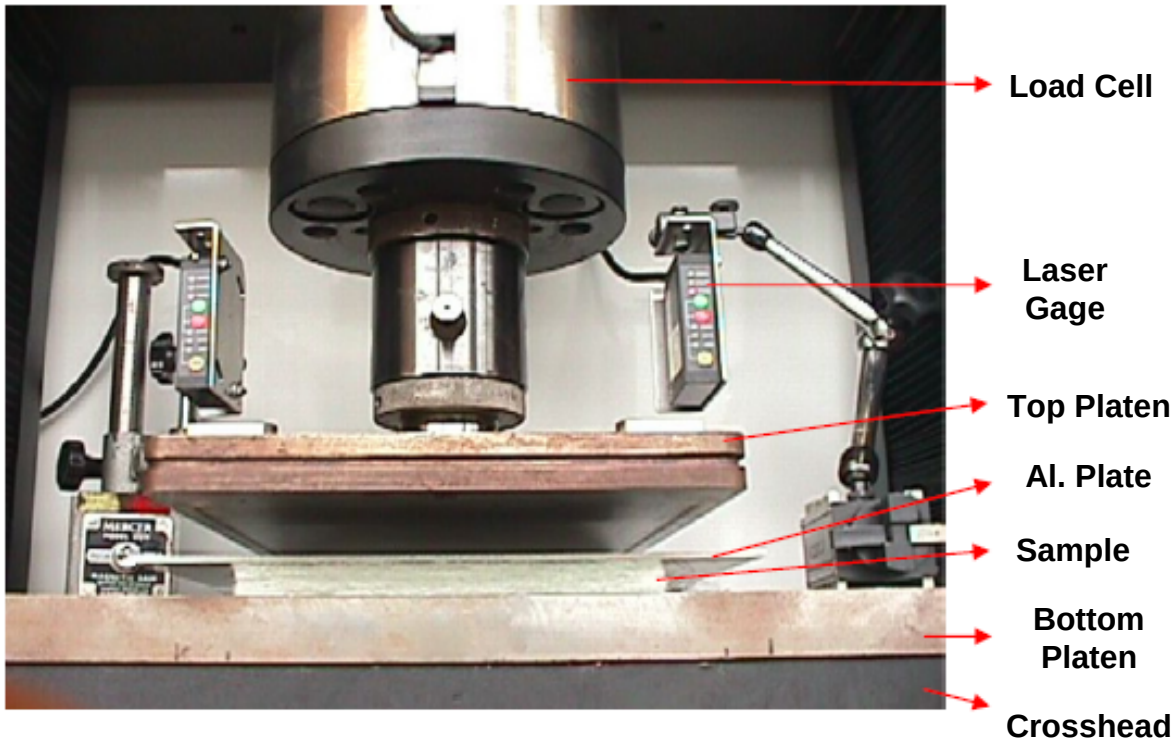

Figure 2.3 The experimental set up of Somashekar et al. [35].

Chen et al. [36] also performed compaction experiments to investigate the compaction behavior of fabric preforms in the RTM process. Two steel flat plates attached to a hydraulic press were used for the compaction experiments. Distance between plates was measured as a function of applied compressive force. Contact pressure between adjacent fabric layers during compaction was measured using a TekScan pressure measurement system. A model of the compaction behavior of woven fabric preforms was proposed by studying the internal pressure distributions between individual fabric layers. Analytical expressions relating the compaction force to fiber volume fraction were established.

Kruckenberg et al. [37] used a pair of circular platens attached to an MTS machine to perform compaction experiments on plain woven textile fabrics. Two set of experiments were done. The first set of experiments involved statically compacting the specimens, allowing relaxation at each step. The compaction speed was held constant. Dry and wet tests were done and compared. An extensometer was placed between the platens to record displacement and compared to the MTS machine recordings. They concluded that the compaction response of the fabrics followed a power law model as suggested by Robitaille and Gauvin [24]. In the second set of experiments, repeated compaction cycles were applied to the preforms in a VARTM process set-up. The tests were referred to as "vibration compaction" experiments. Two methods were used to perform these tests: first; by cycling the pressure under a vacuum bag before resin infusion and second; by applying a mechanical vibration roller on the surface of the vacuum bag after applying the vacuum but before resin infusion. The motivation for conducting these experiments was to demonstrate that vibration could cause rearrangement between individual fiber tows and preform layers; causing a reduction in the overall reinforcement thickness. The number of layers, number of cycles, effect of lubrication, effect of vibration load and frequency were varied and results were plotted to compare the different parameters. Depending on the fabric type, they concluded that vibration compaction up to 16% increase in the overall fiber volume fraction.

Andersson et al. [38] used digital speckle photography, an image processing technique to measure the thickness of the vacuum bag in Vacuum Assisted Resin Transfer Molding (VARTM) process. In this technique, speckles were created on the vacuum bag using special spray paints and the motion of the pattern formed by speckles is photographed using two special cameras. Deformation maps, revealing the change in thickness, are made after processing these

images. A sample deformation map is shown in Figure 2.4. It was concluded that with the use of this method, compaction of a larger area can be continuously monitored with better accuracy compared to other single point sensor measurement techniques.

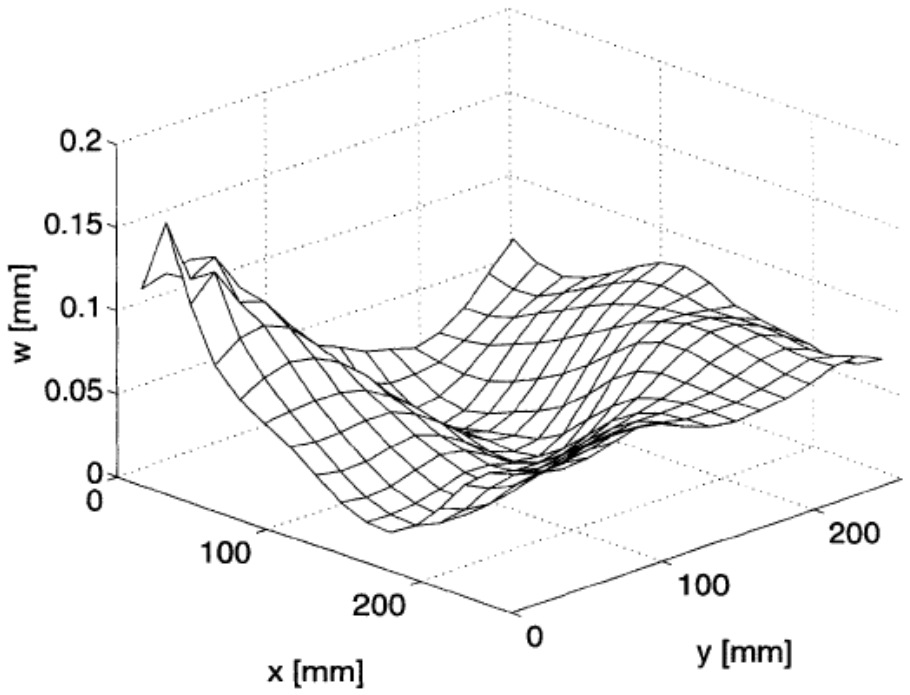

Figure 2.4 Deformation map for a vacuum infusion process with radial flow [38].

Yenilmez et al. [39] used a circular closed fixture to compact random fabric preforms with an embedded core distribution medium (sandwich preform) to be used in a VARTM type of process. Compaction tests were performed at a constant load rate and dial gages were used to measure the part thickness. Tests were performed in a way that mimics the actual VARTM process; fabric is kept dry during loading whereas kept wet during unloading and a relaxation period was also introduced. It was concluded that an accurate compaction database is needed in

the design of VARTM process parameters such as the amount of vacuum, resin gelation, preform compaction and pressure to achieve uniform part thickness in this process.

2.4 Permeability:

Throughout the literature, process models and simulations are well studied [14-23]. These are vital tools for gaining a thorough knowledge of the VARTM process thereby eliminating time consuming trial and error approaches for the manufacture of void free and high quality composite parts. One of the critical material input properties required for these process models is the preform permeability. Permeability is the measure of preform material resistance to flow and depends on the velocity of the infiltrating fluid and the pressure gradient within that preform.

Permeability measurement techniques can be classified as advancing flow front (transient) and steady-state (saturated) methods. The advancing flow front method is carried out with a dry preform and the steady-state method is carried out after the preform has been saturated with a testing fluid. The former method can account for wetting characteristics and capillary effects whereas the latter one is capable of doing material characterization by using a single preform for multiple volume fractions.

The permeability measurements can either be done by using a one dimensional (unidirectional) fixture or by using a radial fixture. In-plane and transverse permeability measurement can be performed by using these two fixture types and under either transient or steady state conditions. Wang et al [40-41] used both fixture types to determine the principal flow directions and in-

plane permeabilites of various fabric reinforcements. The advancing front radial fixture was used to locate the principal material directions which lie along the major and minor axes of the elliptical flow front.

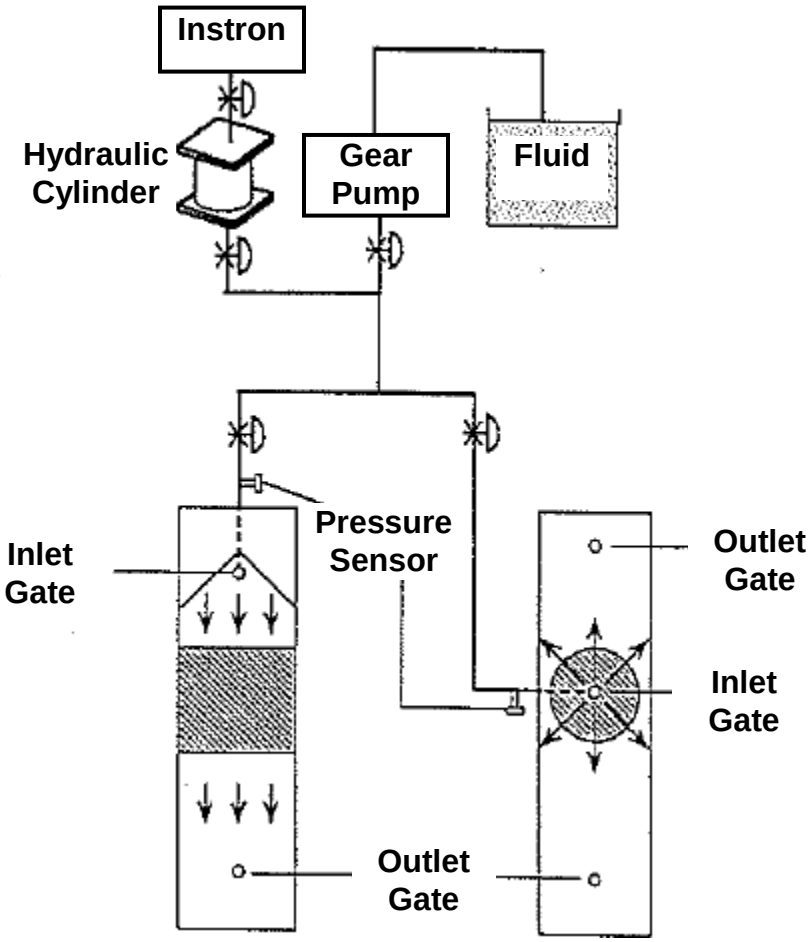

Figure 2.5 The two types of fixtures used to measure in-plane permeability and the experimental setup. Unidirectional 1D fixture shown on left, radial fixture shown on right [40].

The ratio of permeabilities along these axes is given by Equation 2.1 below:

$$\frac{\text{length of minor elliptic axis}}{\text{length of major elliptic axis}} = \left[\frac{S_y}{S_x}\right]^{\frac{1}{2}} \tag{2.1}$$

where S_x and S_y are the permeabilities along the principal axes. They found the absolute values of the permeabilities by using the principal directions, ratio of permeabilities from flow visualization and also using Darcy's Law [42]. They also employed both type of fixtures in conjunction with a cylinder arrangement to measure the transverse permeability [41]. Figure 2.5 shows the two types of fixtures (unidirectional 1D on left, radial fixture on right) used to measure the in-plane permeability used by Wang et al [40]. Figure 2.6 shows the radial fixture involving transverse fluid flow through fabric used to calculate transverse permeability [41].

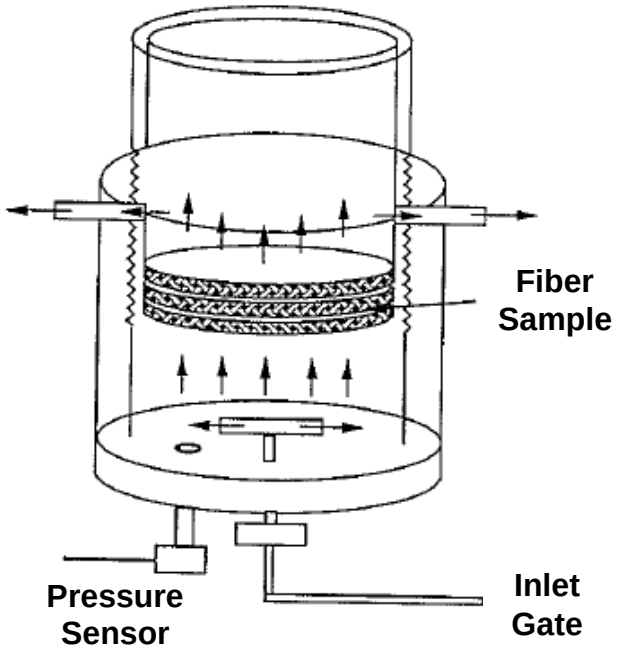

Figure 2.6 Radial fixture used to measure transverse permeability [41].

Chan et al. [43] used constant flow rate experiments to measure the in-plane permeability of anisotropic preforms. The experiments were done with a radial flow fixture. The radial flow fronts positions (in x and y directions) were recorded using a video system and the inlet pressure at the center of the radial fixture was measured. Corresponding in-plane permeabilities were calculated using Darcy's Law. The experimental results revealed a linear relationship between

flow front positions and pressure gradients meaning little deviation from Darcy's Law. They derived separate expressions for permeability for preforms with anisotropic, orthotropic and isotropic characteristics.

Parnas et al. [44] performed in-plane permeability and transverse characterization tests for random mat and 3D woven fabrics. Permeability values were reported for radial flow, saturated and unsaturated one-dimensional flow, and through-thickness flow geometries. Results obtained with the 3D woven fabrics showed much smaller scatter compared to random mat fabrics. It was concluded that the variations in the results demonstrate the importance of the structural heterogeneity in preforms and flow mechanisms such as air entrapment and wicking that Darcy's Law cannot take into account occur during the saturation of fabrics.

Gauvin et al. [45] performed flow simulations of a subway seat to be manufactured using Resin Transfer Molding (RTM). Permeability measurements for continuous strand mats were made to be used as an input to the simulations. They compared the results of 1D unidirectional flow and radial flow measurements and noted that edge effects in the unidirectional molds are sometimes inevitable and can result in erroneous permeability measurements. The technique employed by Chan et al. [43] was used for the radial flow measurements. They also mentioned about the non-homogeneity in continuous strand mats and the difficulty in getting consistent data.

Hammami [46] investigated the key factors in permeability measurements for the VARTM process. A unidirectional flow fixture was used and the validity of Darcy's Law under effects of several factors was investigated. These factors include the effect flow enhancement layers, the

effect of closing of the inlet port at some distance before outlet port (the bleeding procedure) and the effect of inserts (e.g. in marine applications to increase impact resistance). It was concluded that all these factors significantly affect the flow patterns and thus the permeability, by which using the one-dimensional Darcy's Law cannot be accurately predicted.

Ding et al. [47] suggested that the conventional permeability measurement techniques measure the average permeability only and are incapable of making in-situ measurements. A new method that employs gas flow replacing the liquid flow was suggested. A closed unidirectional mold system was used. Preform permeability was determined from the measured pressure contours of the gas flow using a simplified finite difference method. They compared results to tests done with silicon oil. They concluded that the new method is capable of detecting the non-uniformities in local permeability and allows for in-situ measuring and monitoring of fibrous preform permeability for LCM processes.

Drapier et al. [48] used a radial flow cylinder arrangement similar to the fixture in [29] to measure the transient transverse permeability. The fixture is shown in Figure 2.7. The flow front through the thickness of the preform (around 1mm only) was detected using sensitive optical fiber sensors. Permeability was estimated from velocity and pressure recordings using Darcy's Law. The significance of measuring the transient transverse (through-thickness) permeability as opposed to only measuring the saturated transverse permeability was noted, since the case of transient permeability involved is more likely to be encountered in industrial applications. It was concluded that the transient permeability values for the tested biaxial fabrics came out to be as

high as 8-10 times higher than the saturated permeability values. It was also noted that handling of the optical fiber sensors was not very easy and required extra attention.

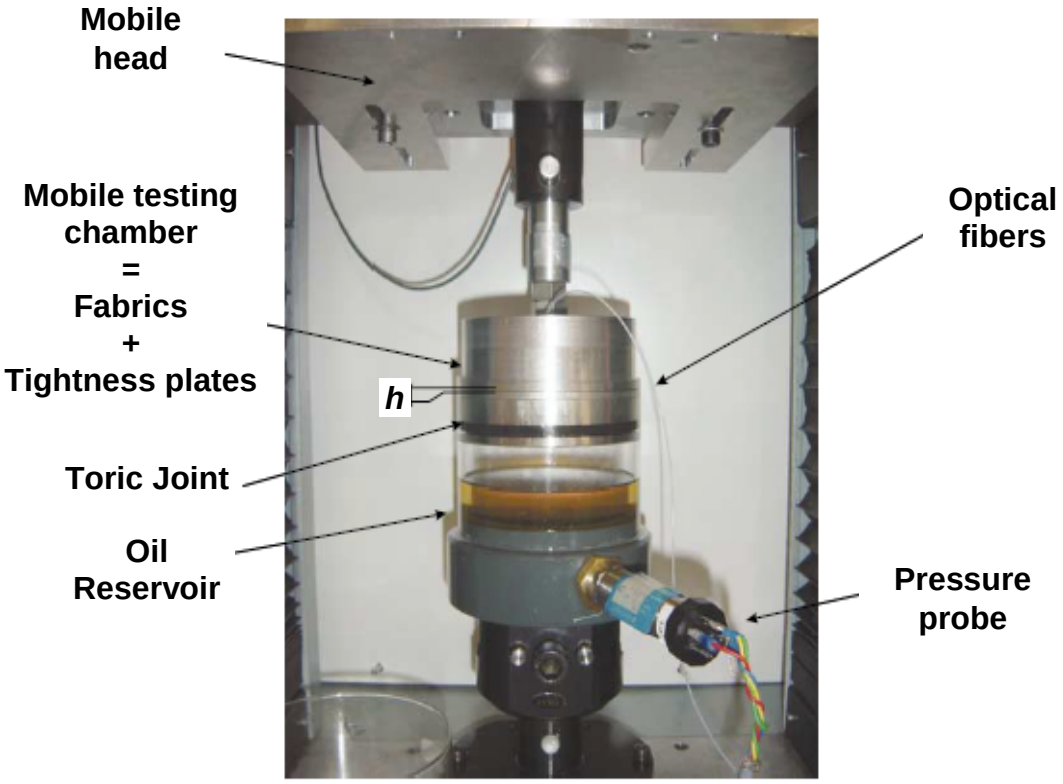

Figure 2.7 Through the thickness transient permeability measurement fixture [48].

Gokce et al. [49] suggested an algorithm that can estimate the transverse permeability of the distribution media (DM) and the preform used in VARTM processes. They noted that DM permeability needs to be measured in-situ rather than being measured separately. An iterative algorithm, that keeps iterating permeability until simulated resin flow data matches with the experimental flow data, was created. It was concluded that DM permeability depends on the preform lay-up (i.e. number of layers of preform and DM). They also added that the algorithm was useful in hybrid systems involving more than one material type (metal and fabric) where it is

difficult to develop an analytical method. A schematic for the iterative algorithm used is shown in Figure 2.8.

Talvensaari et al. [50] studied the effects of stitching pattern, stacking sequence and stitching thread tension level on permeability of woven carbon fibers. A two dimensional radial flow method was used to measure permeability. The flow front was measured by using dielectric sensors and a pressure sensor was placed at the center injection port. It was concluded that stitching increases permeability and thread tension levels have no significant effect. Among the factors considered, it was found that the stacking sequence had largest influence on permeability.

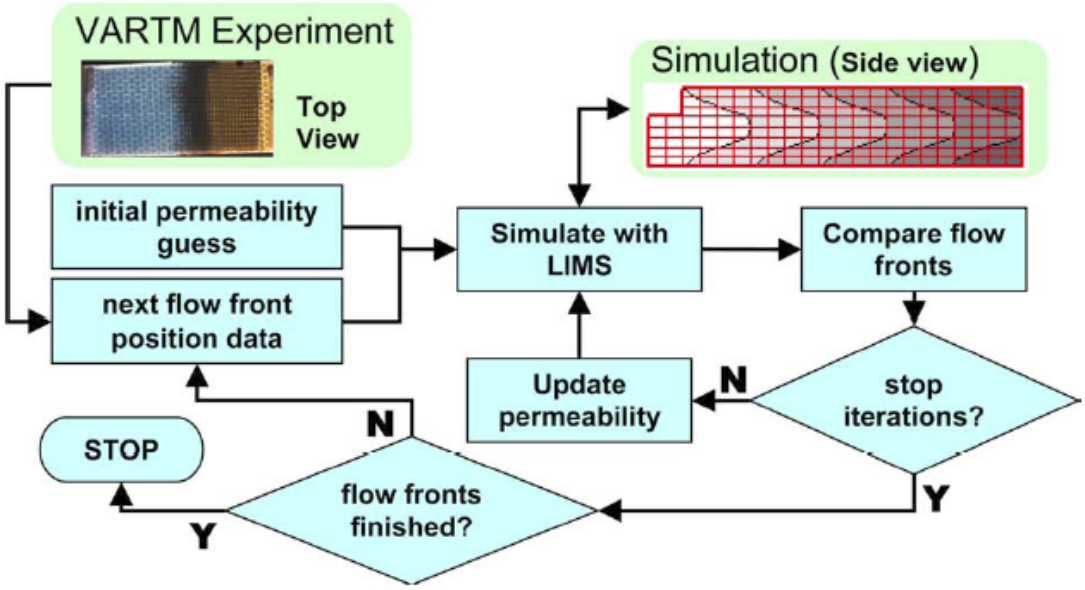

Figure 2.8 Transverse permeability estimation algorithm [49].

Nordlund et al. [51] developed a global permeability prediction model which considered the effects of perturbations of the geometry and the geometrical features from the stitching process, i.e. the presence of the thread and fibers crossing the inter-bundle channels. Biaxial non-crimp stitched fabric was used. The model was based on detailed unit cell models of the local geometry

that were used to determine the local permeability distribution within a fabric. CFD simulations were performed in order to calculate the permeability of the unit cells. These unit cells were then coupled in a network to yield the global permeability. It was shown that the presence of the thread in the inter-bundle channels has small influence on the global network permeability compared to the geometrical feature of the stitching process; the fibers crossing the inter-bundle channels. These crossings were proved to significantly reduce the global permeability. It was noted that the permeability of a fabric can be increased by a more precise stitching process, which reduces the amount of crossings.

Dong [52] proposed a fast permeability measurement technique based on a 1D unidirectional transient method for hybrid preforms with more than one type of fiber mat. Darcy's Law and the continuity equation were utilized along with a control volume finite element approach. The resulting expressions were complex and they were not very easy to adapt to different fiber lay-up configurations except the configuration that was used in this study.

Lee et al. [53] defined a parameter called 'porous space' in their method of predicting the in plane permeability of mat/roving fiber preforms used in the VARTM process. On the basis of experimental observations, it was assumed that the change of the permeability in different experiments was mainly affected by the space provided by the fiber. Accordingly, a prediction method based on the idea of "total porous space of the reinforcement" was proposed. It was noted that considering the physical characteristics, the porous space that the mat/roving fiber provides could be calculated no matter what kind of fiber preform, what layer order or number of layers were used. Changing any of these variables was assumed to be the equivalent of changing

the “porous space” provided by the preform where resin can flow through. Predictions made using the suggested method gave reasonable estimates when compared with the one dimensional in-plane permeability measurements. The study was aimed to predict the permeability values without actually performing experiments.

Endruweit et al. [54] performed permeability characterization tests for random discontinuous carbon fiber preforms. Unsaturated in-plane permeability was determined in radial flow experiments at constant injection pressure. Flow front arrival was detected by an array of pressure transducers. Based on the characterization tests, it was noted that due to the stochastic distribution of fiber bundles in the tested preforms, the preform porosity and permeability were nonuniform. It was indicated that with increasing fiber bundle length and increasing filament count, i.e. increasing local nonuniformity, increasingly uneven flow fronts developed during the injection processes. It was concluded that the preform permeability increases continuously with increasing fiber bundle length and different types of fiber sizing and different bundle cross-sectional shapes affect the overall permeability. A model based on an alternating arrangement of fiber bundles and voids for global preform permeability was also suggested.

Chapter 3

FLOW VISUALIZATION TESTS

3.1 Introduction

Flow visualization tests were performed with the layered fiber/metal hybrid preform to observe the flow patterns and determine whether the hybrid preform can be completely infiltrated. The hybrid preform consists of interspersed metal sheets and dry woven fabrics as shown in Figure 3.1.

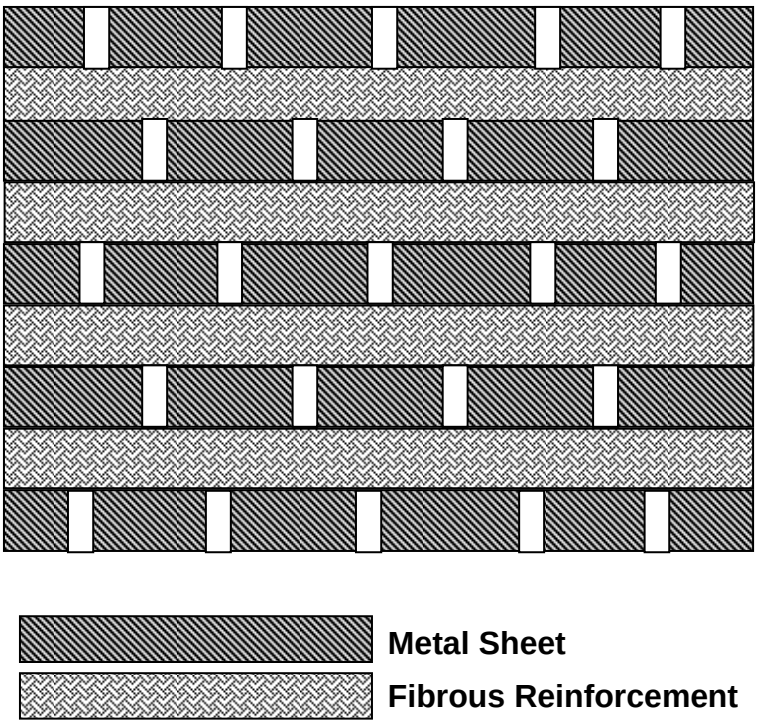

Figure 3.1 Schematic diagram of a layered fiber/metal hybrid preform.

In the manufacturing process of fiber/metal hybrid laminates, the resin is infused into the dry reinforcing fiber by a VARTM type process and bonds the metal sheets to the reinforcing fiber layers. Since resin flow in a VARTM process is primarily in the through-the-thickness or transverse direction, resin pathways were inserted into the metal sheets to allow infiltration between layers. A schematic diagram of the resin infiltration scheme from side view is shown in Figure 3.2. Obviously, the size, shape and arrangement of the pathways impact the infiltration of resin into the preform.

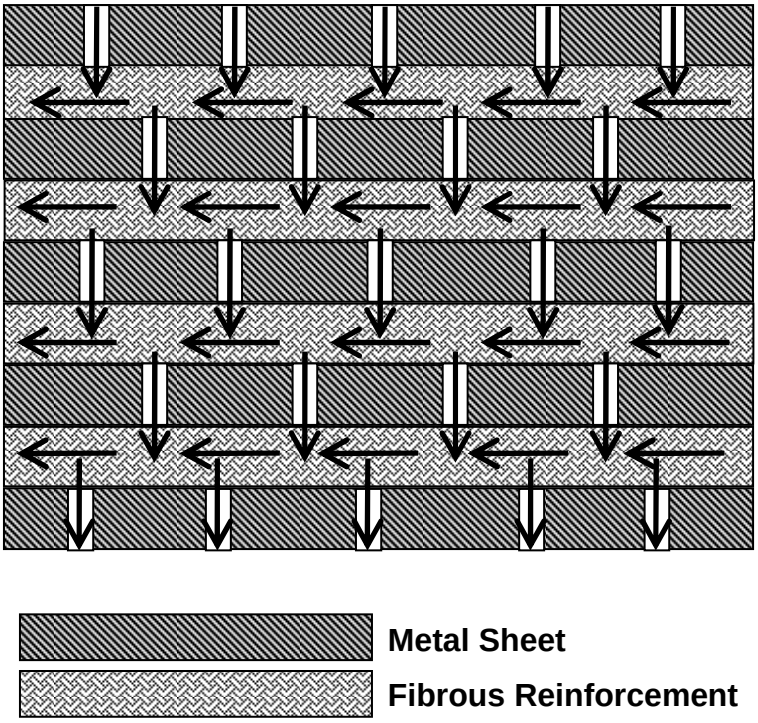

Figure 3.2 Resin infiltration into a layered fiber/metal hybrid preform shown.

3.2 Fixture Components

The visualization fixture is identical to the VARTM fixture currently used at the NASA Langley Research Center [5, 6] except for the changes noted below which were necessary to observe the fluid infiltration. A clear, scratch resistant, polycarbonate tool as shown in Figure 3.3 was used as the visualization fixture and replaced the metal tool used in the conventional VARTM processes. The dimensions of the tool are shown in Figure 3.4. Three 9.5 mm 18 NPT diameter holes were drilled and tapped into the plate for the resin inlet and vacuum connections.

Figure 3.3 Flow visualization fixture tool plate.

Clear plastic films (acetate films), 0.38 mm thick, 35.56 cm long by 35.56 cm wide, were used in place of the metal sheets for their ease of manufacturability and to enable visualization of fluid flow through individual layers. The resin pathways in the acetate films were drilled using the fixture described in Section 3.2.1.

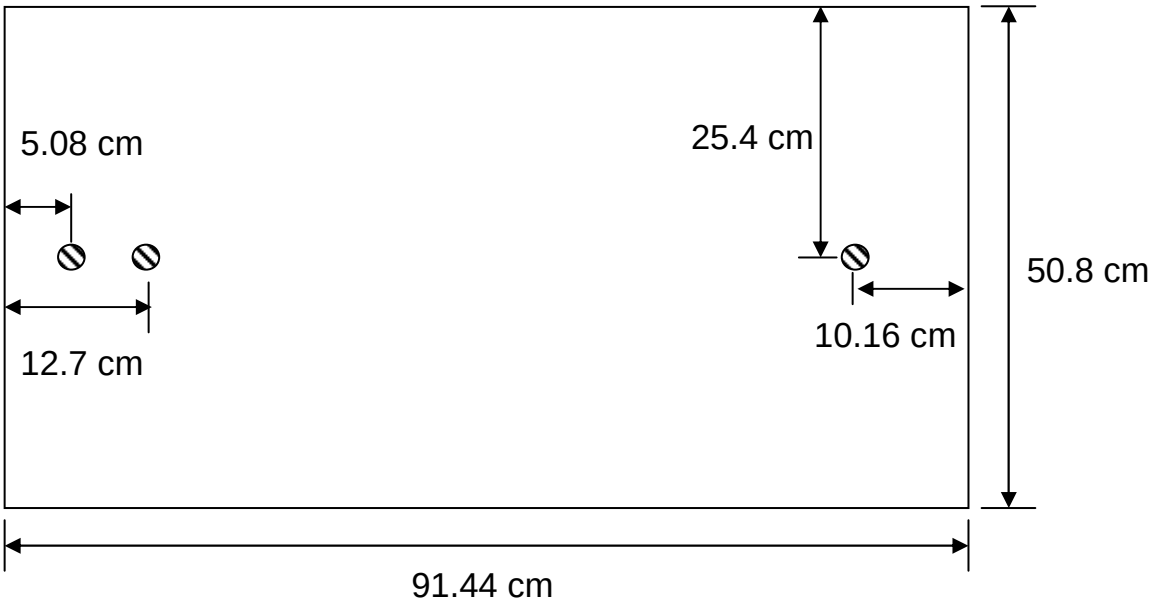

Figure 3.4 Dimensions of the polycarbonate tool.

3.2.1 Pathway Machining Fixture

A fixture was constructed to accurately machine the resin pathways into the acetate films. The fixture consists of two components and is shown in Figure 3.5. The base plate, shown on the left, was used to secure up to six acetate films and the paper template shown on the right was used to ensure proper alignment of the resin pathways. The base plate was fabricated from hard wood with dimensions of 38 cm long by 38 cm wide by 1.27 cm thick. A computer generated hole pattern was printed on paper with dimensions of 35.56 cm long by 35.56 cm wide and used as a template. The paper template was placed on top of the base plate and below the acetate layers to be drilled. Up to six sheets of acetate films and the paper template were placed against the two wooden alignment strips on the base plate and securely clamped. The pathway machining fixture was placed onto the table of a Bridgeport Variable Speed Milling Machine and clamped as shown in Figure 3.6.

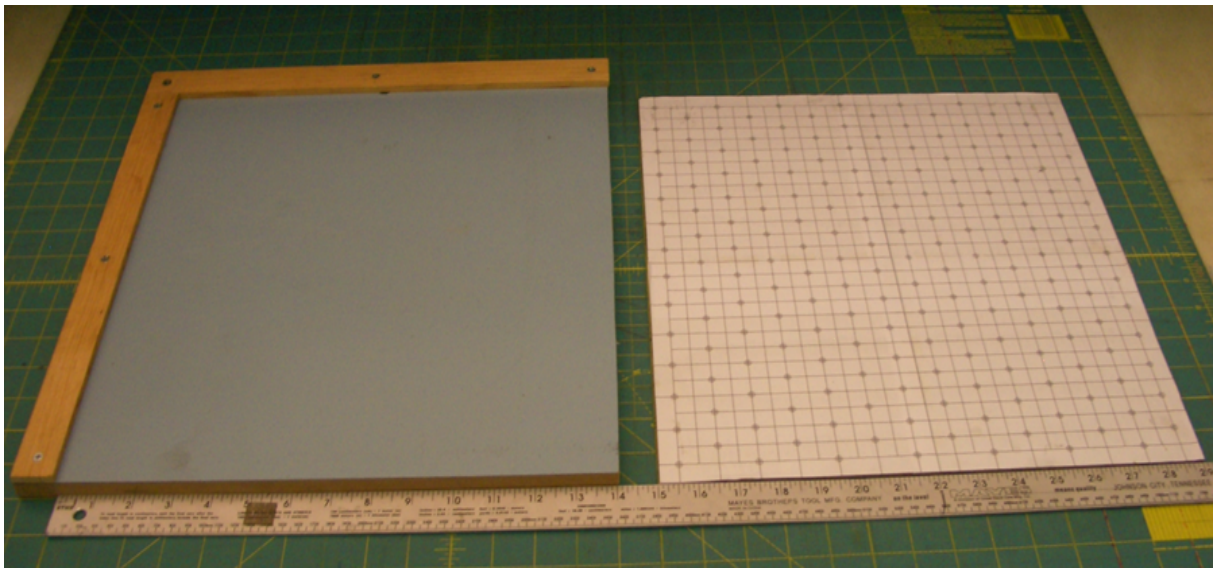

Figure 3.5 Photograph of the pathway machining fixture. The bottom plate was located on the left and the paper template on the right.

The computer generated patterns of pathways were drilled into the acetate films. Hole patterns with two different spacing configurations are shown in Figure 3.7. In the configuration shown on the left, pathways are spaced by 2.54 cm and the total number of pathways is 189. In the configuration shown on the right, pathways are spaced by 1.27 cm and the total number of pathways is 841.

Three different pathway diameters (0.41 mm, 0.83 mm and 1.59 mm) were drilled in the single density configuration whereas one pathway diameter (0.41 mm) was drilled in the 1.27 cm spacing configuration. Figure 3.8 shows the pathway diameter d and pathway spacing S. A summary of the pathway patterns is given in Table 3.1 with the diameter values d, spacing S and porosity ϕ.

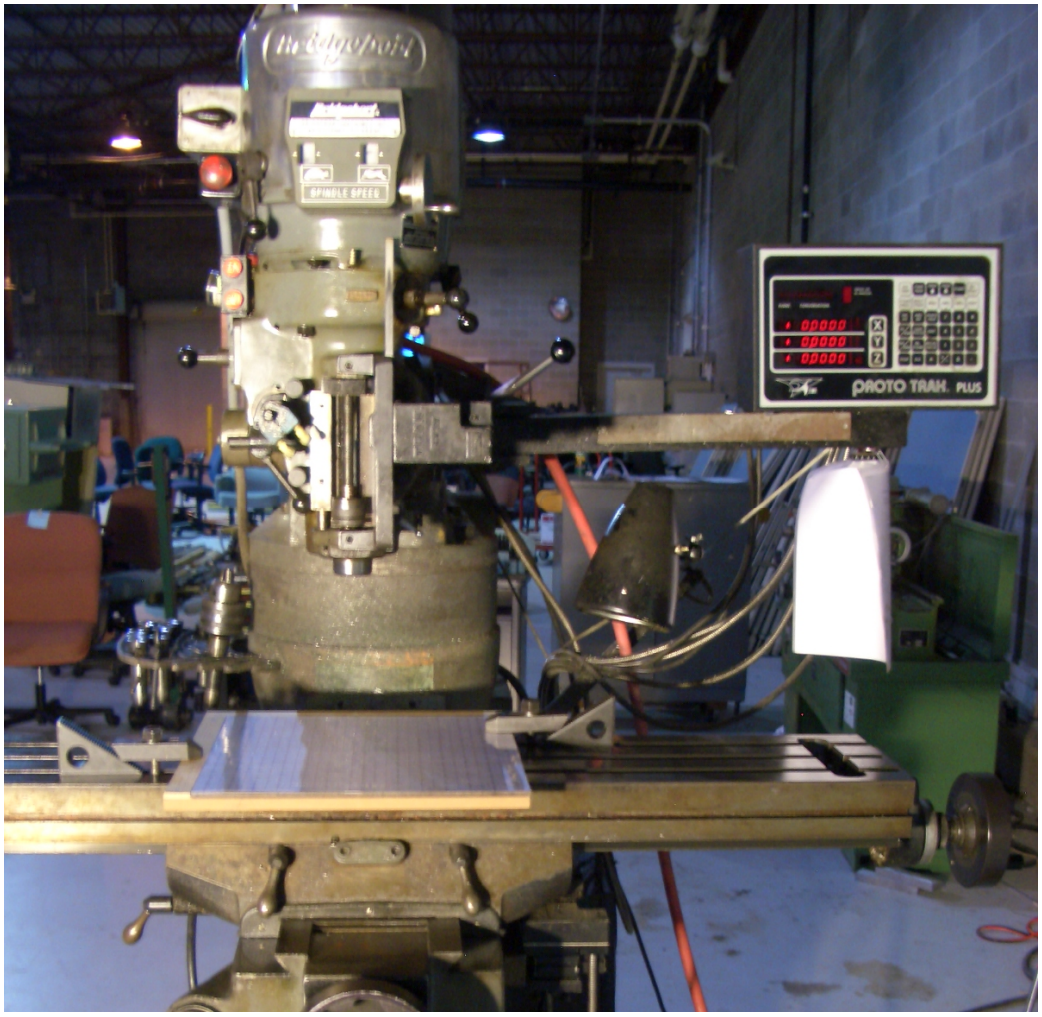

Figure 3.6 Photograph of the Bridgeport Milling Machine.

Table 3.1 Summary of Pathway Patterns; diameter d, spacing S and porosity ϕ.

	d (mm)	S (cm)	ϕ
1	0.41	2.54	0.0002
2	0.83	2.54	0.0008
3	1.59	2.54	0.003
4	0.41	1.27	0.0009

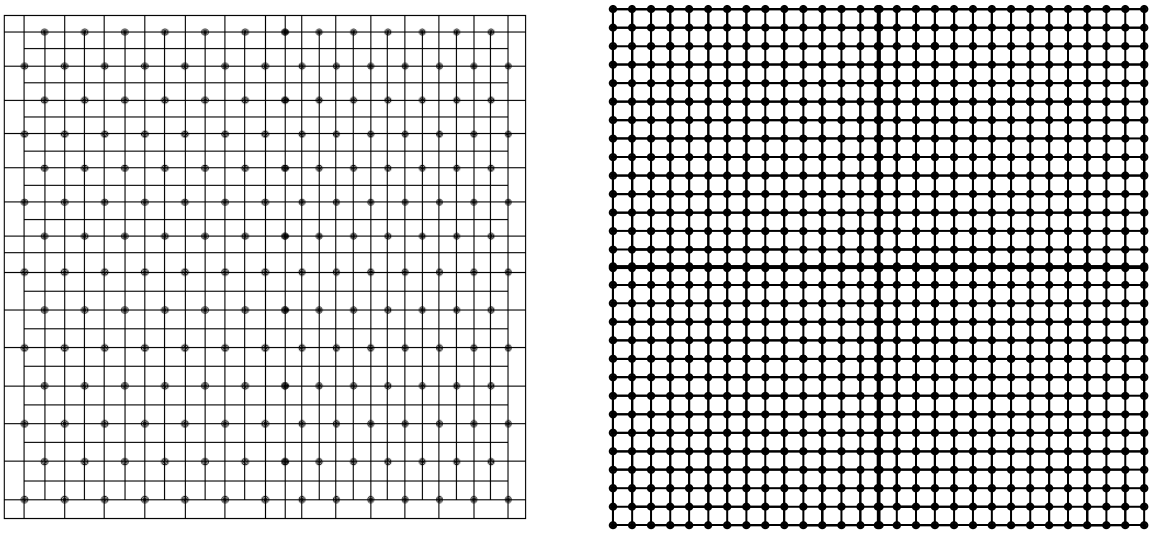

Figure 3.7 Pathway patterns with two different spacing configurations: shown on left is S=2.54 cm; shown on right S=1.27 cm.

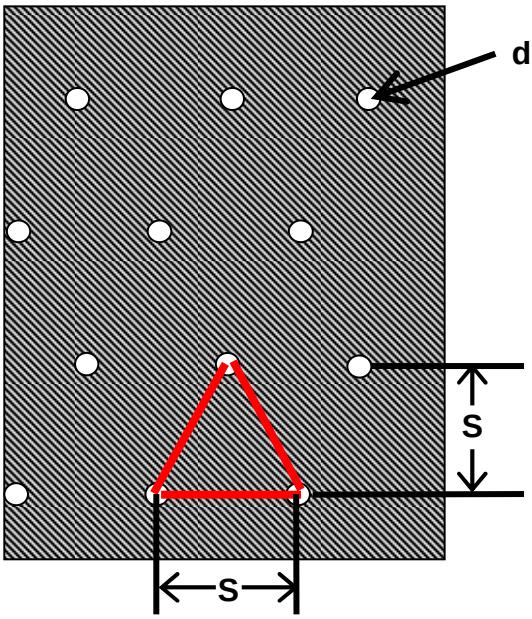

Figure 3.8 Pathway spacing and diameter.

3.2.2 Precision Drill Fixture

The resin pathways were machined into the acetate films using the precision drill fixture shown in Figure 3.9. The fixture includes a Micro Drill Adapter Precision Drill Fixture, an ALBRECHT keyless chuck and a round collet. The precision drill fixture mounts inside the collet and permits small hole drilling using large high speed machinery.

The keyless drill chuck was especially designed for holding small diameter twist drills and has a capacity to hold drills between 0 and 1.59 mm diameter. The chuck was mounted into the end of the precision drill fixture. The collet, with the precision drill fixture and chuck attached, was installed into the spindle of the milling machine as shown in Figure 3.10. The drilling fixture was used to reduce the problem of drill breakage.

3.2.3 Drilling Procedure

The present VARTM manufacturing process requires drilling a series of small diameter pathways (0.41 mm, 0.83 mm and 1.59 mm) at precise locations into the acetate films as shown in Figure 3.10. A pROTO TRAK 3-axis readout system installed on the milling machine was used to quickly and accurately locate where on the machining fixture the holes were to be drilled. The pROTO TRAK is the electronic box shown in the upper right hand corner of Figure 3.6. Once the pROTO TRAK was zeroed at a reference point on the top plate, the locations of the pathways to be drilled were easily determined. The pROTO TRAK basically eliminates the need for a template except for verification of the hole location.

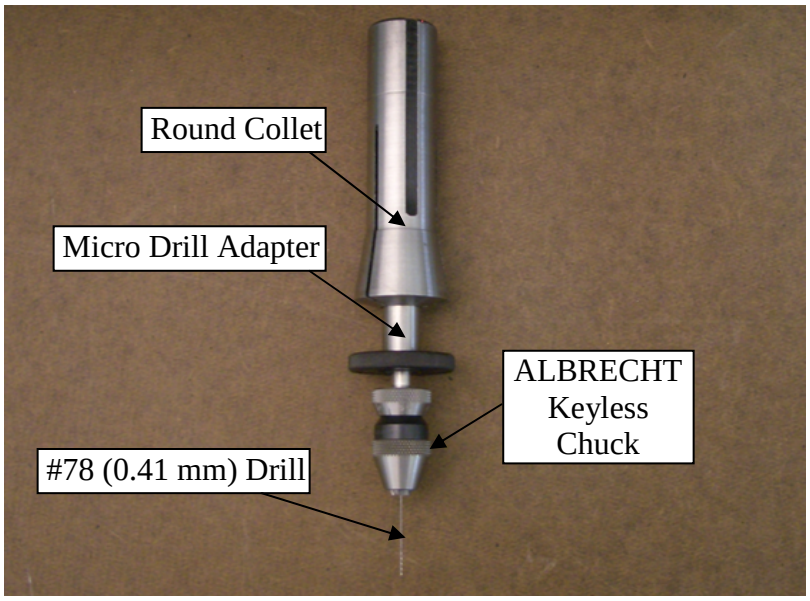

Figure 3.9 Photograph of the precision drill fixture.

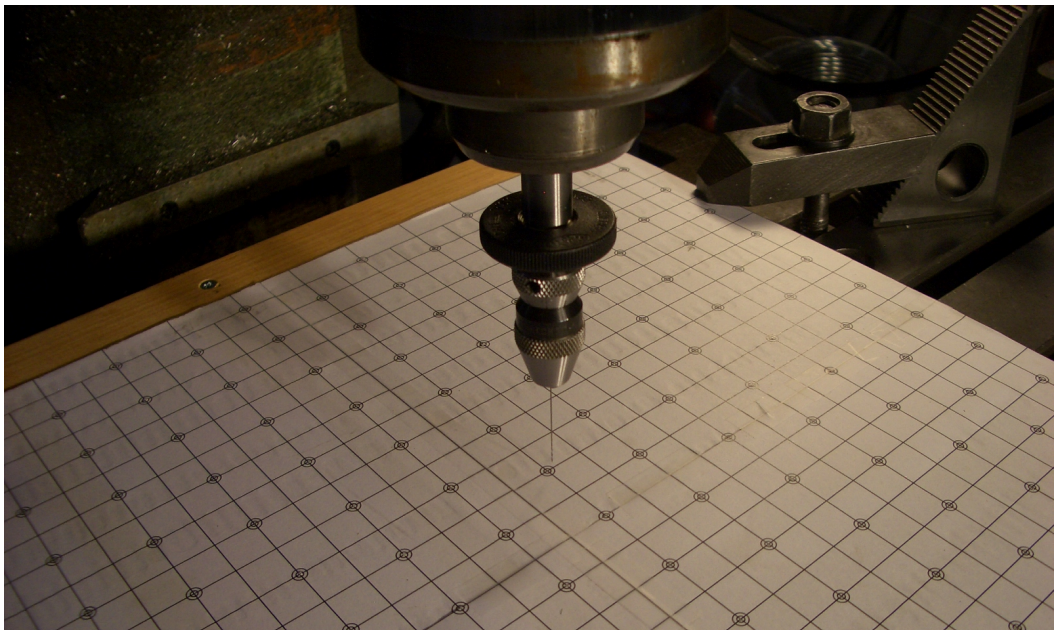

Figure 3.10 Photograph of the precision drill fixture and the template showing the location of the resin pathways to be drilled into the acetate films.

3.3 Flow Visualization Test Procedure and Materials

A diagram of the flow visualization fixture for the FML VARTM process is shown in Figure 3.11. The hybrid preform used in the flow visualization tests consisted of 5 layers of the acetate films and 4 layers of dry fabric. Shown in Figure 3.12 is a photograph of the bagged lay up on the polycarbonate tool. Mounted below the polycarbonate tool is a mirror which was used to observe the resin flow along the bottom surface of the preform. Use of the mirror allowed the video camera to simultaneously record the flow fronts on both the top and bottom surfaces of the preform. The resin inlet tube is shown on the right and the vacuum outlet tube is shown on the left.

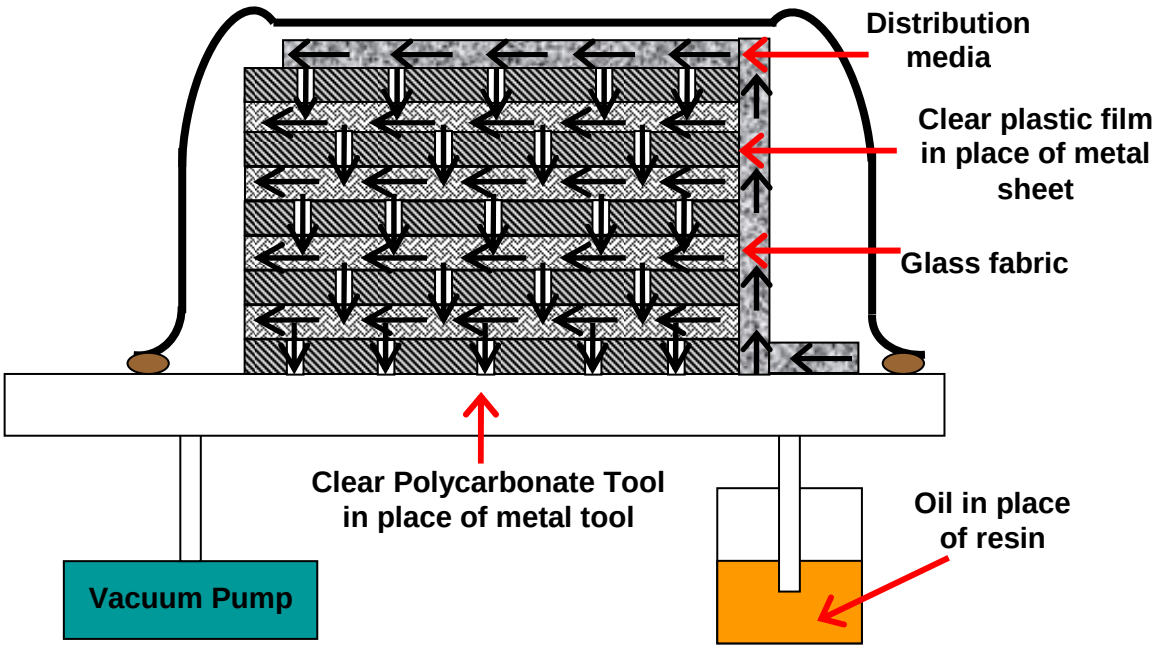

Figure 3.11 Diagram of the flow visualization fixture for the FML VARTM process.

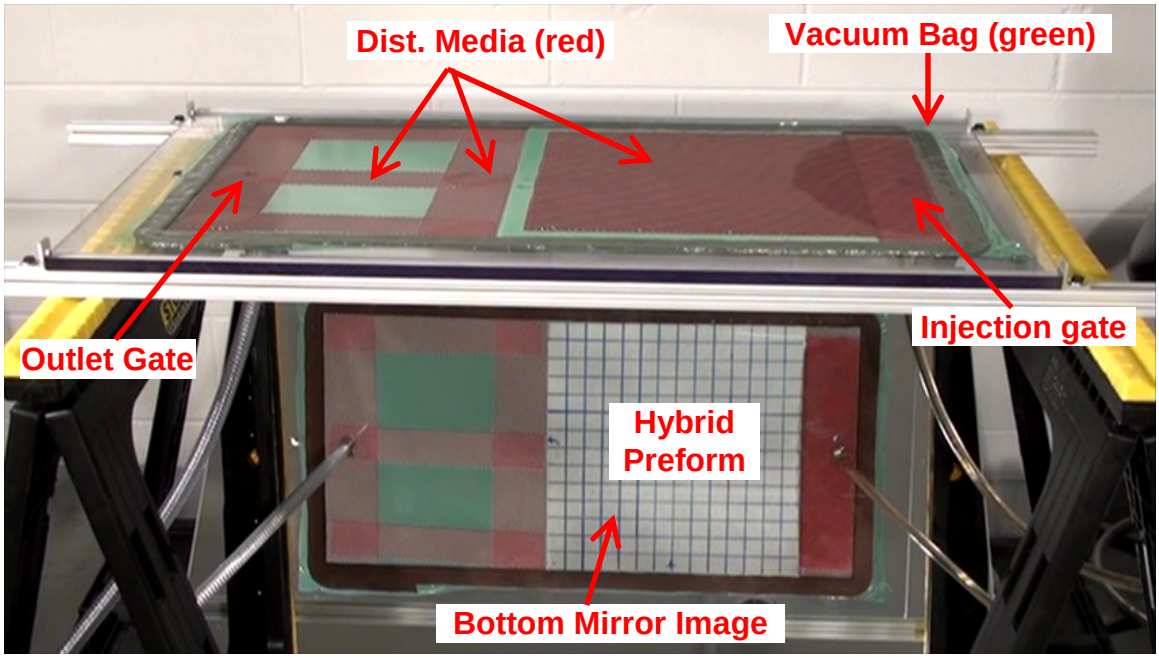

Figure 3.12 Photograph of the flow visualization fixture at the beginning of infiltration.

A total nine pieces of distribution medium were used as seen in Figure 3.12: Three layers of 40.64 cm by 33.02 cm were placed on top of the preform, three pieces cut in strips of 7.62 cm by 35.56 cm were placed on the polycarbonate tool surface perpendicular to the flow direction (one at the injection side, one at the outlet side and one at the end of the preform) and another three pieces cut in strips of 5.08 cm by 30.48 cm were placed on the polycarbonate tool surface parallel to the flow direction.

A scaled grid of 2.54 cm increments was drawn on the bottom layer of the acetate films for tracking the flow front. Acetate films were numbered by markers to observe the filling of individual layers during infiltration. The hybrid preform of fabric and acetate films was placed on top of the polycarbonate tool and then bagged and sealed with two layers of sealing tape. The sealing tape was placed 7.62 cm away from the four tool sides except the outlet side where the tape was placed 8.89 cm away from the side.

The list of materials used in the flow visualization tests is given below:

- S2 glass fabric (style 6781 8-harness satin weave from US Composites with areal weight of 293.5 g/m^2 and fiber density of 2.49 g/cc).
- Acetate films (clear plastic films) with thickness of 0.382 mm.
- SAE 40W motor oil (viscosity of 0.24 Pa.s and density of 709 kg/m^3).
- Distribution medium (Resinflow 60 LDPE/HDPE blend resin distribution medium supplied by AIRTECH Advanced Materials Group).
- Vacuum bag (Ipplon DPT1000 nylon bagging film supplied by AIRTECH Advanced Materials Group).

In Figure 3.12, a flow visualization test for the VARTM process using acetate films with pathway diameter of d =0.41 mm and spacing S =2.54 cm is shown. The fluid flow pattern in the distribution medium can be observed at the top surface 5 seconds after resin enters the fixture. Similarly, Figure 3.13 shows the fluid flow fronts on the top and bottom surfaces of the preform at 4 minutes after resin first enters the fixture. The fluid used in the visualization study was SAE 40 W motor oil. The oil was degassed for 30 minutes prior to the infiltration.

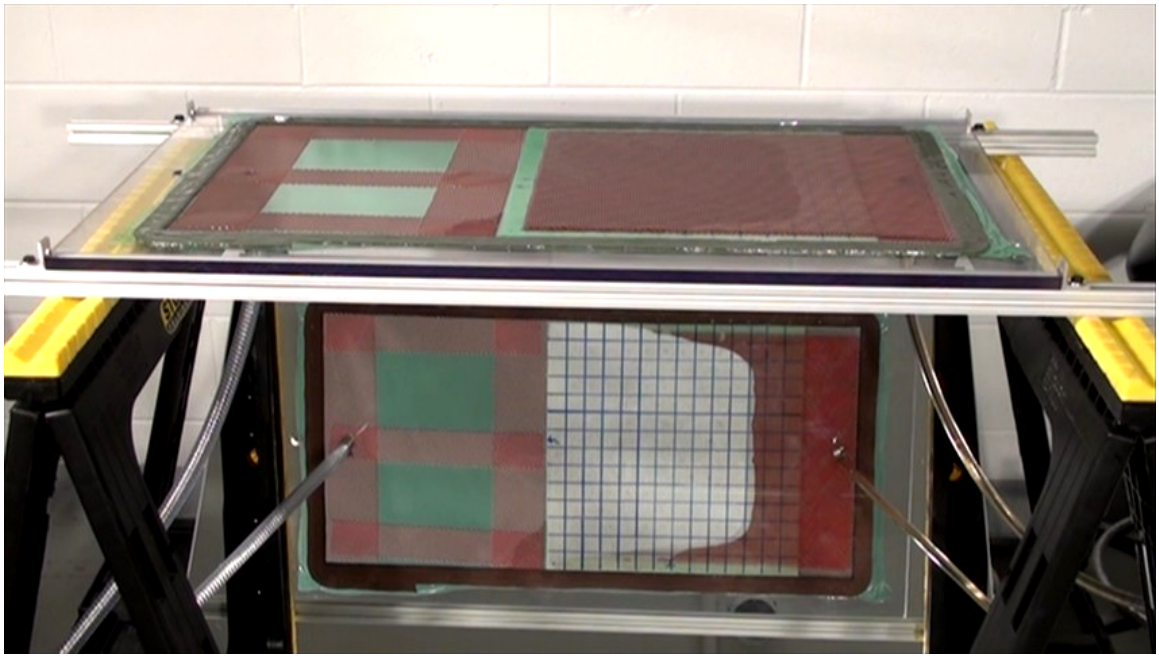

Figure 3.13 Photograph of the flow visualization fixture. Fluid flow fronts can be observed on the top and bottom surfaces of the preform.

3.4 Flow Visualization Test Results

In this section, results of the flow visualization studies will be presented. First, in Section 3.4.1, a sample flow visualization test will be discussed in detail. Then, the results will be presented for two types of processes; namely for the VARTM and for the Controlled Atmospheric Pressure Resin Infusion (CAPRI) processes in Sections 3.4.2 and 3.4.3 respectively. The CAPRI process is similar to the VARTM process except that two vacuum pumps are used in the CAPRI process; one at the inlet side and one at the outlet side to create different vacuum levels [55]. By adjusting the pressure gradient to lower values than in the VARTM process, relaxation of the preform was aimed to be minimized. Thus, a more uniform part thickness with a higher volume fraction is targeted in the CAPRI process. However, due to reduced pressure gradient, the infiltration times

in the CAPRI process are significantly longer compared to the VARTM process. In the current study, the inlet gate used in the CAPRI experiments has a reduced vacuum level of 0.5 atm.

3.4.1 Sample Flow Visualization Test

In Figure 3.14, a sample flow visualization test for the VARTM process using acetate films with flow pathways of d=0.83 mm and S =2.54 cm is shown. The flow pattern on the top surface of the distribution medium can be observed 5 seconds after resin enters the fixture. This is shown in Figure 3.14 (a). At this time, no fluid has entered the bottom surface of the hybrid preform. At 30 seconds, the distribution medium is fully infiltrated and fluid is just entering the edge of the bottom surface of the hybrid preform (Figure 3.14 (b)). The top surface of the preform is only partially saturated and still dry in the areas not covered by the distribution medium as seen in the upper left corner of Figure 3.14(b).

In Figure 3.15 (a), at t =1.5 minutes, the bottom surface reveals that the fluid has infiltrated about 2.54 cm into the preform. It is also seen that race-tracking occurs along the edges of the preform. At this time, dark circles of fluid are just beginning to appear on the bottom surface, indicating that the fluid has begun to infiltrate the final layers of glass fabric and acetate film. The top surface of the preform is still partially saturated as seen in the upper left corner of Figure 3.15(a).

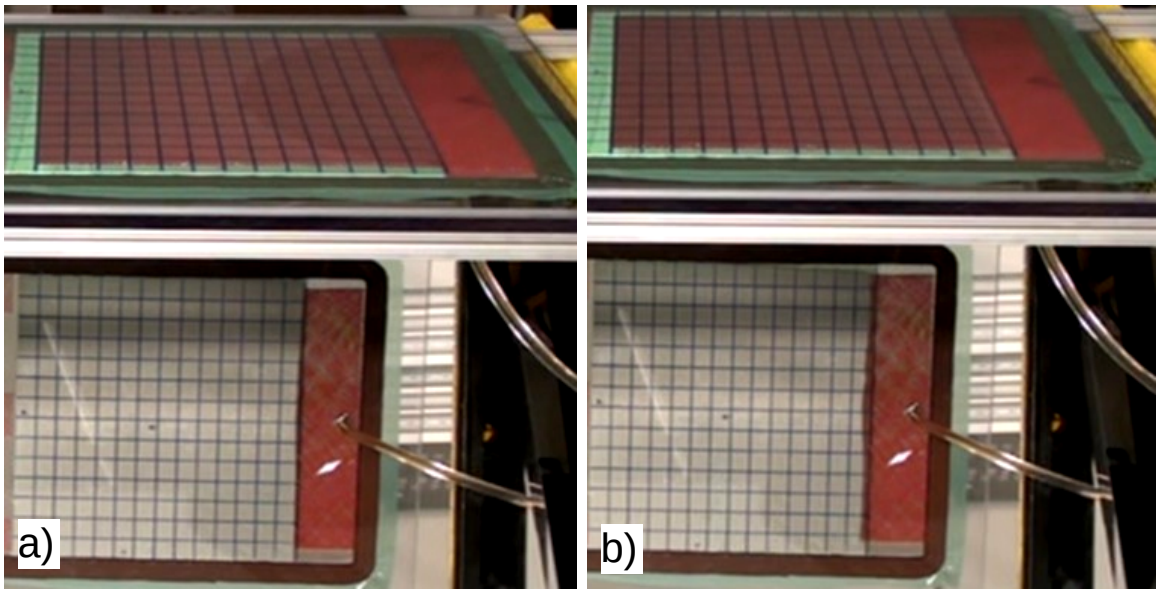

Figure 3.14 Comparison between top and bottom flow fronts at a) t =5 sec. and b) t =30 sec.

In Figure 3.15 (b), at t =3 minutes, the dark circles of fluid at the bottom surface of the preform become larger and much more visible. Infiltration has now become both in-plane from the inlet edge of the preform and transverse due to the flow pathways drilled in the acetate films. At this time, about 5.08 cm of the bottom surface of the preform have been completely infiltrated and the top surface of the preform has completely saturated. Race-tracking effects also seem to become more visible at this time.

Looking at the bottom surface in Figure 3.16(a), at t = 4.5 minutes, it is seen that transverse flow through the flow pathways is significant. The fluid flows radially outward and begins to merge with the fluid from adjacent flow pathways and the bulk flow front. In Figure 3.16(b), at t =8.5 min., the preform is completely infused and the infiltration process is complete.

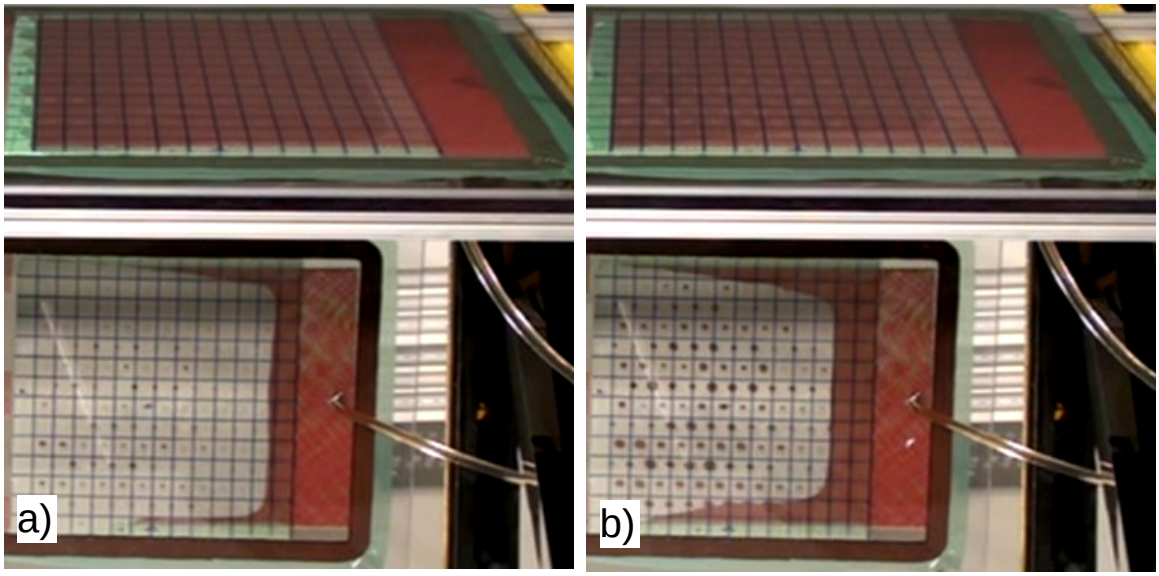

Figure 3.15 Comparison between top and bottom flow fronts at a) t =1.5 min. and b) t =3 min.

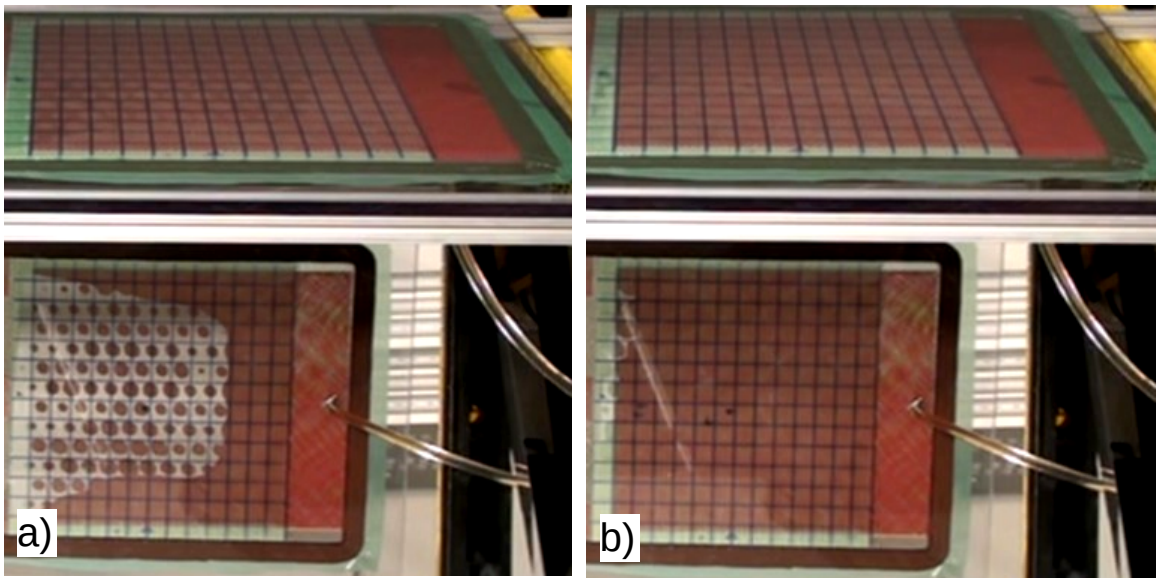

Figure 3.16 Comparison between top and bottom flow fronts at a) t = 4.5 min. and b) t=8.5 min.

3.4.2 The VARTM Process

In Figures 3.17 and 3.18, the flow patterns at the top and bottom surfaces of the hybrid preform are compared for the pathway spacing of S=2.54 cm. Figure 3.17 shows that the flow patterns on the top surface of the distribution medium are very similar for all pathway diameters. The total infiltration times are about 30 seconds for d= 0.83 mm and d= 1.59 mm and about 30 seconds for d=0.41 mm.

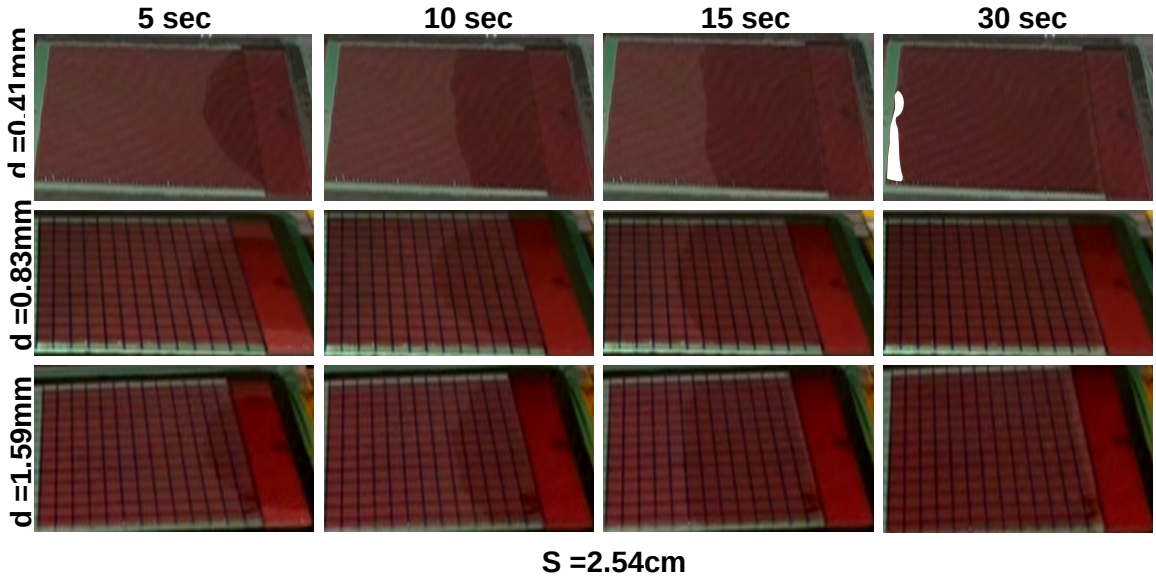

Figure 3.17 Flow patterns on the top surface of the distribution medium. For hybrid preforms with flow pathway hole diameters of 0.41 mm (top), 0.83 mm (center), and 1.59 mm (bottom).

Shown in Figure 3.18 are the flow patterns on the bottom surface of hybrid preforms with pathway spacing of S=2.54 cm. For the hybrid preform with the 0.41 mm diameter flow pathways, fluid infiltration is dominated by in-plane flow from the edges of the preform (Figure 3.18, top). Transverse fluid flow through the pathways did not appear on the bottom surface of the preform until 14 minutes. The experiment was terminated after 23.5 minutes before the bottom surface was completely infiltrated due to fluid reaching the vacuum port of the tool plate.

When the flow pathway hole diameter was increased to 0.83 mm (Figure 3.18, center), after 4 minutes into the process, fluid reaches the bottom surface of the preform by both in-plane flow thorough the edges of the preform and transverse flow through the flow pathways. After 6 minutes, flow becomes predominantly transverse through the flow pathways with complete infiltration occurring at 8.5 minutes. Increasing flow pathway hole diameter to 1.59 mm (Figure 3.18, bottom) results in transverse flow through the pathways completely dominating infiltration of the bottom surface of the preform. Complete infiltration occurs in only 4 to 5 minutes.

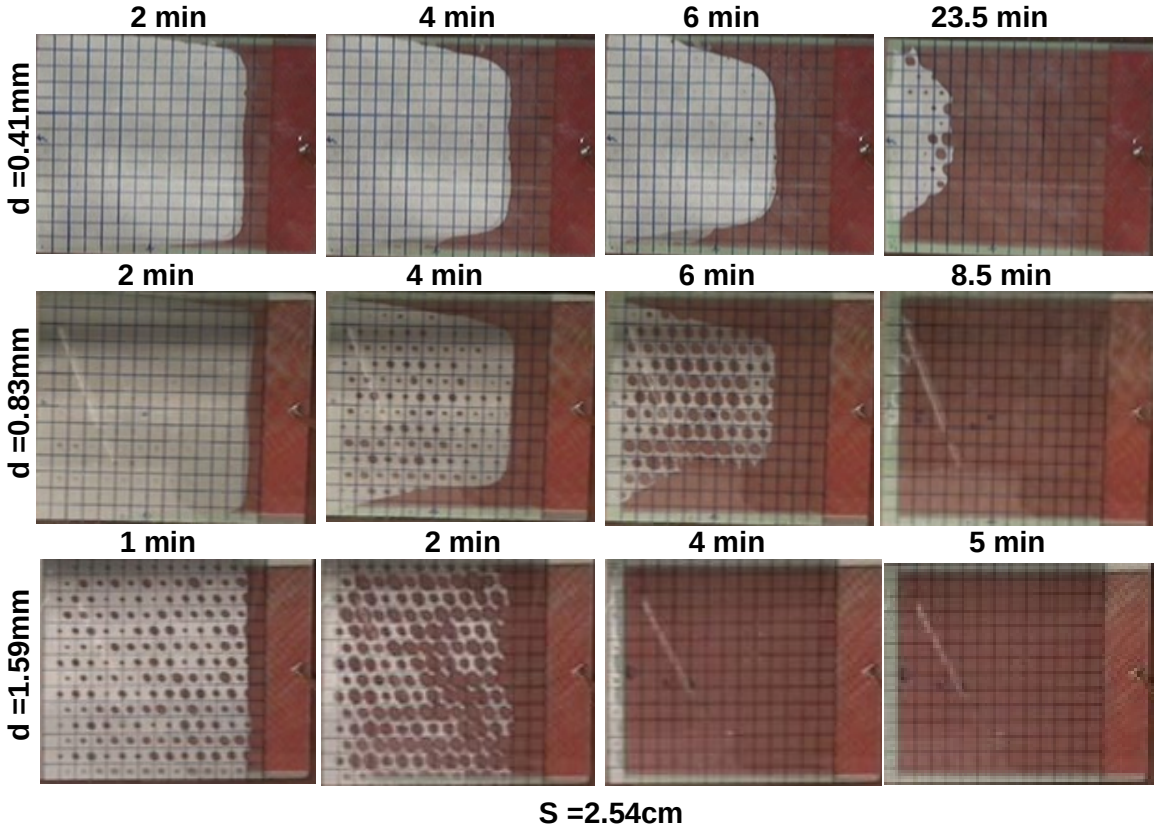

Figure 3.18 Flow patterns on the bottom surface of hybrid preforms with pathway spacing of 2.54 cm. Flow pathway hole diameters were 0.41mm (top), 0.83 mm (center), and 1.59 mm (bottom).

The flow patterns on the top surface of the distribution medium and on the bottom surface of the hybrid preform for preforms with 0.41mm pathway diameters and spacings of 2.54 cm and 1.27 cm are shown in Figure 3.19 and 3.20, respectively. It is seen that the flow patterns and total infiltration times for the distribution medium are similar. Hence, the total infiltration times for the distribution medium are independent of the pathway diameter and spacing. The flow patterns on the bottom surface are shown in Figure 3.20 and reveal that the hybrid preform with the 1.27 cm pathway spacing is completely infiltrated and the infiltration time is 40% shorter than the preform with the 2.54 cm pathway spacing. This is expected, since there are about four times more pathways for the preform with the 1.27 cm pathway spacing.

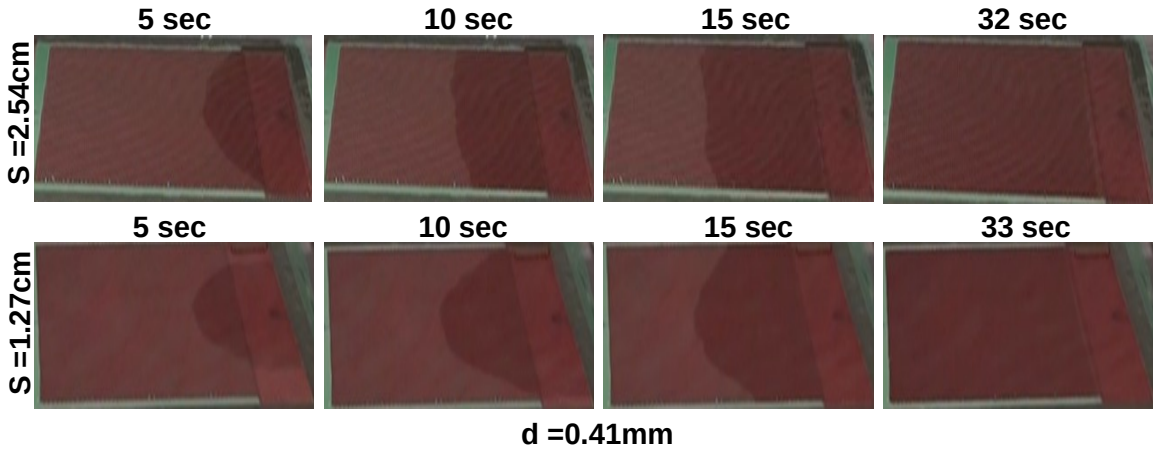

Figure 3.19 Flow patterns on the top surface of the distribution medium. For hybrid preforms with pathway spacings of 2.54 cm (top) and 1.27 cm (bottom) with flow pathway hole diameter of 0.41 mm.

Figure 3.20 also reveals that the flow patterns are different when the pathway spacing is decreased. For the 2.54 cm pathway spacing, fluid infiltration at the bottom surface is primarily in-plane. When the pathway spacing is decreased to 1.27 cm, there is significantly more transverse flow, especially in the center of the preform.

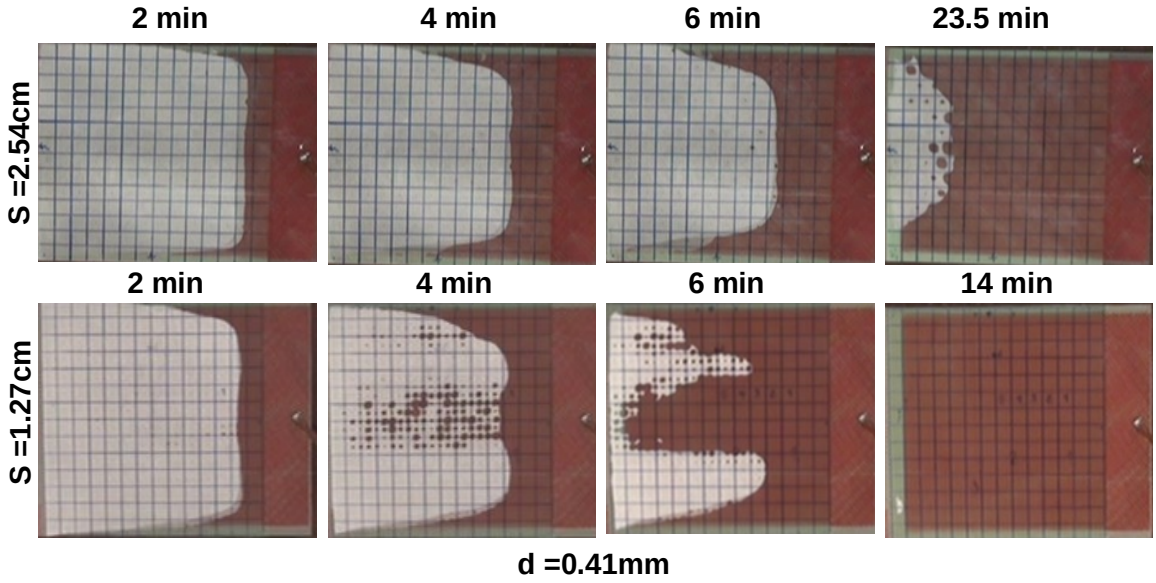

Figure 3.20 Flow patterns on the bottom surface of hybrid preforms with flow pathway hole diameter of 0.41mm. Pathway spacings were 2.54 cm (top) and 1.27 cm (bottom).

3.4.3 The CAPRI Process

In figures 3.21 and 3.22, the flow patterns on the top surface of the distribution medium and on the bottom surface of the hybrid preform are shown for preforms with 0.41 mm and 0.83 mm pathway diameters with a spacing of 2.54 cm, and a 0.41 mm pathway diameter with a spacing of 1.27 cm manufactured by the CAPRI process. The flow patterns for the distribution medium are similar for all pathway configurations. At 140 seconds, the distribution medium is completely infiltrated except for the preform with the pathway diameter of 0.83 mm. The total infiltration time for the distribution medium for this case is about 160 seconds. The difference in total infiltration times can be attributed to individual test conditions such as slight differences in vacuum levels, or the alignment of the flow pathways in the acetate films.

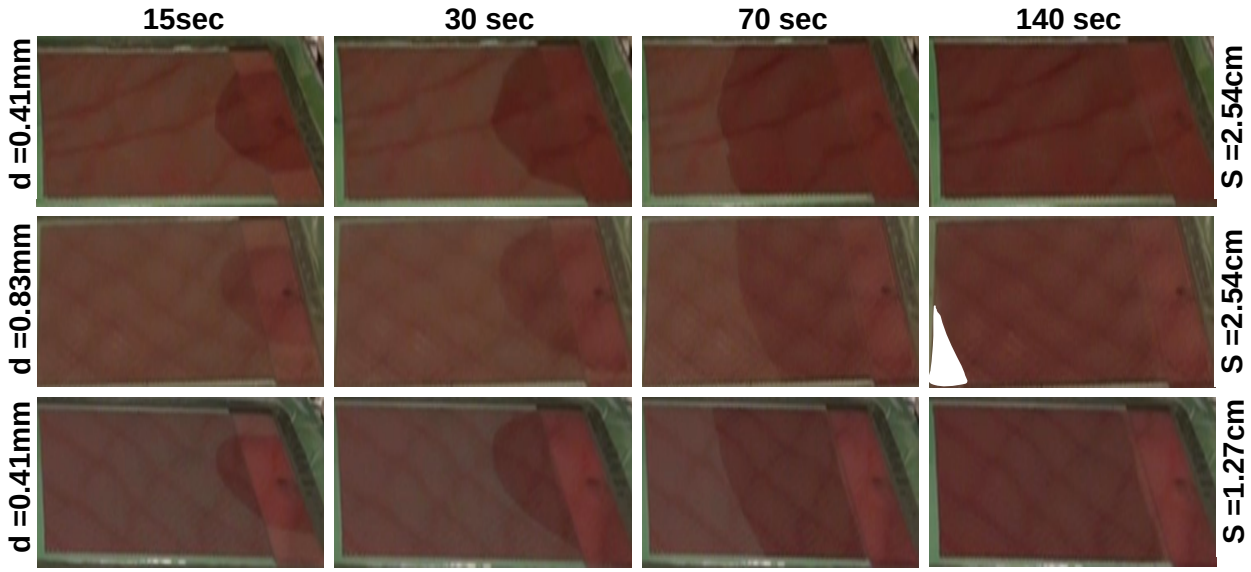

Figure 3.21 Flow patterns on the top surface of the distribution medium. For hybrid preforms with flow pathway hole diameters of 0.41 mm (top), 0.83 mm (center) with pathway spacing of 2.54 cm, and with flow pathway hole diameter of 0.41mm with pathway spacing of 1.27 cm (bottom).

Shown in Figure 3.22 are the flow patterns on the bottom surface of the preform. The total infiltration time for the hybrid preform with pathway hole diameter of 0.41 mm and spacing of 1.27 cm is the shortest at about 34 minutes. This is followed by the hybrid preform with pathway hole diameter of 0.83 mm and spacing of 2.54 cm which has a total infiltration time of 47 minutes. For the hybrid preform with pathway hole diameter of 0.41 mm and This is followed by the hybrid preform with pathway hole diameter of 0.83 mm and spacing of 2.54, the process was terminated at 43 minutes before the infiltration was complete due to testing fluid (oil) reaching the vacuum port. Similar to the VARTM process, as the pathway hole diameter increases or as the pathway spacing decreases, the transverse flow tends to dominate over the in-plane flow.

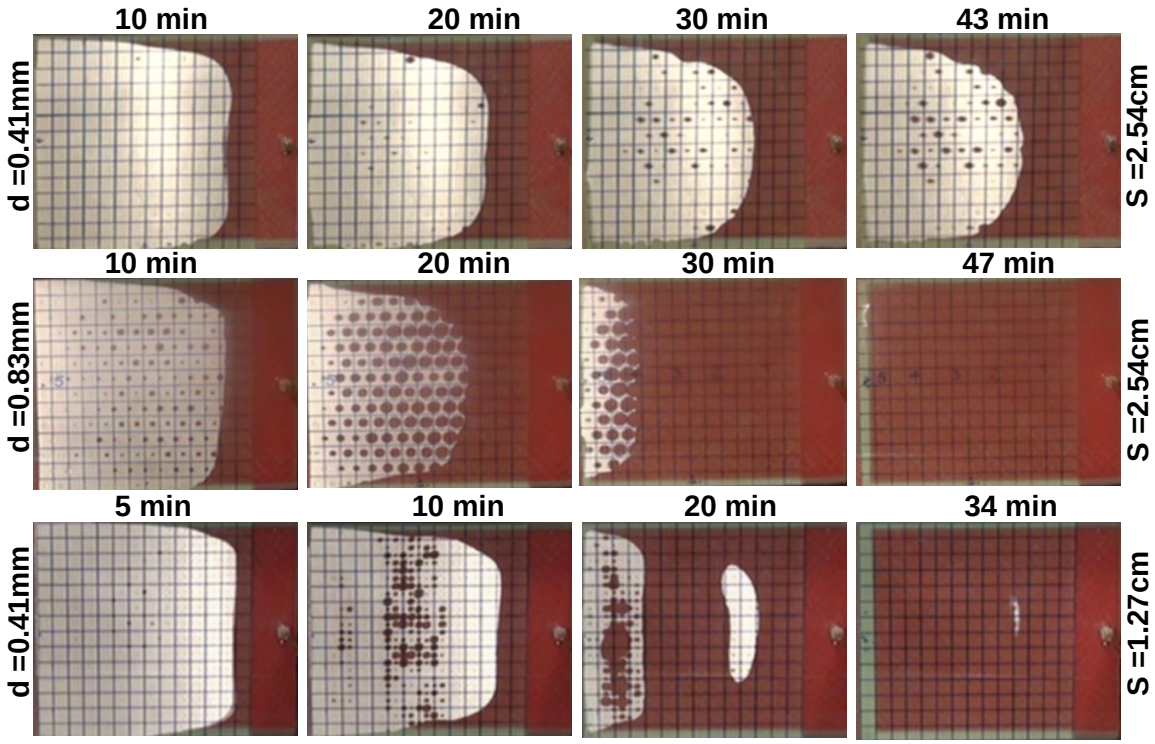

Figure 3.22 Flow patterns on the bottom surface of hybrid preforms with pathway spacing of 2.54 cm. Flow pathway hole diameters were 0.41mm (top), 0.83 mm (center), and 1.59 mm (bottom).

3.4.4 Comparison between the VARTM and CAPRI Flow Visualization Tests

Shown in Figures 3.23-3.25 are comparisons of the flow patterns in the distribution medium for hybrid preforms resin infused by the VARTM and CAPRI processes. Due to the reduced resin injection pressure, the CAPRI process takes about 4 to 5 times longer to completely infiltrate the distribution medium.

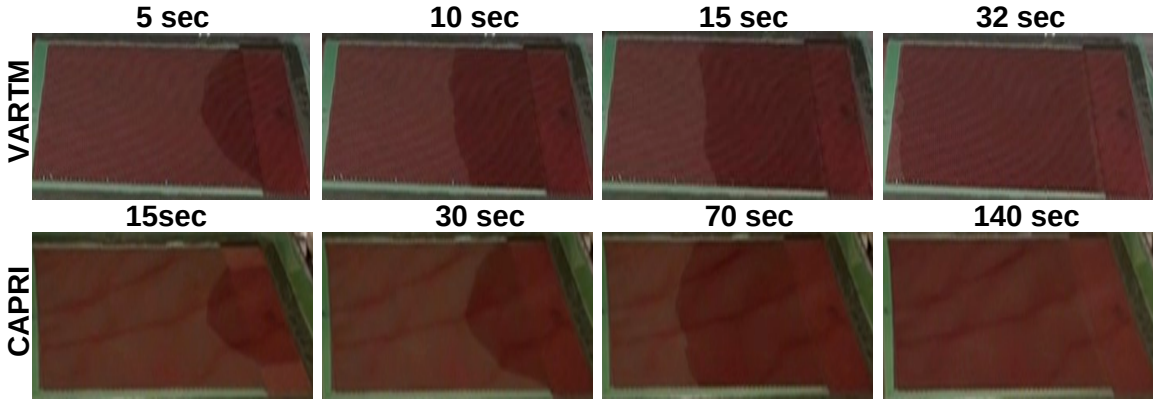

Figure 3.23 Comparison of flow patterns on the top surface of the distribution medium in the VARTM (top) and CAPRI (bottom) processes for flow pathway hole diameter of 0.41mm with pathway spacing of 2.54 cm.

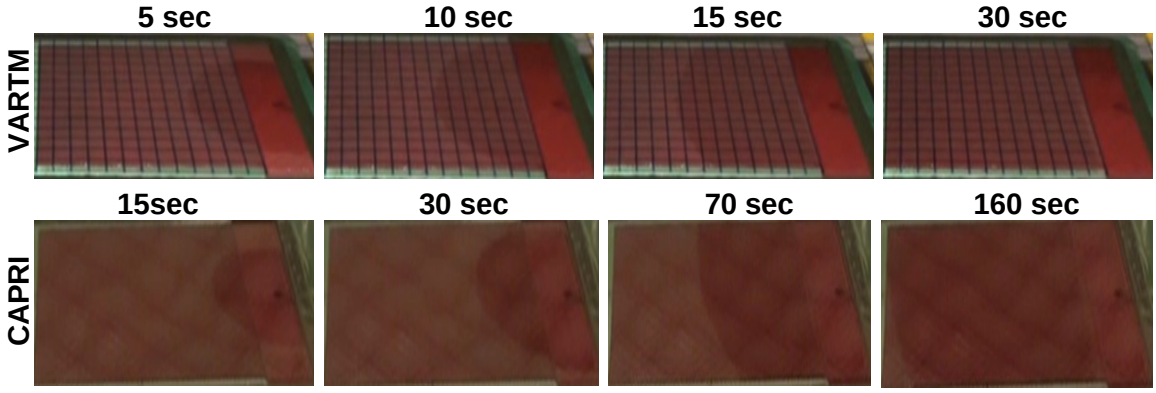

Figure 3.24 Comparison of flow patterns on the top surface of the distribution medium in the VARTM (top) and CAPRI (bottom) processes for flow pathway hole diameter of 0.83 mm with pathway spacing of 2.54 cm.

Figures 3.26-3.28 show the flow patterns on the bottom surface of the hybrid preforms measured during the VARTM and CAPRI flow visualization tests. Shown in Figure 3.26 are the bottom surfaces of hybrid preforms with flow pathway hole diameter of 0.41 mm and pathway spacing of 2.54 cm when the fluid has infiltrated about 2.54 cm, 5.08 cm, 7.62 cm and 10.16 cm into the center of the preform.

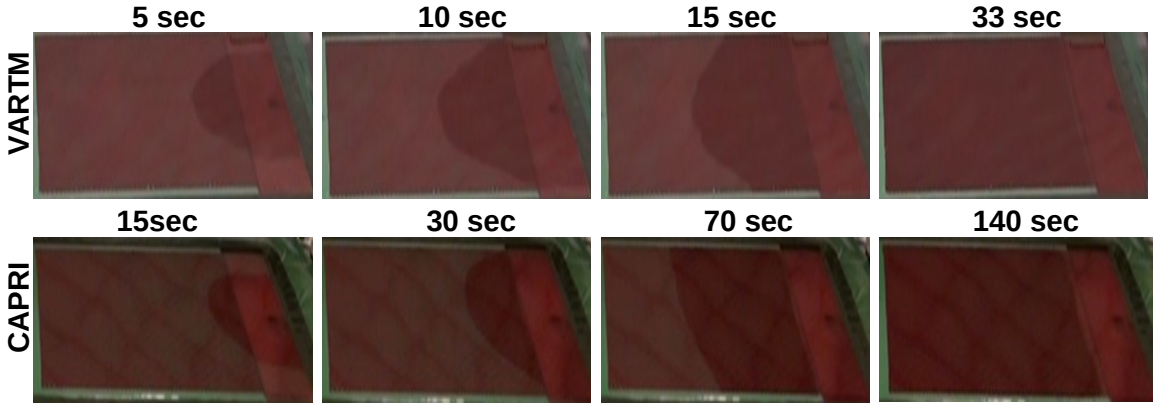

Figure 3.25 Comparison of flow patterns on the top surface of the distribution medium in the VARTM (top) and CAPRI (bottom) processes for flow pathway hole diameter of 0.41mm with pathway spacing of 1.27 cm.

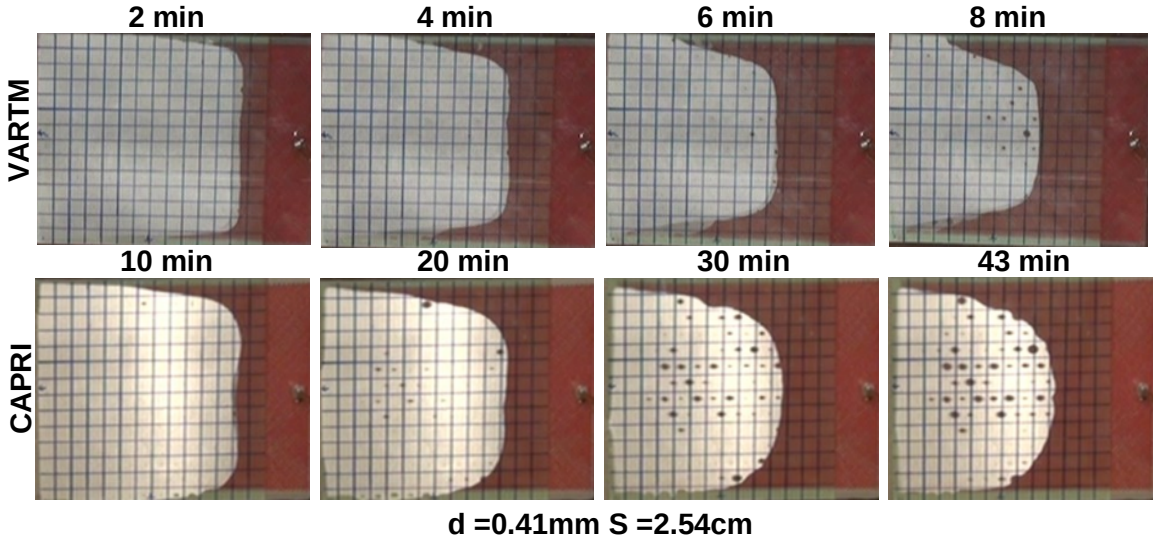

Figure 3.26 Comparison of flow patterns on the bottom surface of hybrid preforms in the VARTM (top) and CAPRI (bottom) processes for flow pathway hole diameter of 0.41mm with pathway spacing of 2.54 cm.

The filling times of the CAPRI process at these locations are about 5 times that of the VARTM process. In Figure 3.27, the bottom surfaces of hybrid preforms with flow pathway hole diameter of 0.83 mm and pathway spacing of 2.54 cm are shown when the fluid has infiltrated about 2.54 cm, 5.08 cm and 7.62 cm into the center of the preform and completely into the preform (last frame). The filling times of the CAPRI process are about 3 times that of the VARTM process in

the first three time frames. The hybrid preform is completely infiltrated in about 8.5 minutes for the VARTM process which is about one fifth of the CAPRI process infiltration time of 47 minutes.

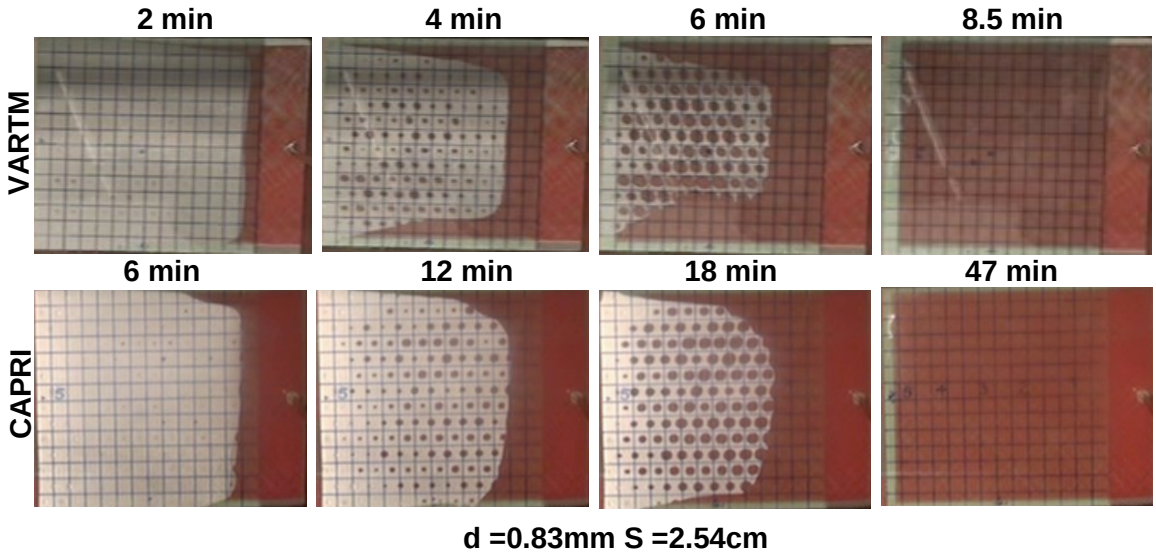

Figure 3.27 Comparison of flow patterns on the bottom surface of hybrid preforms in the VARTM (top) and CAPRI (bottom) processes for flow pathway hole diameter of 0.83mm with pathway spacing of 2.54 cm.

The flow patterns on the bottom surface of hybrid preform with flow pathway hole diameter of 0.41 mm and pathway spacing of 1.27 cm for the VARTM and CAPRI processes are shown in Figure 3.28. In the VARTM process, at 4 minutes, fluid appears on the bottom surface concentrated around the center of the preform parallel to the flow direction.

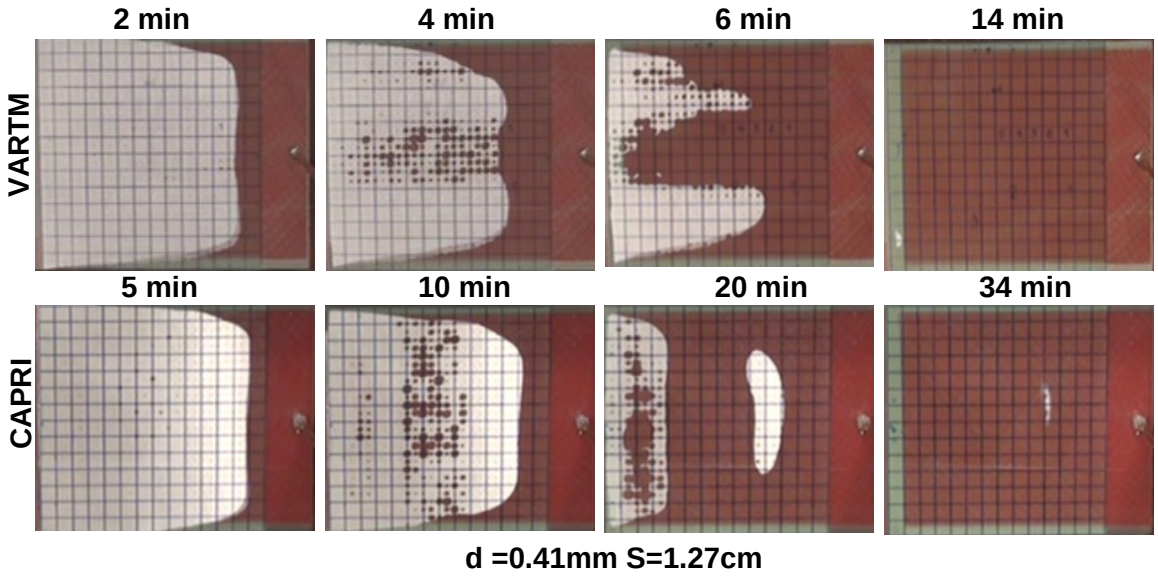

Figure 3.28 Comparison of flow patterns on the bottom surface of hybrid preforms in the VARTM (top) and CAPRI (bottom) processes for flow pathway hole diameter of 0.41mm with pathway spacing of 1.27 cm.

For the CAPRI process, at 10 minutes, fluid appears on the bottom surface concentrated around the center of the preform perpendicular to the flow direction. Despite the fact that the same flow pathway diameter and spacing were used in both processes, the infiltration patterns are quite different. A possible explanation for this can be the reduced injection pressure used during the CAPRI process which results in less preform relaxation and thickness variation compared to the VARTM process. This certainly could impact the flow patterns.

Table 3.2 shows the total infiltration times for the VARTM and CAPRI processes for different flow pathway hole diameters and spacing configurations. An interesting result can be seen from this Table is that, for the VARTM process, the case of d =0.83 mm and S= 2.54 cm has a total infiltration time of 8.5 minutes which was shorter than the case of d=0.41 mm and S=1.27 cm where the total infiltration time was 13.9 minutes. For the CAPRI process, the total infiltration

time was 46.8 minutes in the case of d =0.83 mm and S= 2.54 which was longer than the case of d=0.41 mm and S=1.27 cm where the total infiltration time was 33.9 minutes.

Table 3.2 Total infiltration times for the flow visualization tests.

Process Type	**Pathway Diameter and Spacing**	**Total Infiltration Time**
VARTM	d=0.41 mm, S= 2.54 cm	24+ min
	d=0.83 mm, S= 2.54 cm	8.5 min
	d=1.59 mm, S= 2.54 cm	5 min
	d=0.41 mm , S= 1.27 cm	13.9 min
CAPRI	d=0.41 mm, S= 2.54 cm	43+ min
	d=0.83 mm, S= 2.54 cm	46.8 min
	d=0.41 mm , S= 1.27 cm	33.9 min

The porosity values from Table 3.1 were 0.0008 for flow pathway hole diameter and spacing of 0.83mm and 2.54 cm, and 0.0009 for flow pathway hole diameter and spacing of 0.83mm with and 2.54 cm. One might expect that the latter case should have a shorter total infiltration time since the porosity thus the permeability of the acetate films is higher compared to former case. This agrees with the CAPRI visualization test results but not with the VARTM visualization test results. However, since the porosity and permeability values for the two cases are very close to each other, one would expect the total infiltration times to also be close. Hence, the differences are primarily due to experimental error.

3.5 Summary

Flow visualization tests were performed for the VARTM and CAPRI processes using the four different pathway configurations as given in Table 3.1. The top and bottom flow fronts were monitored using a video camera and screen shots were acquired at chosen time frames. Monitoring the top surface revealed the flow patterns and the total infiltration time for the three layers of the distribution medium used in the tests. Similarly, monitoring the bottom surface revealed the flow patterns and the total infiltration time for bottom surface of the hybrid preform. Due to the nature of the CAPRI process, it took 7-8 times longer to infiltrate the hybrid preform compared with the VARTM process.

Based on the flow visualization tests, it can be concluded that the flow pathway hole diameter and spacing do not have a significant affect on the infiltration of distribution medium or top surface of the hybrid preform. Shown in Figures 3.17 and 3.19, the total infiltration time for the distribution medium was about 30 seconds for all cases of the VARTM process. Shown in Figure 3.21, the total infiltration time for the distribution medium was about 140 seconds for all cases of the CAPRI process with the exception of flow pathway hole diameter and spacing of 0.83 mm and 2.54 cm case which had a higher infiltration time.

The flow pathway hole diameter and spacing have a significant effect on the infiltration of the hybrid preform which was observed by the monitoring the preform bottom surface flow fronts. Both the flow patterns and the total infiltration times vary depending on the flow pathway hole diameter and spacing. Increasing the pathway diameter and spacing helped to reduce the total

infiltration time for the hybrid preform in both processes. As the flow pathway hole diameter was increased, resin infiltration of the hybrid preform became dominated by transverse flow through the acetate films and glass fabrics.

For the flow pathway hole diameter and spacing of 0.41 mm and 2.54 cm case, Figure 3.26 shows that complete infiltration of the hybrid preform cannot be achieved because fluid reaches the vacuum port before the hybrid preform was completely infiltrated, and the test was stopped. Hence, with this flow pathway configuration, the flow rate is not high enough to completely infiltrate the hybrid preform.

In the following chapters, the preform compaction and permeability characterizations will be presented and the results will be used as input parameters to the VARTM and CAPRI flow simulation models for the FMLs. The flow patterns predicted by the simulation models will be compared with the results of the flow visualization experiments in Chapter 6.

CHAPTER 4

PREFORM COMPACTION

4.1 Introduction

Due to the flexible nature of the vacuum bag, there is no direct control over the thickness or fiber volume fraction of the composite part in the VARTM procedure. The compaction of the reinforcement preform is complex and depends on the compressibility and relaxation of the reinforcement under pressure, and the interaction between the reinforcement and the resin flow. Many researchers [12-27], [56-60] have conducted numerous studies to investigate the compaction behavior of the preform during the VARTM process. The flexible nature of the vacuum bag, coupled with the varying pressure inside the mold cavity, results in laminates with a nonuniform final thickness. Rigas et al. [61], Grimsley et al. [62, 63] and Govignon et al. [64] investigated variations of the final thicknesses in composite parts manufactured by the VARTM process. It was found that the final cured thickness of a part changes along the resin progression direction. As the distance from the vacuum source increases, the part thickness increases, and correspondingly, the fiber volume fraction of the laminate decreases. Summerscales et. al. [56] and Grimsley et al. [62, 63] conducted experimental studies to track the thickness change of the preform during the VARTM process. It is well accepted that during the flow of the resin in the fiber preform, the total compaction pressure is shared by the resin pressure and the pressure supported by the fiber network [14, 65]. Therefore, the following equation is introduced to account for the transverse equilibrium inside the mold cavity during impregnation [66]:

$$P_c = P_r + P_n \tag{4.1}$$

where, P_c is the total compaction pressure, P_r is the resin pressure and P_n is the effective compressive stress in the preform. For the VARTM process, the external pressure applied is the atmospheric pressure.

The normal strain in the preform along the transverse direction (ε) is a function of the net pressure applied to the preform. There is no general constitutive model which can fully describe the response of the reinforcement under the compression force. Thus, compaction tests are conducted to determine curves of compressive strain versus compression pressure. With the initial fiber volume fraction of the preform (V_{f0}) and thickness of the panel (t_0) given, the fiber volume fraction V_f, displacement w, and thickness t can be found by solving the following equations:

$$w = \int_{y=0}^{t_0} \varepsilon \, dy \tag{4.2}$$

$$t = \int_{y=0}^{t_0} (1+\varepsilon) \, dy \tag{4.3}$$

$$V_f = V_{f0} \frac{t_0}{t} \tag{4.4}$$

Since a general constitutive model is not available, the relationship between the compressive strain in the preform and the applied pressure was obtained by fitting the compaction test results to an empirical model. This will be shown in Section 4.4.2. Two important phenomena were observed during the compaction experiments. First, because of the resin lubrication effect [21,

22, 25], the wet fiber sample saturated with resin was compacted more than the dry reinforcement under the same pressure. Second, the compressive response of the preform under the compaction force was not elastic, and the hysteresis occurs during the unloading process [61, 62, 63].

During the VARTM process, before resin injection, the dry reinforcement is under vacuum compression. Thus, the compressive strain of the preform can be calculated from the compaction response of the dry preform during the loading process. After the resin passes, the local net pressure applied to the preform decreases as a result of the increasing resin pressure. This is equivalent to an unloading process. Accordingly, the strain in the wet preform was determined by the compaction response of the resin saturated preform during the unloading process. Therefore, the compressive strain varies with the net pressure applied to the preform as follows:

$$\varepsilon = \begin{cases} f_1(P_n) & \textit{dry compaction, loading} \\ f_2(P_n) & \textit{wet compaction, unloading} \end{cases} \tag{4.5}$$

For a standard VARTM process, the resin pressure is maintained at 1 atm in the injection reservoir and 0 atm at the flow front (vacuum side). Figure 4.1 presents the two different effects of resin flow on the compaction behavior of the preform. Before infiltration, the dry condition exists (4.1a), the preform essentially supports the external pressure, $P_n = P_{atm}$ and a maximum debulking deformation of the preform is reached. During infiltration, two deformation mechanisms are present in the wet area of the preform: wetting compaction (4.1b) and the springback (4.1c). The wetting compaction is caused by rearrangement of the fiber network,

created by the lubrication effect of the wetting fluid [63]. Under a given external pressure, lubrication of the dry preform will cause an increase in preform compaction (ε) by an additional amount of wetting deformation (ε_w). On the other hand, the presence of the resin leads to an increase of the local resin pressure (P_r). According to Equation 4.1, the net pressure applied to the preform P_n has to decrease since the total external pressure was constant (P_{atm}). Consequently, the preform compaction (ε) decreases by an amount of springback deformation (ε_s). The two competing mechanisms, wetting compaction and springback, work together to determine the local preform compaction behavior. It is clear that at any time during the infiltration process, the local compaction behavior of the preform will depend on the relative magnitude of the wetting and springback deformation mechanisms.

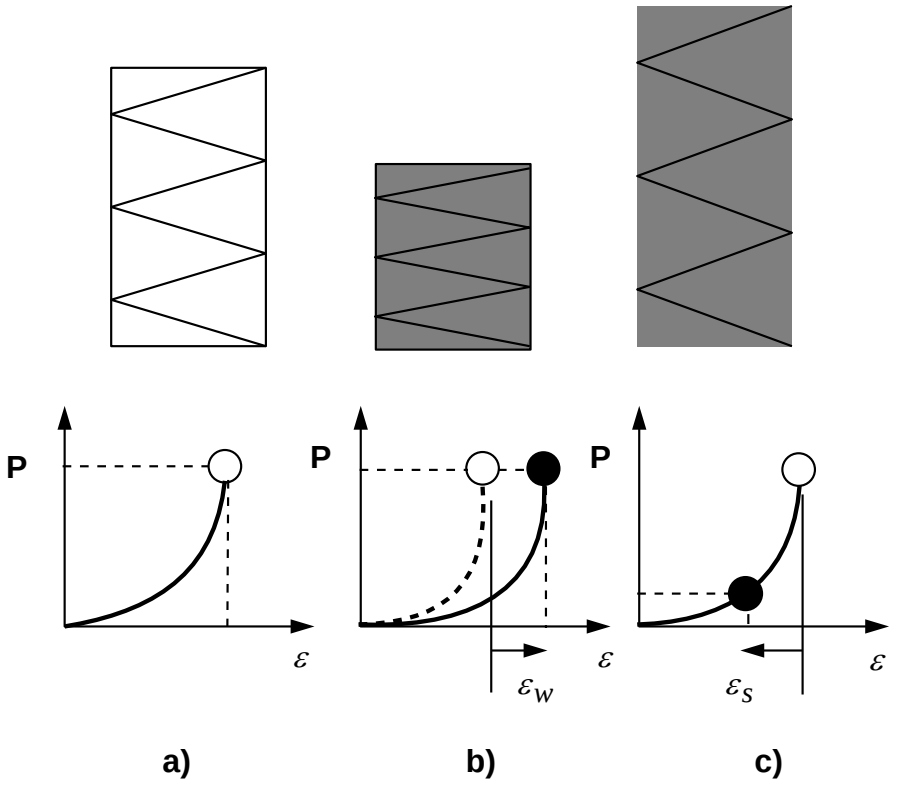

Figure 4.1 Compaction mechanisms during VARTM, a) dry compaction, b) wetting compaction and c) spring back.

For verification of the compaction test procedures, SAERTEX® MAWK (multi axial warp knit) preforms were used since data for MAWK fabric was available from an earlier study by Grimsley [67]. The compaction response and the preform permeability are coupled by the state of the preform, such as the fiber volume fraction and the saturation.

In this study, the compaction of hybrid fiber/metal preform specimens containing multiple stacks was characterized. The experiments were conducted over the range of compaction pressures found in typical VARTM conditions. The resulting experimental data was fit to empirical equations which can be used as material input parameters in process model simulations.

4.2 Materials

For the compaction tests, the materials tested are listed below:

- MAWK (multi axial warp knit) carbon fabric. It is composed of seven plies of AS-4 and IM-7 carbon fibers; single-stack with total areal weight of 1423 g/m^2 and fiber density of 1.78 g/cc. The plies are stacked, not woven, and then knitted with an alternating polyester tricot/chain knit thread.
- S2 glass fabric; style 6781 8-harness satin weave. It was supplied by US Composites with areal weight of 293.5 g/m^2 and fiber density of 2.49 g/cc.
- Distribution medium; Resinflow 60 LDPE/HDPE blend was supplied by AIRTECH Advanced Materials Group.

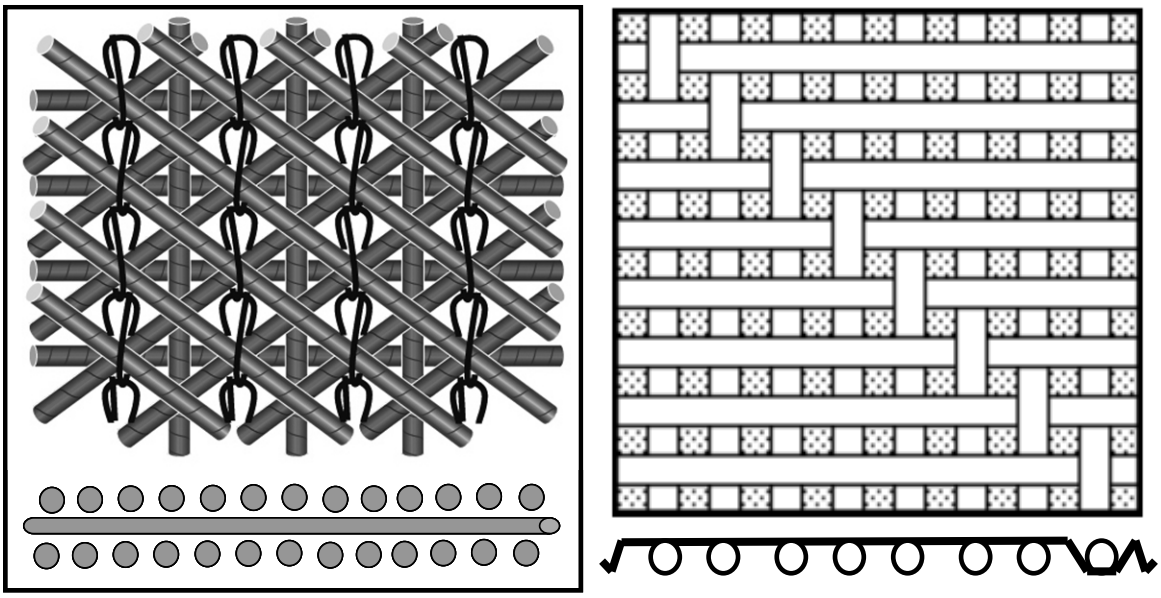

Figure 4.2 Schematic diagrams of the fabrics tested. Shown on left is MAWK (multi axial warp knit) carbon fabric and shown on right is 8-harness satin weave S2 glass fabric.

The wetting fluid used the wet compaction tests was SAE 40W oil. It had a viscosity of 0.24 Pa.s and density of 709 kg/m^3. A schematic diagram of the tested fabrics is shown in Figure 4.2.

4.3 Preform Compaction Characterization

4.3.1 Test Fixture

The experiments were conducted under both dry and wet conditions to measure the compaction response of the hybrid fiber/metal preforms at the low pressures experienced during VARTM processing. The compaction test fixture was composed of two flat plates used to compact the samples. The upper plate had dimensions of 15.2 cm x 15.2 cm, and the lower plate had dimensions of 15.2 cm x 35.6 cm. The plates were cut from 1.27 cm thick tool steel. The lower plate had four circular alignment pins inserted to hold the samples in place. Both a laser displacement sensor (L-Gage) and a digital dial indicator were used to monitor the crosshead

displacement and thus the thickness of the sample being tested. A schematic diagram of the compaction test setup is shown in Figure 4.3.

The fixture mounts between upper and lower platens of a MTS Insight 100 kN Material Testing Machine. The MTS machine was computer controlled by the software TestWorks. The software allowed the user to create custom programs to control the machine. Two TestWorks software programs were created, one for static (step-by-step) compaction and the other for dynamic (continuous) compaction of the samples.

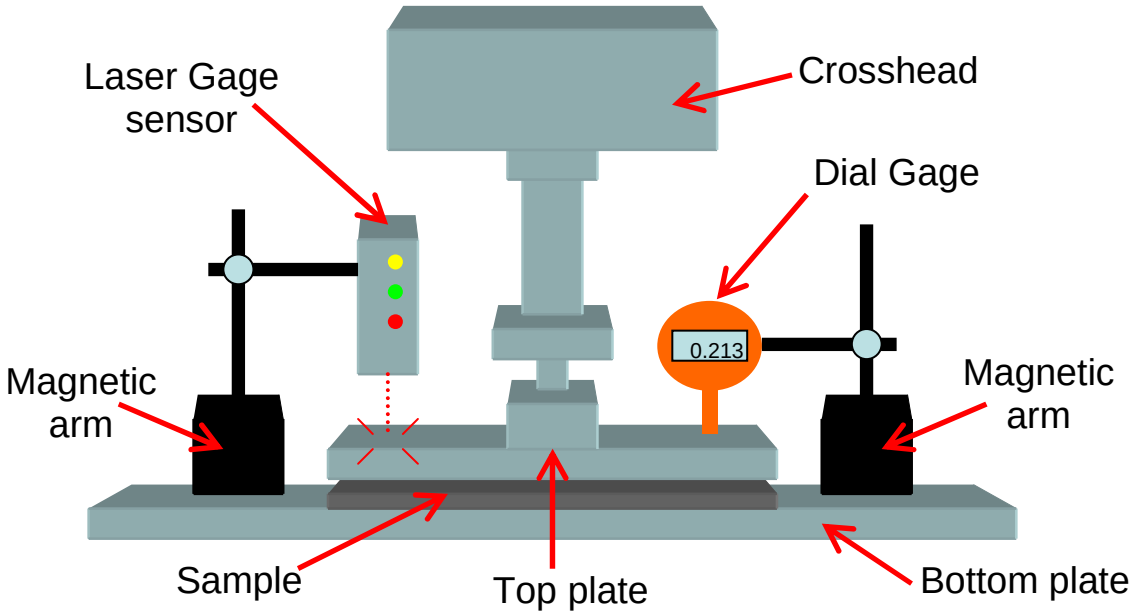

Figure 4.3 Schematic diagram for the compaction test setup.

Figure 4.4(a) shows the main screen for the TestWorks software and Figure 4.4(b) shows the LabVIEW screen for collecting data from the sensor. Instantaneous load and extension (crosshead displacement) readings can be seen on the TestWorks screen. The LabVIEW screen shows the change in the output voltage of the sensor which is converted to displacement (compaction) of the preform.

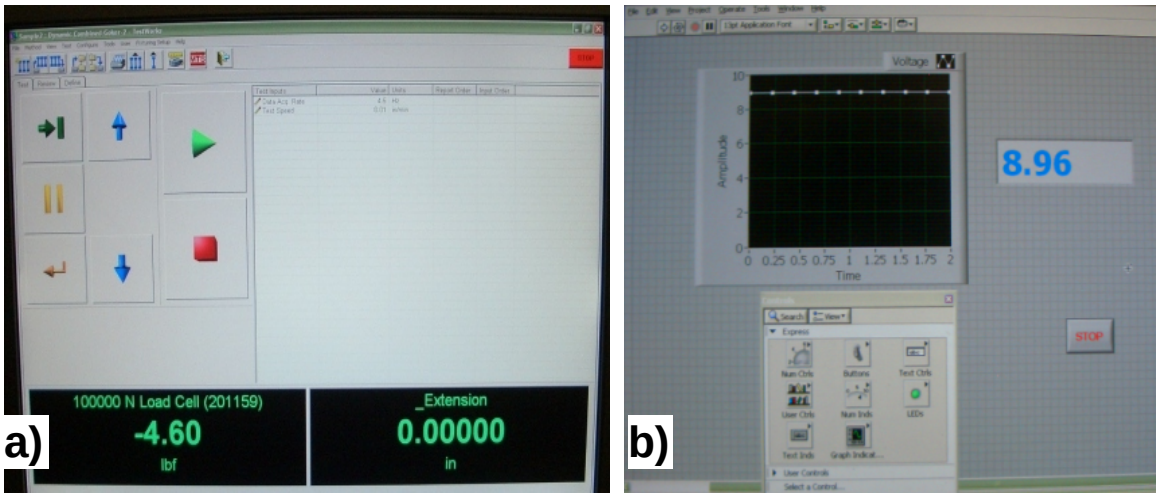

Figure 4.4 TestWorks(a) and LabVIEW (b) software screen shots.

4.3.2 Dynamic Compaction Test Procedures

The program for dynamic testing applies an increasing compressive load up to a set high load limit and then releasing this load down to a set low load limit. The test cycle is decomposed into two cycles*: Loading* and *Unloading*. Both of these cycles were performed with a constant crosshead speed (mm/min). The user inputs to the test program are: high load limit, low load limit, crosshead speed, and data acquisition frequency. The TestWorks program records the crosshead position and load data and saves it in a text file.

The test procedure for dynamic testing will be explained in more detail here. First, the MTS machine was calibrated using the TestWorks software after attaching the fixture (two steel plates) on to the machine platens. After the calibration, the cross head was lowered all the way down until it touches the bottom plate. At this point, the extension reading of the machine was zeroed. The dial indicator was also placed on the upper plate and zeroed at this position. Then,

the crosshead was raised and the sample to be tested was placed on the bottom plate. The crosshead was manually and slowly lowered until the upper plate touches the sample and a minimal initial load (5-10 N) was attained. At this position, the readings from the dial indicator and the machine were recorded, since they both indicate the initial thickness of the preform. The dial indicator, a Mitutoyo Digimatic Indicator with a resolution of 0.001 mm, was used to verify the machine readings. The laser displacement sensor (L-Gage) was used to monitor the displacement of the fixture. The compaction fixture setup with the L-Gage sensor on left and with the dial indicator on right is shown in Figure 4.5.

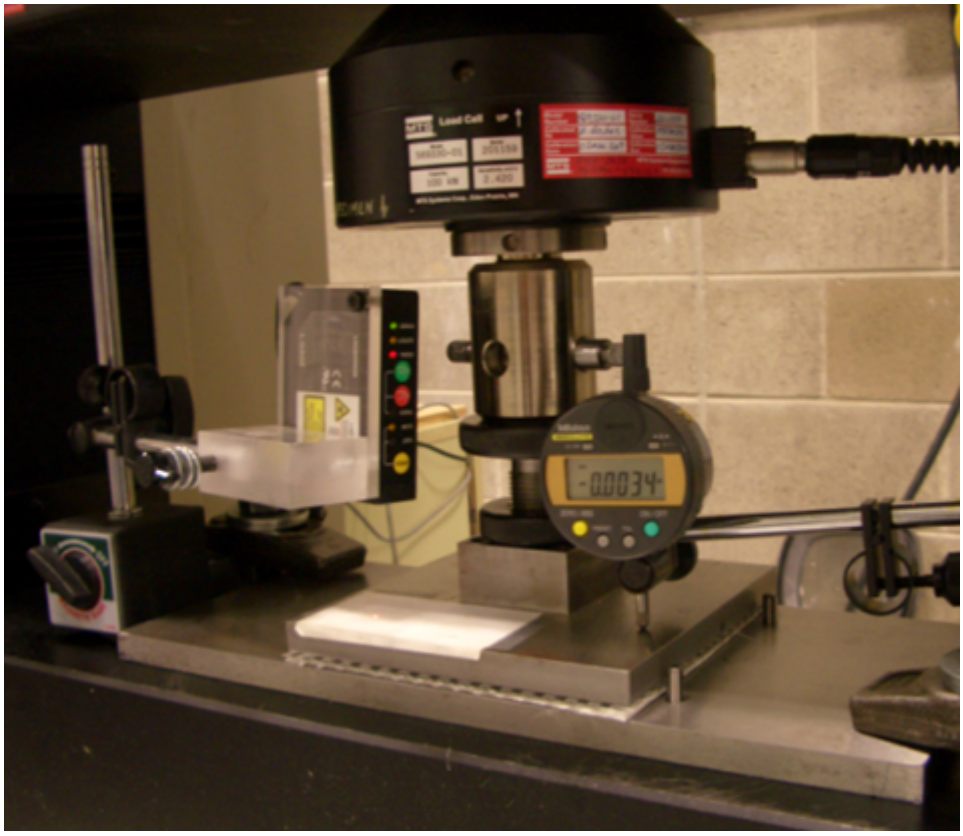

Figure 4.5 Dry compaction of carbon fabric.

The L-Gage sensor was obtained from Banner Engineering, model number LG5A65NUQ and has a range of 15.2 mm. The output data of the displacement sensor was acquired using LabVIEW. The L-Gage sensor was mounted above the upper plate of the compaction test fixture as shown in Figure 4.5. A piece of white paper was glued onto the upper plate to minimize reflections, which might be caused by the steel surface. Before using the L-Gage sensor, it must be calibrated by defining the minimum and maximum distance limits or distance range. A distance range of 12.7 mm (0.5 in.) was used in this study. Precision gage blocks were used to set the minimum and maximum distance limits.

A constant strain rate of 0.127-0.508 mm/min was used for compacting the preform specimens. Specimens of 15.2 cm x 15.2 cm were loaded to 2.67 kN, which corresponds to the maximum VARTM compaction pressure of 101.5 kPa. Once the maximum load limit was reached, the crosshead began unloading the specimen until the load dropped to the lower load limit of 0 N. The data acquisition rate was 4.5 Hz, which matches the sampling frequency of the L-Gage sensor.

4.3.3 Static Compaction Test Procedures

The static compaction experiments were performed using the MTS load frame and the same test fixture used in the dynamic tests. In the static compaction tests, samples were compressed at a constant crosshead speed until a specified load was reached. When the specified load was reached, the crosshead was stopped. The MTS Insight test machine holds the crosshead extension constant but does not maintain the load fixed. Hence, the instantaneous load on the

preform decreases over time due to relaxation of the preform. A two minute relaxation period was observed after each specified load point was reached. After the two-minute hold, the crosshead extension, MTS load cell force and preform thickness were measured and recorded.

In the static tests, the initial preform thickness was measured using either the L-Gage laser displacement sensor or the dial indicator. The crosshead extension at the specified load intervals was recorded by the digital indicator and the machine. The static test program for the MTS load frame was created using the TestWorks software. The test program requires the user to enter the minimum load, maximum load, the load increments, and the crosshead speed (strain rate).

At the beginning of the test, the load was increased from the initial preload (minimum load) to the first load increment and held constant for two minutes as mentioned in the previous paragraph. After the two minute hold, the MTS applied load and crosshead extension, and the preform thickness was recorded. The crosshead was then moved to the next load increment at the specified rate, held for two minutes, and the applied load, crosshead extension and preform thickness measured.

The procedure was repeated until the maximum load was reached. Once the maximum load was reached, the preform was unloaded at the same crosshead speed until the minimum load was reached. During unloading, at each load increment, the crosshead was again held constant for two minutes and the applied load, crosshead extension and preform thickness were measured.

4.3.4 Data Analysis

Since a general constitutive model was not available, the relationship between the compressive strain in the preform and the applied pressure was initially obtained by fitting the compaction test results to an empirical model using Equation 4.5. The form of the compaction equation depends on the type of preform [60].

In this study, preform compaction data will be presented by constructing a curve of fiber volume fraction as a function of pressure. The preform thickness was converted to fiber volume fraction, V_f, using the following equation:

$$V_f = \frac{FAW}{t * \rho_F} \tag{4.6}$$

where, *FAW* was the fiber areal weight of the preform, *t* was thickness, and ρ_F was the fiber density. The compaction pressure was determined by simply dividing the measured load by the preform cross sectional area.

4.4 Results

4.4.1 Multi-Axial Warp Knit (MAWK) Carbon Fabric

Multi axial warp knit (MAWK) carbon fabric compaction tests were performed to compare the results of the present study with the MAWK fabric data previously measured by Grimsley [67]. Grimsley used a vacuum bag technique to compact the preform to the specified pressure settings. Results of the compaction experiments performed by using the current procedures (static and dynamic tests) were compared with Grimsley's data in Figure 4.6 for the 2-stack MAWK

preform and Figure 4.7 for the 4-stack MAWK preform. Shown in Figure 4.8 is a comparison between the compaction behavior of a 4-stack MAWK preform measured using the dynamic test procedure and Grimsley's data. The crosshead speed used was 0.254 mm/min.

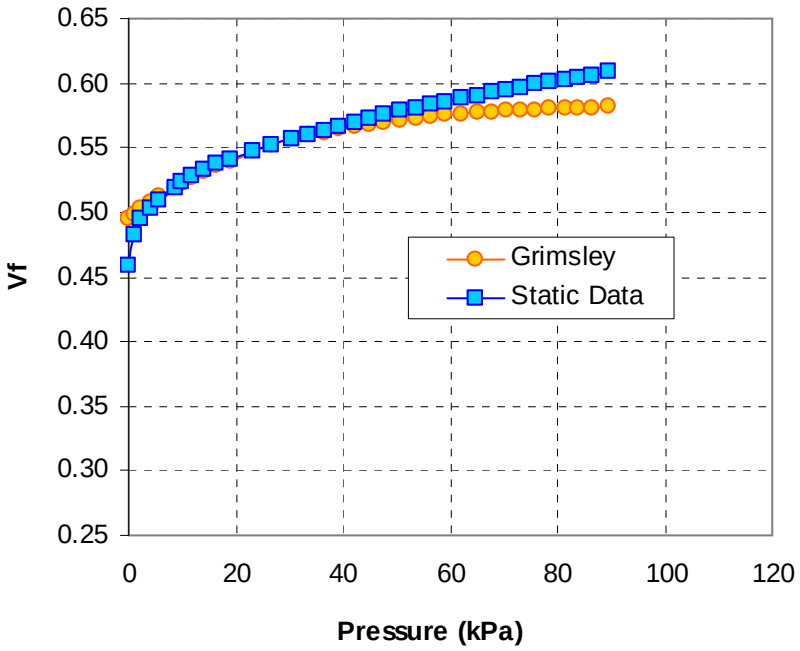

Figure 4.6 Fiber volume fraction vs. compaction pressure for loading of a dry 2-stack MAWK preform. Comparison between the static test method and data of Grimsley [67].

There was good agreement between test methods of the 4-stack MAWK preform except for the initial fiber volume fraction at minimal pressure. This may be due to slight differences in the initial thickness measurements. For the 2-stack MAWK preform, there was some deviation in the fiber volume fractions at higher compaction pressures. This can be attributed to the different testing procedures used. To compact the preforms, Grimsley used a vacuum bag technique whereas a compaction fixture was used in the current study as explained in Section 4.3.1. The results of Grimsley's tests plotted in the Figures 4.6-4.8 were taken from a best fit equation of multiple data sets, which may have also contributed to the differences observed in the present data and Grimsley's data.

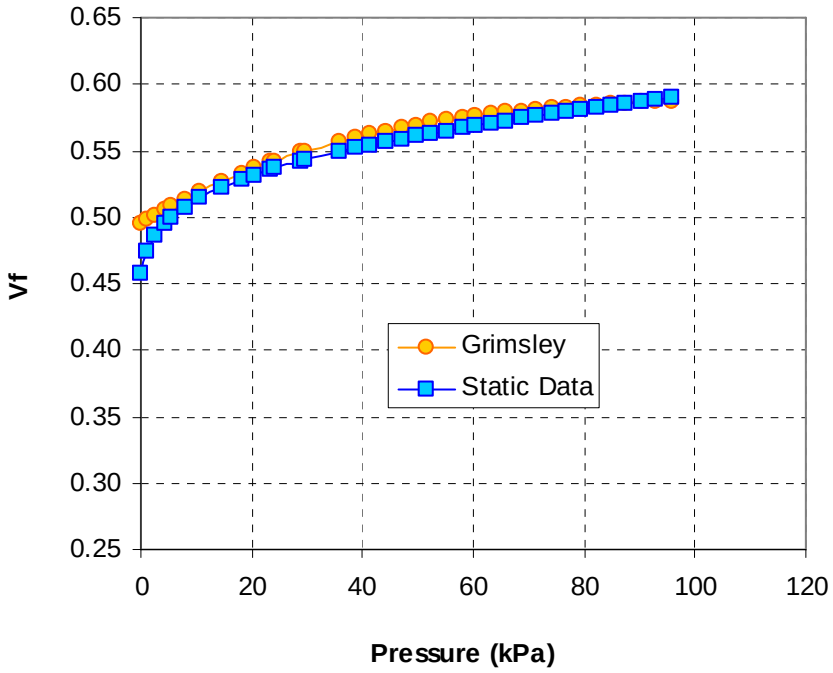

Figure 4.7 Fiber volume fraction vs. compaction pressure for loading of a dry 4-stack MAWK preform. Comparison between the static test method and data of Grimsley [67].

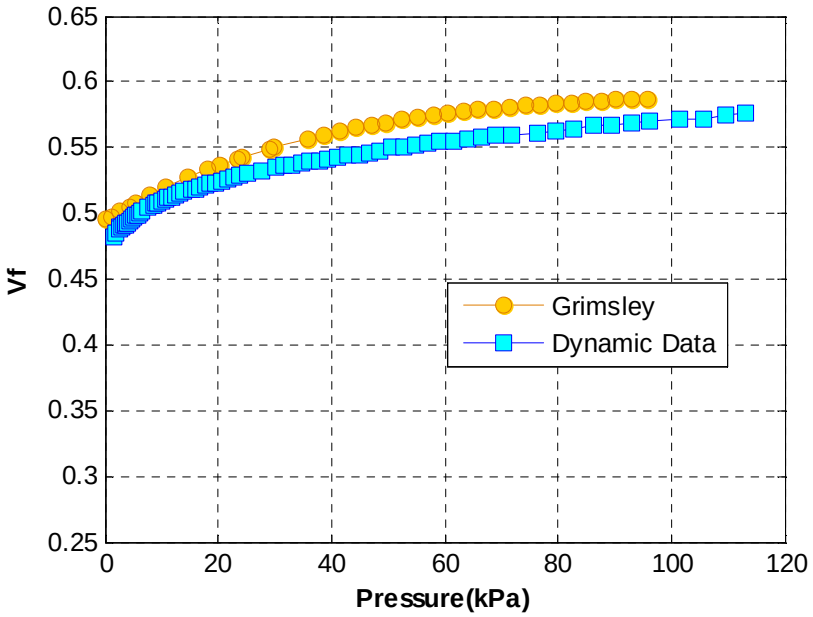

Figure 4.8 Fiber volume fraction vs. compaction pressure for loading of a dry 4-stack MAWK preform. Comparison between the dynamic test method and data of Grimsley [67].

Shown in Figure 4.9 is a comparison between the static and dynamic test procedures for the 4-stack MAWK preform. The data for both loading and unloading compare well with some differences occurring at the low compaction pressures. As in the case shown in Figure 4.8, this was due to the differences in initial thickness measurements of the preforms in two different tests.

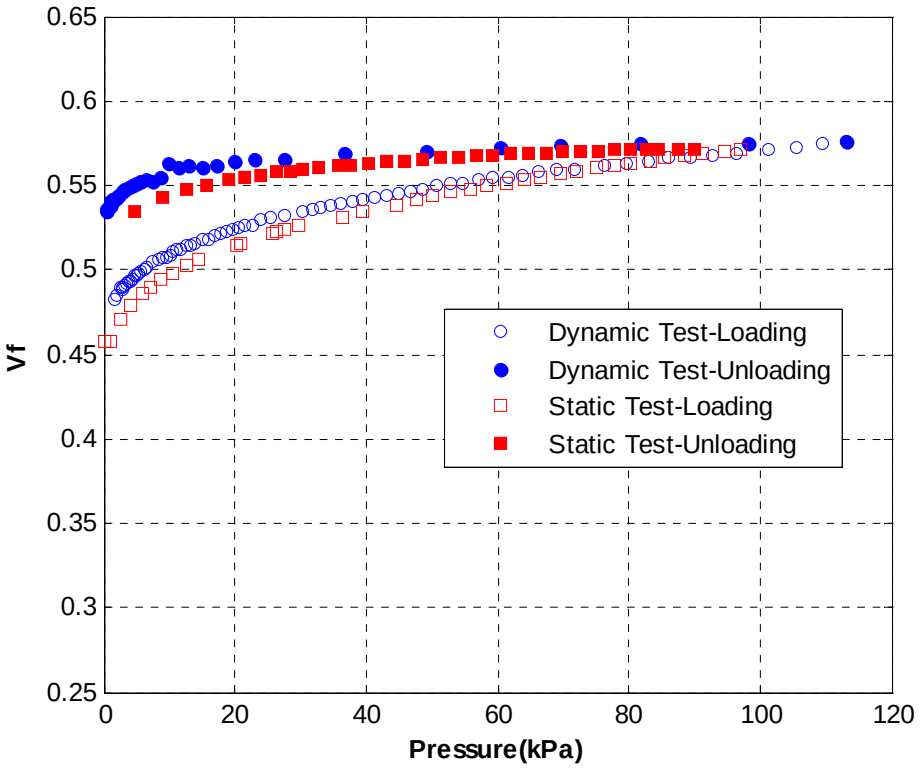

Figure 4.9 Fiber volume fraction vs. compaction pressure for a dry 4-stack MAWK preform. Comparison between the dynamic and static test methods during loading and unloading.

A comparison between dry and wet compaction for a 4-stack MAWK carbon fiber preform is shown in Figure 4.10. Dynamic compaction test method was used. As expected, the MAWK fabric becomes more compressible and the fiber volume fraction increases for the wet preform, since the fluid has a lubricating effect on the fibers being compressed [21, 22, 25].

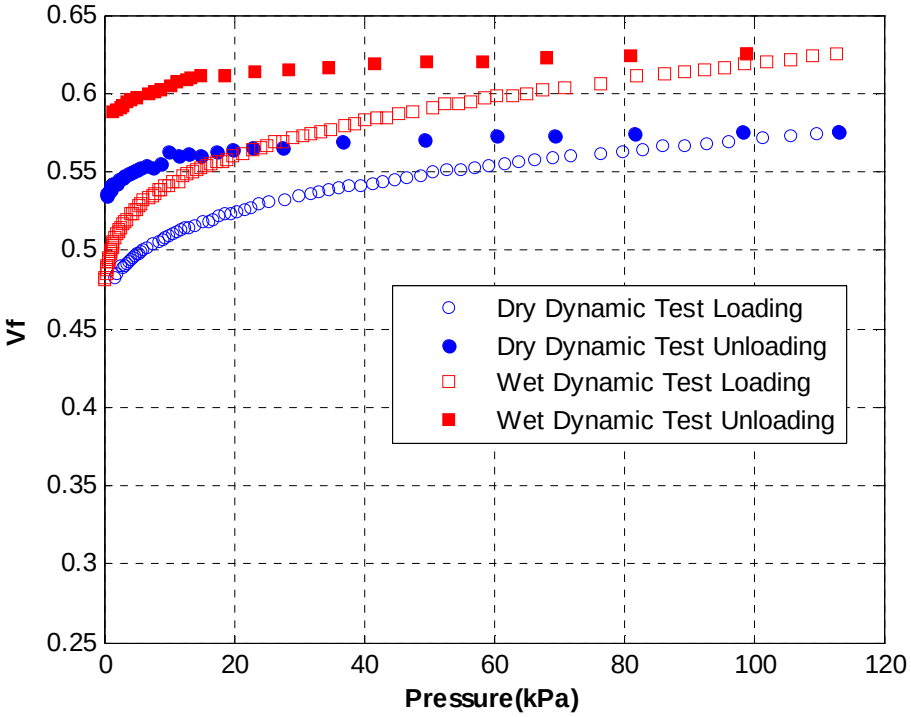

Figure 4.10 Fiber volume fraction vs. compaction pressure of 4-stack MAWK preforms. Comparison between loading and unloading for dry and wet (fluid saturated) preforms.

4.4.2 S2-Glass Fabric

Compaction experiments for 8-harness satin weave S2-glass fabric were performed using both the static and dynamic test procedures. All specimens tested were 8 layers thick and the crosshead speed was 0.254 mm/min unless otherwise noted. The compaction behavior of the S2-glass fabric during loading and unloading using the static compaction test method is shown in Figure 4.11. The results for two test samples compare well. A comparison between the static and dynamic test method is shown in Figure 4.12. At low crosshead speeds, the dynamic test result agrees well with the static test results.

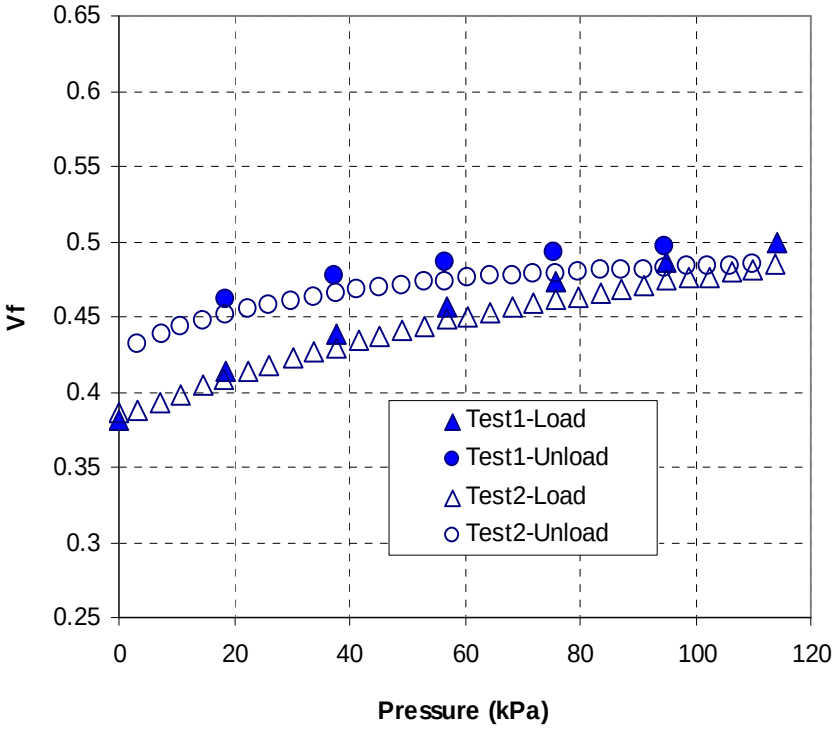

Figure 4.11 Fiber volume fraction vs. compaction pressure for an 8-layer, S2-glass preform. Comparison between two static tests at 0.254 mm/min.

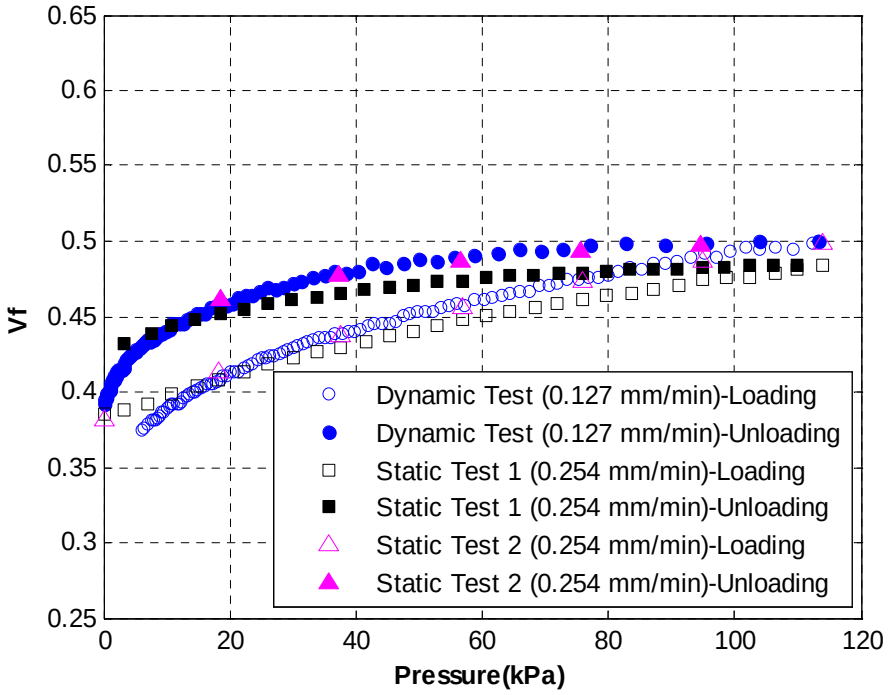

Figure 4.12 Fiber volume fraction vs. compaction pressure for an 8-layer, S2-glass preform. Comparison between the static and dynamic test methods.

The effect of crosshead speed on dynamic compaction of S2-glass preform for both loading and unloading conditions is shown in Figure 4.13. As the crosshead speed increases, the fiber volume fraction at a specified compaction pressure decreases. These results were consistent with observations in previous investigations [22, 25]. A possible explanation was that at higher crosshead speeds, there was less time for fibers to redistribute and nest. Further, there may be a strain rate effect on the transverse stiffness of the S2-glass fiber.

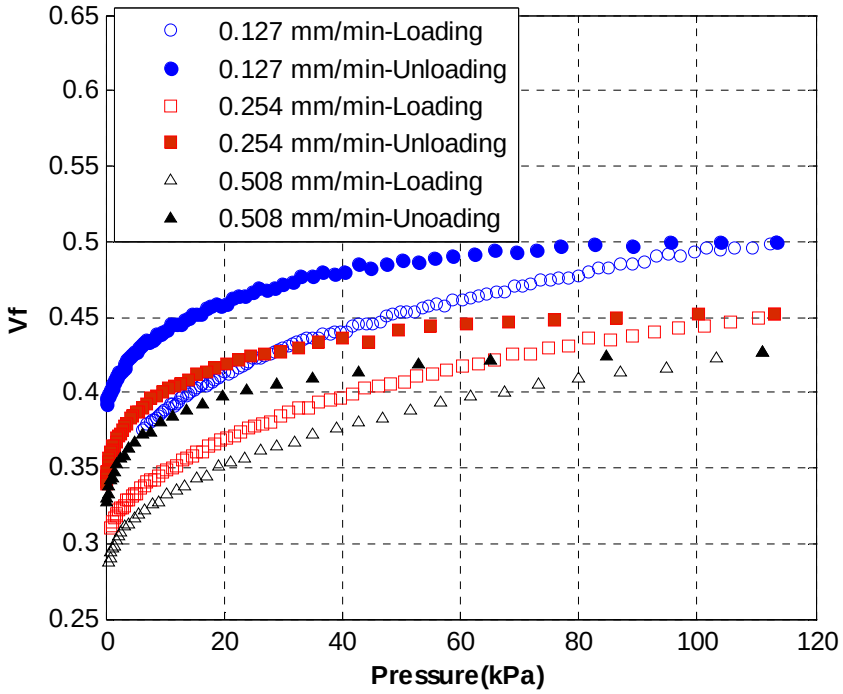

Figure 4.13 Fiber volume fraction vs. compaction pressure for an 8-layer, S2-glass preform. Comparison between dynamic compaction tests at different crosshead speeds.

A comparison between dry and wet compaction of the S2-glass preform loaded at 0.254 mm/min is shown in Figure 4.14. Similar to the results of the multi axial warp knit (MAWK) carbon fabric, the lubrication effect causes the fluid saturated preform to achieve a higher fiber volume fraction at a given compaction pressure than the dry preform.

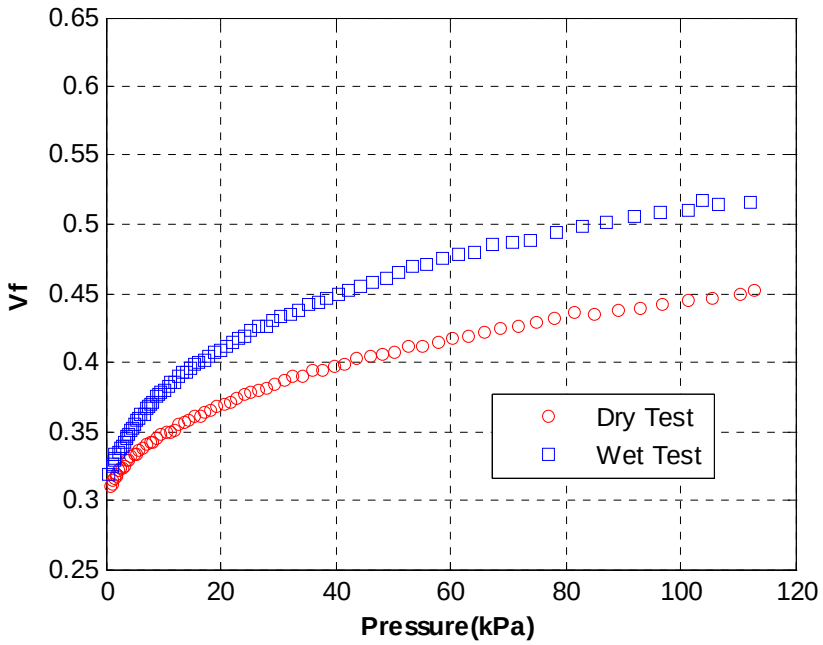

Figure 4.14 Fiber volume fraction vs. compaction pressure for an 8-layer, S2-glass preform. Comparison between dry and wet (fluid saturated) preforms tested at 0.254 mm/min.

Looking at the S2 glass fabric compaction test results up to this point, it can be concluded that the dynamic test procedure can be used to determine the basic compaction behavior of a dry and wet fibrous preforms during both loading and unloading. However, the crosshead speeds must be relatively slow. In the present study, dynamic tests with crosshead speeds in the range of 0.127 mm/min–0.254 mm/min show compaction data that agree well with data obtained using a static test method. Figures 4.15 and 4.16 show wet (fluid saturated) tests at 0.127 mm/min and at 0.254 mm/min respectively. Two tests are shown for each speed. As expected, the test with the higher crosshead speed shows lower fiber volume fractions at a given pressure, when compared to the test with the slower speed. The maximum fiber volume fraction at highest pressures for the two tests shown in Figure 4.15 is between 0.57 and 0.58 whereas the maximum volume fraction drops to between 0.49 and 0.52 when the testing speed is doubled as shown in Figure 4.16.

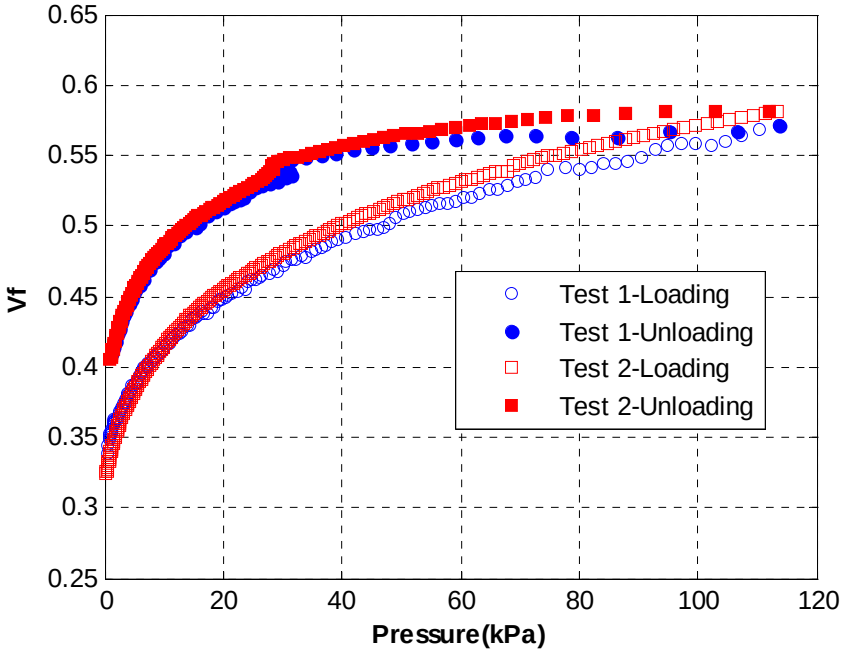

Figure 4.15 Fiber volume fraction vs. compaction pressure for an 8-layer, S2-glass preform. Comparison between two wet (fluid saturated) tests at 0.127 mm/min.

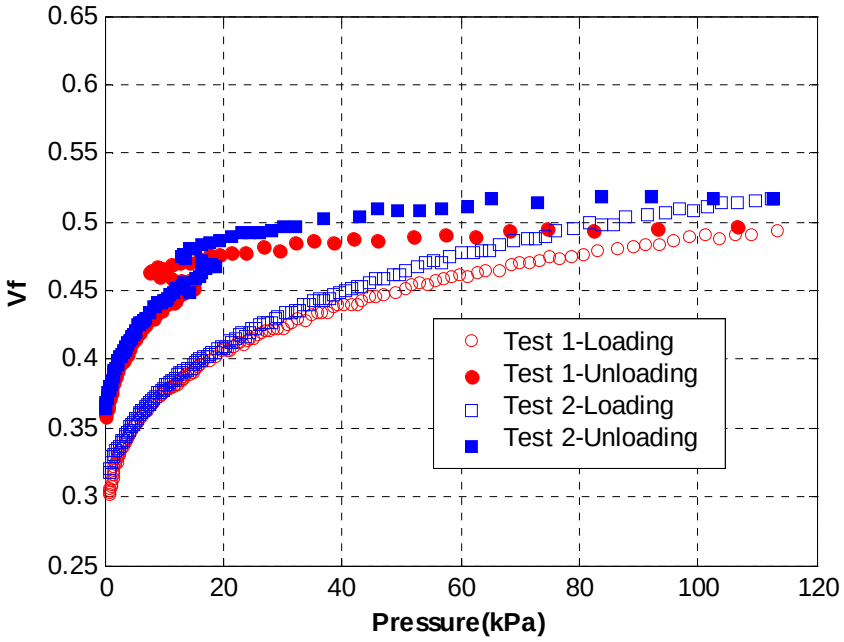

Figure 4.16 Fiber volume fraction vs. compaction pressure for an 8-layer, S2-glass preform. Comparison between two wet (fluid saturated) tests at 0.254 mm/min.

Looking at the fiber volume fractions at a given pressure in Figures 4.15 and 4.16, it is seen that they are higher when compared to the dry tests under the same testing conditions. The dry test at 0.127 mm/min reaches a maximum fiber volume fraction of about 0.50 compared with the wet (fluid saturated) test at the same speed reaching a maximum fiber volume fraction of about 0.58. A similar trend is observed for the higher speed tests at 0.254 mm/min; the dry one in Figure 4.13 has a maximum fiber volume fraction of about 0.45 whereas the wet test in Figure 4.16 has a maximum fiber volume fraction of about 0.50 or higher. This verifies the lubrication effect and the resulting increase in fiber volume fraction as demonstrated in Figure 4.14.

A discontinuity is observed in the fluid saturated compaction curves during unloading. Taking a closer look at the unloading curves, it is seen that these discontinuity occurs at around 30 kPa for the tests in Figure 4.15 and at around 15 kPa for the tests in Figure 4.16.

In the compaction tests, with the effect of the wetting fluid, the preform layers tend to stick to either the upper or the lower plate of the compaction fixture. During the unloading stage, as the upper and lower plates move away from each other, the nested individual preform layers start to separate from each other at some loading point. Once the separation starts, due to the pressure gradient created between the ambient pressure and the pressure held within the nested preform, more wetting fluid flows through the preform and this causes an overall pressure increase, and thus an increase in fiber volume fraction as seen in the unloading curves. The discontinuity becomes more noticeable in the higher speed test of Figure 4.16 and occurs at lower pressures compared to the slower speed test of Figure 4.15. This can be related to the speed effect on the compaction of fabrics as less nesting was expected to occur at higher speeds.

Figures 4.17 and 4.18 show the dry loading and wet (fluid saturated) unloading curves, respectively, for 8 layers of S2-glass tested at 0.127 mm/min. A new sample was used in each test. A best fit curve was drawn for the data sets in each figure using the mathematical model shown in Equation 4.7 below. The slight differences in compaction curves were again due to the initial fiber volume fractions (starting thickness under minimum load), as this value changed slightly from one test to another. The strain was calculated from Equation 4.7 and can be converted fiber volume fraction using Equation 4.8 where $\phi_{initial}$ is the *initial porosity* of the fabric, a, b and c are the model constants, ε is the strain and P_f is the fabric pressure. The constants in Equations 4.7-4.8 were found by nonlinear regression and are given in Table 4.1.

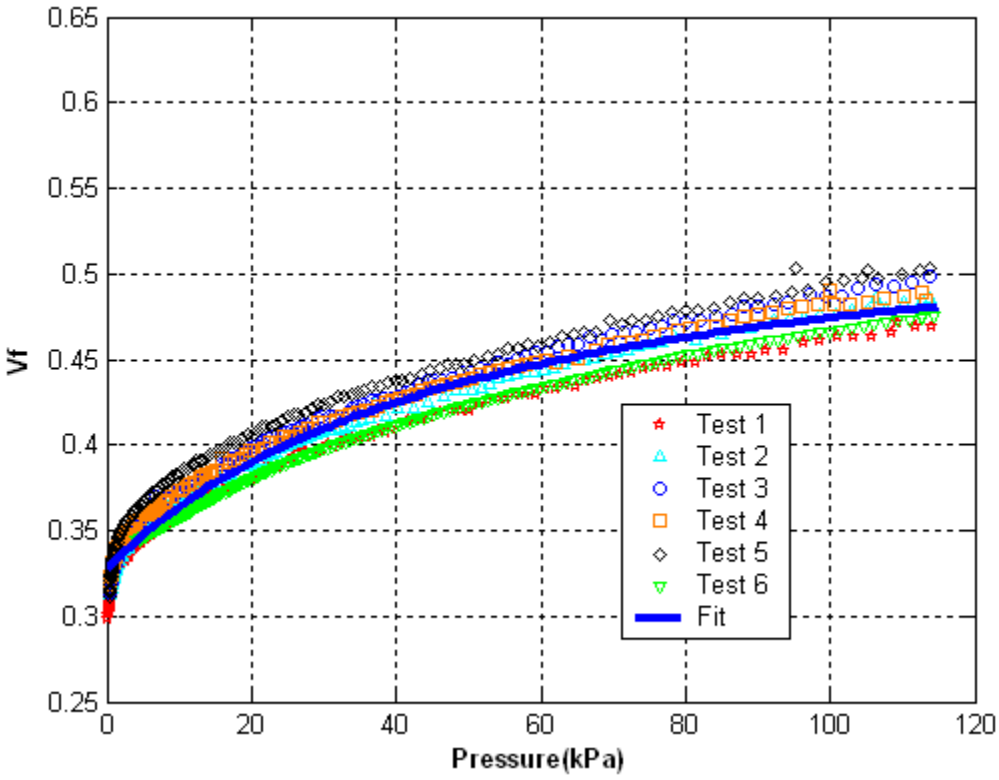

Figure 4.17 Fiber volume fraction vs. compaction pressure for an 8-layer, S2-glass preform. Comparison between loading curves six dry tests at 0.127 mm/min.

$$\varepsilon = a + b\left[\frac{P_f}{c + P_f}\right] \tag{4.7}$$

$$V_f = \frac{1 - \phi_{initial}}{1 - \varepsilon} \tag{4.8}$$

Table 4.1 Constants for the compaction fit models.

	Dry Loading	**Wet Unloading**
a	0.0828	-0.0165
b	0.3678	0.3521
c	29.607	8.970

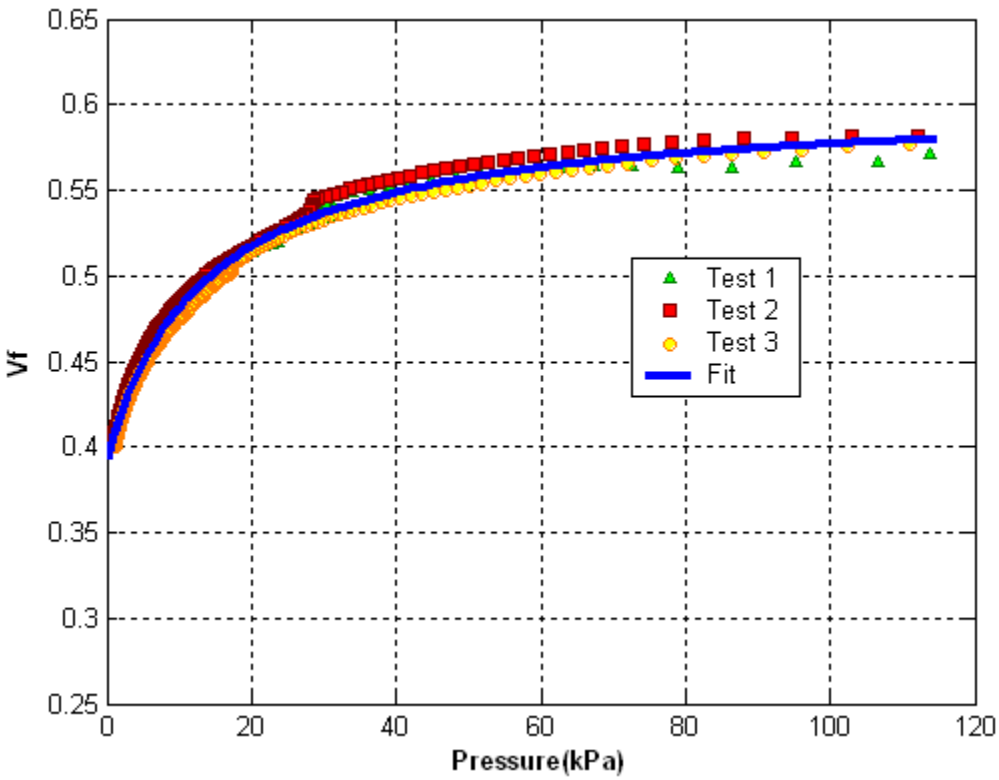

Figure 4.18 Fiber volume fraction vs. compaction pressure for an 8-layer, S2-glass preform. Comparison between unloading curves of three wet tests at 0.127 mm/min.

4.4.3 Distribution Medium

Compaction tests for 3 layers of Distribution medium (DM) were performed. The tests were performed at 0.127 mm/min using the dynamic testing method. Three layers were tested due to the fact that this was the number of layers used in VARTM flow visualization tests as explained in detail in Chapter 3. The results are shown in Figures 4.19 and 4.20. Figure 4.19 shows the fiber volume fraction versus compaction pressure and Figure 4.20 shows the fiber volume fraction versus thickness curve for the DM. This curve, as will be explained in Chapter 5, is useful in determining the thickness values corresponding to fiber volume fractions to be used in the permeability measurement tests.

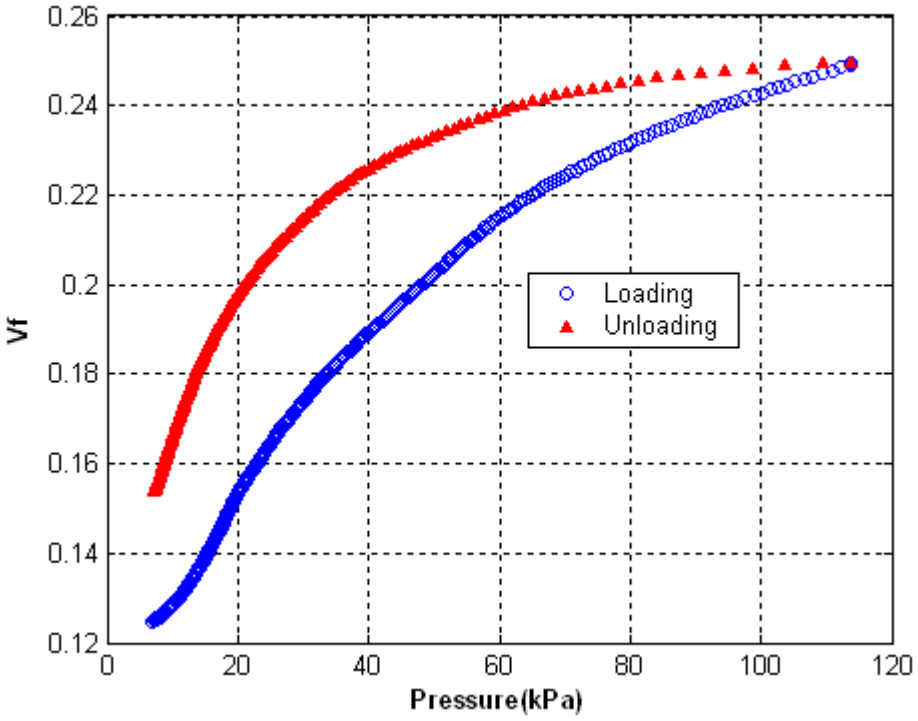

Figure 4.19 Fiber volume fraction vs. compaction pressure for a 3-layer DM.

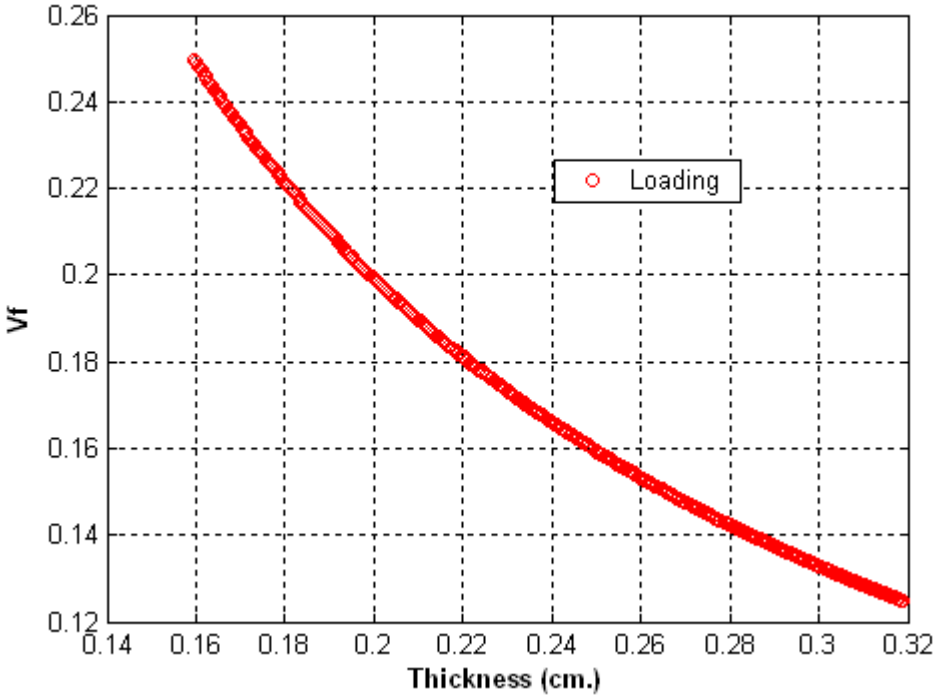

Figure 4.20 Fiber volume fraction vs. thickness (in.) for a 3-layer DM.

4.5 Summary

One of two important characterization experiments required to construct an accurate model of the VARTM/FML process is the preform compaction characterization. In this chapter, results of the preform compaction characterization tests were presented and discussed. Characterization tests were performed for the MAWK (multi axial warp knit) carbon fabric, S2 glass fabric and for the distribution medium (DM). The MAWK fabric was used for the verification of the compaction techniques employed in this study and the data was compared with an earlier study by Grimsley [67]. The measured MAWK compaction data agreed well with Grimsley's [67] data.

The compaction behavior of the S2 glass fabric was investigated under several testing conditions including dry and saturated conditions, different compaction speeds and using static and dynamic testing procedures. In the VARTM process, the preform can be modeled as being compacted when dry and then allowed to relax when infiltrated or wet. Thus, multiple sets of data gathered from the *dry loading* and *wet unloading* tests were fit to mathematical models to be used in the developed VARTM simulation models. The compaction behavior of distribution media was also measured.

CHAPTER 5

PREFORM PERMEABILITY

5.1 Introduction

Permeability is the measure of a preform material resistance to flow and relates the velocity of the infiltrating fluid to the pressure gradient within that preform. Fluid flow through a porous and permeable medium is given by the well known empirical law Darcy's Law [42]. It gives a relation between average velocity and resin pressure gradient. Three dimensional Darcy's Law for an anisotropic material can be written as:

$$\bar{q} = -\frac{S}{\eta}\nabla P \qquad \text{and in open form:} \qquad \begin{pmatrix} \bar{q}_x \\ \bar{q}_y \\ \bar{q}_z \end{pmatrix} = -\frac{1}{\eta}\begin{pmatrix} S_{xx} & S_{xy} & S_{xz} \\ S_{yx} & S_{yy} & S_{yz} \\ S_{zx} & S_{zy} & S_{zz} \end{pmatrix}\begin{pmatrix} \partial P/\partial x \\ \partial P/\partial y \\ \partial P/\partial z \end{pmatrix} \tag{5.1}$$

where $\bar{q}$ is the superficial velocity, η is the viscosity of the fluid, ∇P is the pressure gradient vector and S is the permeability tensor.

For orthotropic preforms, this relation reduces to one dimensional Darcy's Law for each direction; x, y and z as shown in Equation 5.2. In this study, x and y directions were in-plane (advancing flow) directions and z direction is the transverse (thorough thickness) direction.

$$\bar{q}_x = -\frac{S_{xx}}{\eta}\frac{dP}{dx} \quad , \qquad \bar{q}_y = -\frac{S_{yy}}{\eta}\frac{dP}{dy} \quad \text{and} \quad \bar{q}_z = -\frac{S_{zz}}{\eta}\frac{dP}{dz} \tag{5.2}$$

Preform permeability is a required input parameter for the flow model used to track the flow of resin. Thus, preform permeability characterization experiments are an essential part of the VARTM/FML simulation model.

5.2 Preform Permeability Characterization Experiments

The fibrous preforms are deformable and anisotropic porous materials. Hence, the permeability depends both on the direction of flow and the degree of compaction of the preform. In this study, the permeabilities in the principal materials directions were measured for the corresponding preforms.

The permeability measurement system was composed of a permeability fixture, constant flow rate pump, and a data acquisition system. A real time data acquisition system was composed of a DAQ board, signal conditioning and multiplexing hardware, and LabVIEW data acquisition software. Experiments were conducted to measure the in-plane (*Sxx* and *Syy*) and the transverse (*Szz*) permeabilities ranging from 35% up to 60% and the data were fit to empirical models which relate permeability to fiber volume fraction.

5.2.1 Materials

Permeability characterization tests were performed for the following materials:

- S2 glass in in-plane and transverse directions. (Style 6781 8-harness satin weave with areal weight of 293.5 g/m^2 and fiber density of 2.49 g/cc).
- Acetate films in transverse direction with three different flow pathway diameters (0.41mm, 0.83 mm and 1.59mm) and with two different spacings (0.41mm 2.54 cm and 1.27 cm).
- Distribution media (DM) in in-plane and transverse directions. (Resinflow 60 LDPE/HDPE blend resin distribution medium).

5.2.2 Permeability Test Fixtures

The test fixtures were designed to direct a one-dimensional flow of fluid through the preform to measure the in-plane (Sxx and Syy) and the transverse (Szz) permeabilities. A schematic diagram of the in-plane permeability test fixture is shown in Figure 5.1. An actual photo is shown in Figure 5.2. The fixture, fabricated from tool steel, was instrumented with diaphragm pressure sensors to measure fluid pressure in the test cavity and thickness sensors to measure the preform thickness changes.

The fixture was mounted on MTS Insight 100 kN Material Testing Machine. The fixture was designed to characterize preform specimens 15 cm in length by 15.3 cm in width, at thicknesses up to 2.5 cm. Two linear voltage differential transducers (LVDT) were mounted on opposite

ends of the fixture to ensure uniform thickness across the 15.0 cm length of the specimen. Two pressure sensors were installed in the fixture. The sensors located at the inlet and outlet sides were used to measure the inlet and outlet fluid pressures and they were required for determining the in-plane permeability under steady-state conditions. The fixture was also capable of measuring the advancing-front permeability using three pressure sensors that can be mounted in the cavity.

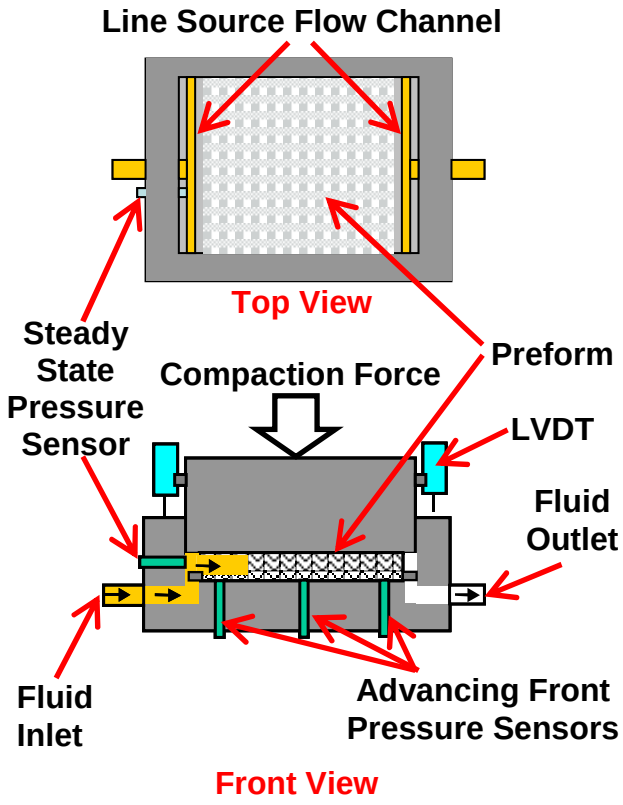

Figure 5.1 Schematic for the In-plane Permeability Fixture.

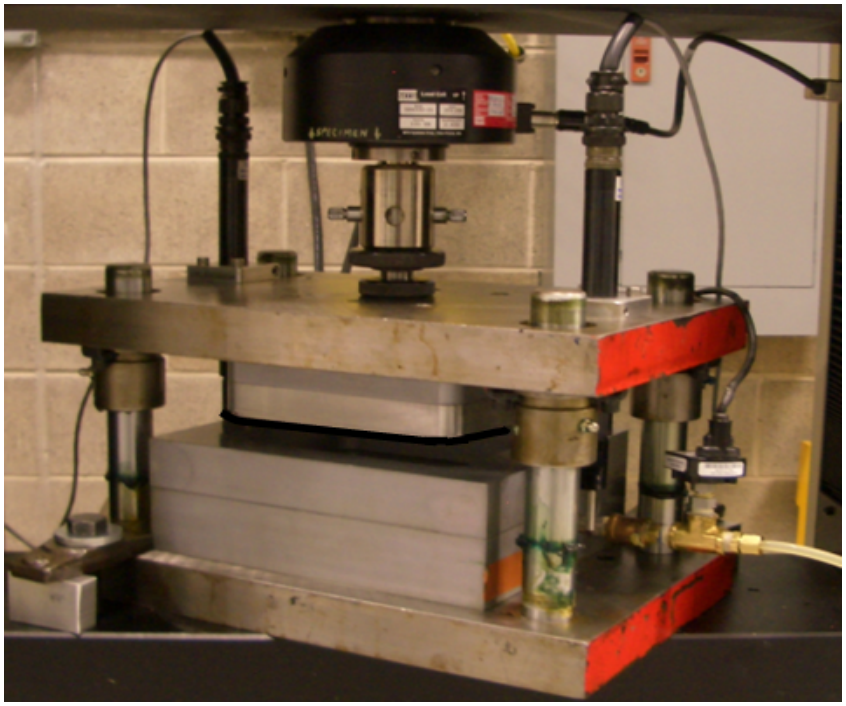

Figure 5.2 In-plane Permeability Fixture.

The transverse, or through-thickness, *Szz*, fixture, shown in Figures 5.3 and 5.4, was designed with a test cavity to accommodate 5.08 cm x 5.08 cm preform specimens up to 3.20 cm thick. The concept was identical to that of the in-plane fixture except that the fluid was directed through the thickness of the specimen by rigid distribution plates mounted in the plunger and in the bottom of the cavity. The plates were machined with 0.50 cm diameter holes drilled at every 0.64 cm. A single linear voltage differential transducer (LVDT) was used to measure the thickness of the preform specimen. Two pressure transducers were located at the inlet and outside sides used to measure the pressure gradient in the transverse direction.

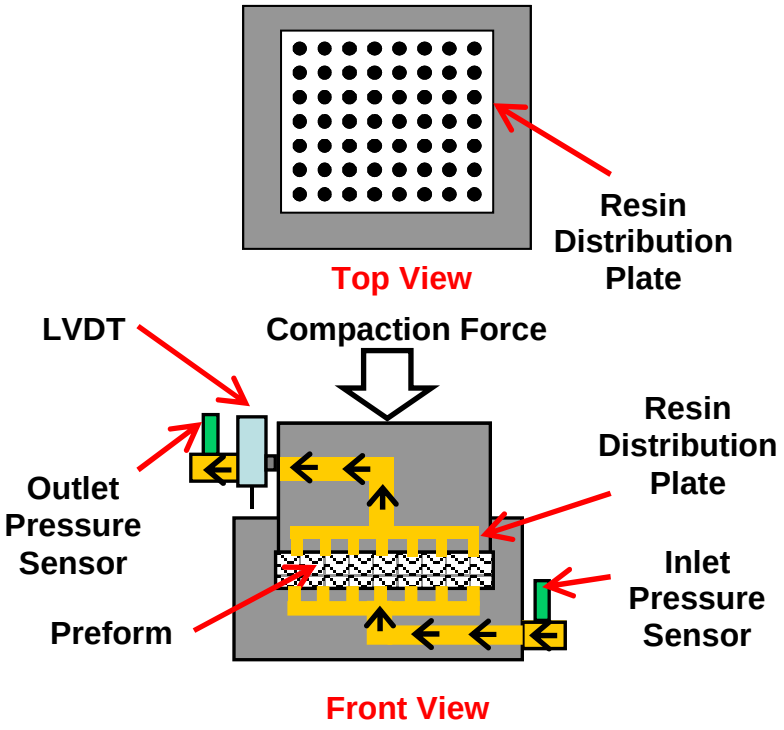

Figure 5.3 Schematic for Transverse Permeability Fixture.

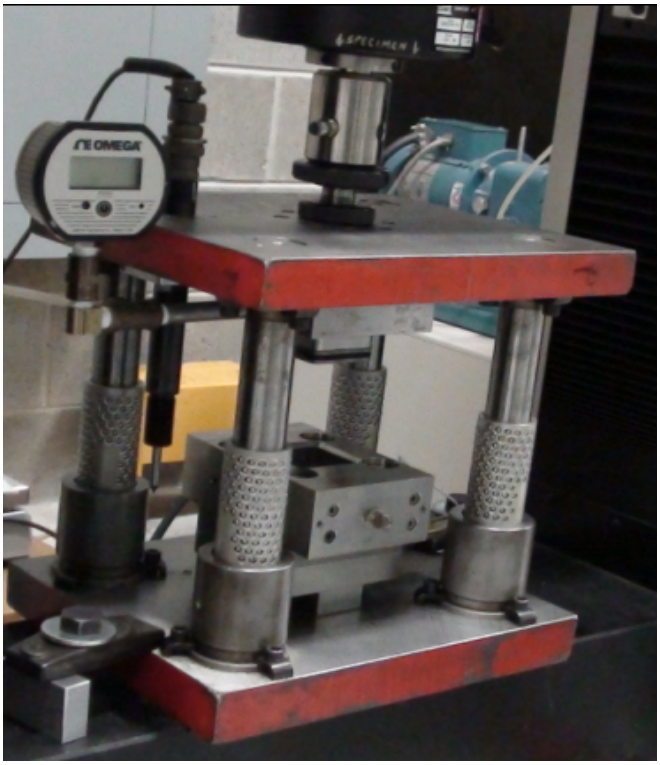

Figure 5.4 Transverse Permeability Fixture.

5.2.3 Test Procedures

In this section, the test procedure for both in-plane and transverse permeability measurements is explained in detail. At the beginning of each test, the load cell was calibrated using the MTS TestWorks software. The upper part of the fixture attached to the crosshead was lowered to the point where it touches the lower part of the fixture and some load reading was observed indicating contact. The LVDT and crosshead displacement readings were zeroed at this point. After this step, the crosshead was raised and an O-ring was inserted into the piston located in upper part of the fixture (Figures 5.2 and 5.4). For the in-plane permeability fixture, O-rings with a square cross section with sides of 3.3 mm and 540 mm long were used. For the transverse permeability fixture, O-rings with a circular cross section with a diameter of 3.87 mm and 158 mm long were used. O-rings were made by cutting and gluing the two ends of the rubber O-ring material and a new one was made for each test. The preform specimens were placed inside the cavity of the lower part of the fixture and the mold was closed by slowly lowering the crosshead to make sure that the O-ring was not sheared when the piston enters the cavity. Once the crosshead was lowered to the desired starting thickness or volume fraction level, a Parker Zenith® Precision Gear Metering Pump as shown in Figure 5.5 was used to inject the testing fluid into the fixture at a constant flow rate.

SAE 40 motor was used as the testing fluid in this study. The oil has viscosity of 0.24 Pa.s and a density of 709 g/cc. The flow rates through the preform samples were measured using a Mettler-Toledo® balance (model SB16001) and a stop watch.

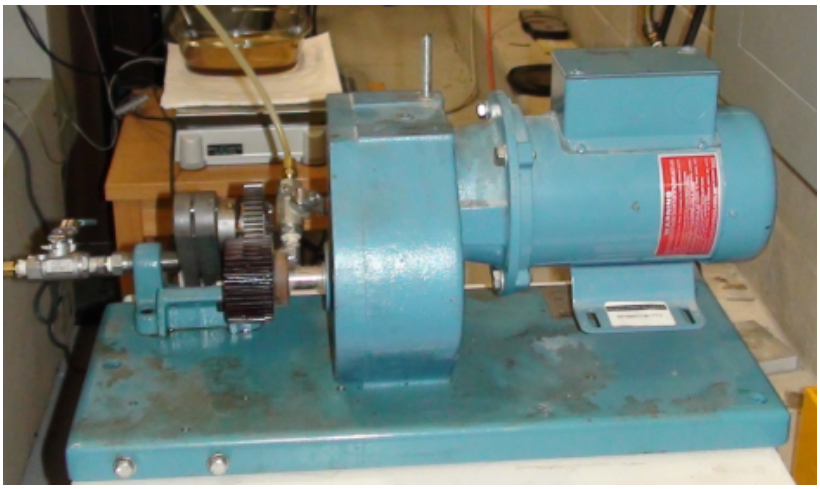

Figure 5.5 Parker Zenith® Precision Gear Metering Pump.

Once steady-state flow conditions were reached, the inlet and outlet pressures across the preform specimens were measured. At each fiber volume fraction, the difference between inlet and outlet pressures over a range of different flow rates was measured and the data was used to construct a curve of volumetric flow rate versus the pressure drop. A linear relationship between volumetric flow rate and pressure drop at a specified volume fraction was obtained and ensured that test was valid.

Measuring the slope of the volumetric flow rate versus pressure curve gives the average permeability for the preform at the specified fiber volume fraction. A sample plot is shown in Figure 5.6 for the S2 glass transverse permeability experiment. Looking at Figure 5.6, it can also be seen that as the fiber volume fraction increases the slope of the volumetric flow rate versus pressure curve decreases.

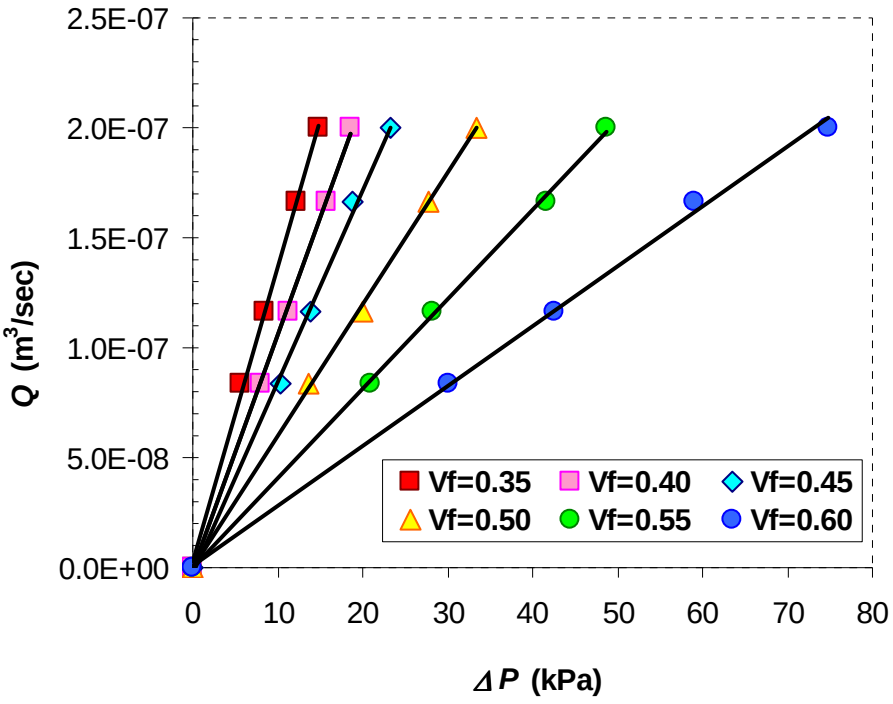

Figure 5.6 Change volumetric flow rate vs. pressure drop shown at four different volume fractions during S2 glass transverse permeability characterization.

5.3 Data Analysis

During the experiments the fluid inlet and outlet pressures, fluid flow rate and preform thickness were measured. The fiber volume fraction, V_f was calculated as follows:

$$V_f = \frac{FAW}{t * \rho_F} \tag{5.3}$$

where, FAW is the fiber areal weight of the preform, t is thickness, and ρ_F is the fiber density. Permeability S (m^2) was calculated at each compaction or thickness level from the one-dimensional form of Darcy's Law:

$$S = \frac{q\eta L}{\Delta P} \tag{5.4}$$

where, q is the superficial velocity (m/s), η is the viscosity of the fluid, $\Delta \boldsymbol{P}$ is the measured pressure difference and L is the length of the preform specimen in the direction of flow.

The superficial or filter velocity, q (m/s), was calculated as:

$$q = \frac{M}{\rho_R A} = \frac{Q}{A} \tag{5.5}$$

where, ρ_R is the density of the fluid (kg/m^3), M is the mass flow rate (kg/s) and A is the cross-sectional area of the preform normal to the flow direction (m^2) and Q is the volumetric flow rate (m^3/s).

Substituting Equation (5.5) $q = \frac{Q}{A}$ in Equation (5.4): $\Longrightarrow S = \eta\left(\frac{Q}{A}\right)\frac{L}{\Delta P}$ (5.6)

Rewriting Equation (5.6): $S = \eta\left(\frac{Q}{\Delta P}\right)\frac{L}{A} \quad \Longrightarrow \quad S = \eta\, m\frac{L}{A}$ (5.7)

where, $m = \frac{Q}{\Delta P}$ is the slope of the Q (m^3/s) vs. ΔP (Pa) curve.

Measuring the slope m of the volumetric flow rate versus pressure drop curve (as shown in the sample plot of Figure 5.6) gives the average permeability for the preform at the specified fiber volume fraction. Calculation of the permeability using the slope m is shown in Equations 5.6 and 5.7. L, the length of the preform specimen in the direction of flow was equal to the length of the mold and equal to the total preform thickness for the in-plane and transverse permeability measurement tests respectively. In addition, for the in-plane measurements, x was the warp direction and y was the fill direction.

For each preform specimen tested, a curve of permeability S versus fiber volume fraction V_f was constructed. The data was fit to an exponential equation as shown in Equation 5.8.

$$S = d\, e^{mVf} \tag{5.8}$$

where, *d* and *m* are constants.

5.4 Calculation of Transverse Permeability (*Szz*) using Hybrid Preforms:

The transverse permeability of highly porous preforms such as the resin distribution mediums used in the VARTM process can be hard to measure using the current permeability measurement setups. Since these materials were purposefully chosen with a substantially high transverse permeability to facilitate the through thickness resin flow, it can be hard to precisely measure the very minimal pressure gradient across them, which is needed in the permeability calculations. The permeability of a preform that cannot be directly measured can be calculated using permeability measurement data obtained from hybrid preform tests. In these hybrid preform configurations, the preform with high permeability was placed between two preforms with known permeabilities. A sample hybrid preform with two layers of glass fabric and a layer of distribution medium in between them is shown in the Figure 5.7.

In hybrid preform tests, the hybrid preform was compressed to a known total thickness. The thickness of the middle layer with unknown permeability was assumed to have the same thickness when measured at the load free condition. Subtracting this value from the overall total thickness gave the total thickness for the two fabric layers at the top and bottom. Since these fabric layers were of the same type, such as glass or carbon fabrics, it was assumed that each layer has the same compacted thickness and thus the same volume fraction. Using the

mathematical models fit to the permeability data of the glass or carbon fabrics, the corresponding permeability values of these fabrics at the specified volume fractions were calculated.

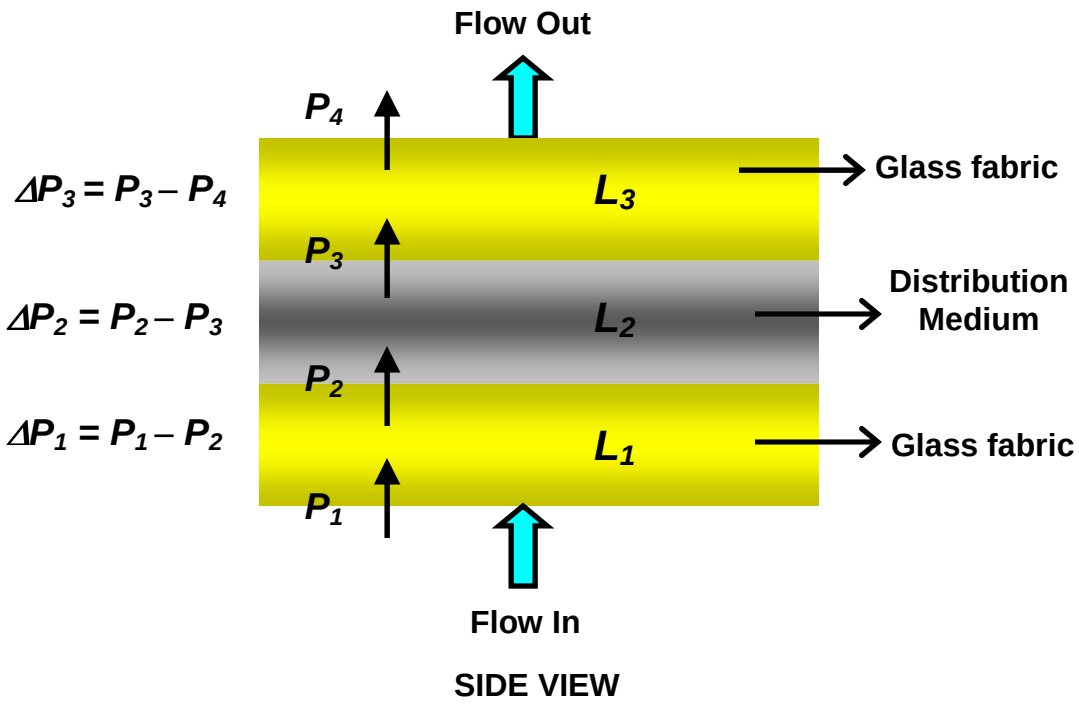

Figure 5.7 Sample hybrid preform with glass fabric layers and distribution medium.

From Figure 5.7, it can be noted that $\Delta P_3 = \Delta P_1$ since the glass (or carbon) fabric layers were assumed to have the same thickness $L_1 = L_3$ and same permeability at the specified volume fraction; $S_1 = S_3$. Thus, rewriting the one dimensional Darcy's Law as given by Equation 5.6 for the individual layers:

For Carbon/Glass Fabric Layer 1 (bottom layer): $S_1 = \eta \frac{Q}{A} \frac{L_1}{(P_1 - P_2)}$ (5.9)

For Carbon/Glass Fabric Layer 2 (top layer): $S_3 = \eta \frac{Q}{A} \frac{L_3}{(P_3 - P_4)}$ (5.10)

For the middle layer (screen distribution medium): $S_2 = \eta \frac{Q}{A} \frac{L_2}{(P_2 - P_3)}$ (5.11)

During the hybrid preform permeability tests, the inlet and outlet pressures; P_1 and P_4 and the flow rate Q were measured. The total thickness of the hybrid preform ($L_{total} = L_1 + L_2 + L_3$) was recorded during the test and the thickness of the middle layer (L_2) with unknown permeability was measured before the test. Thus, $L_1 = L_3 = (L_{total} - L_2)/2$.

In the set of Equations 5.9 to 5.11 above, the thickness values L_1, L_2 and L_3, the cross sectional area A, the viscosity of the fluid η and the pressures P_1 and P_4 are all known and the only unknowns are P_2 and P_3. Once Equation 5.9 and 5.10 are solved for the variables P_2 and P_3 in terms of the known variables, they can be substituted in Equation 5.11 to solve for the unknown permeability S_2 as follows:

$$S_2 = \eta \frac{Q}{A} \frac{L_2}{\left[P_1 - P_4 - \eta \frac{Q}{A} \left(\frac{L_1}{S_1} + \frac{L_3}{S_3} \right) \right]} \tag{5.12}$$

It was also possible to calculate an average permeability for S_2 by constructing a plot of volumetric flow rate versus pressure drop curve and measuring the slope of that curve as explained in section 5.3. For this purpose, P_2 and P_3 values need to be individually calculated from Equations 5.9 and 5.10 for multiple flow rates so that the pressure drop at each corresponding flow rate can be calculated.

5.5 Results

5.5.1 S2-Glass Fabric

Permeability characterization tests for S2 glass were performed in all three principal directions. In-plane permeability (*Sxx* and *Syy*) and transverse permeability (*Szz*) test results are shown in Figures 5.8 and 5.9, respectively. Three sets of tests were done for each principal direction (in-plane and transverse) and the exponential equation (Equation 5.9) was fit to the cumulative data.

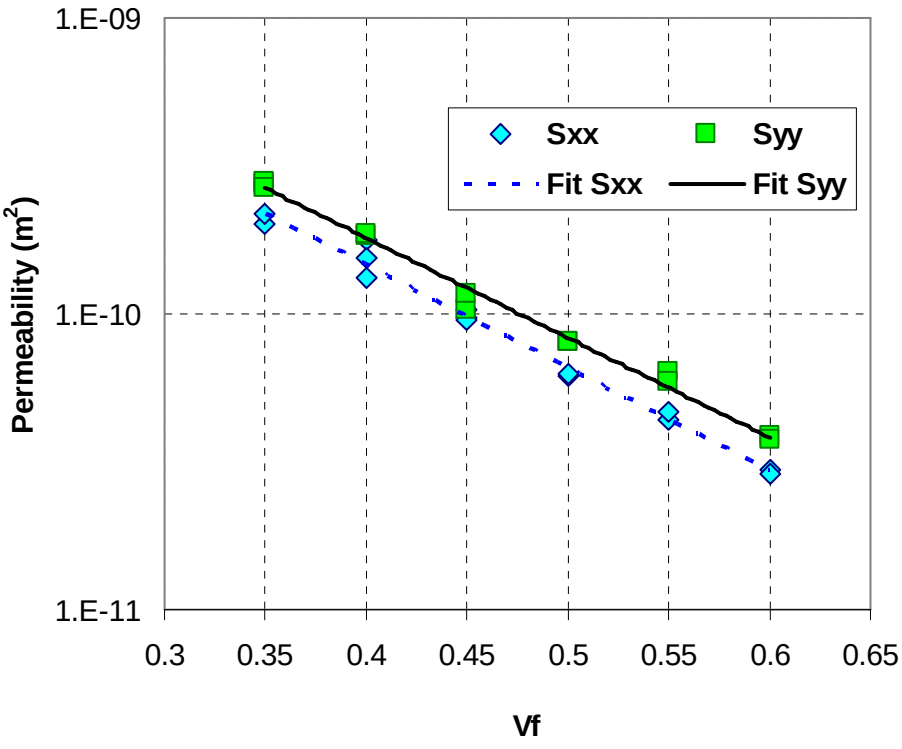

Figure 5.8 In-Plane Permeability (*Sxx* and *Syy*) test results for S2 glass preform.

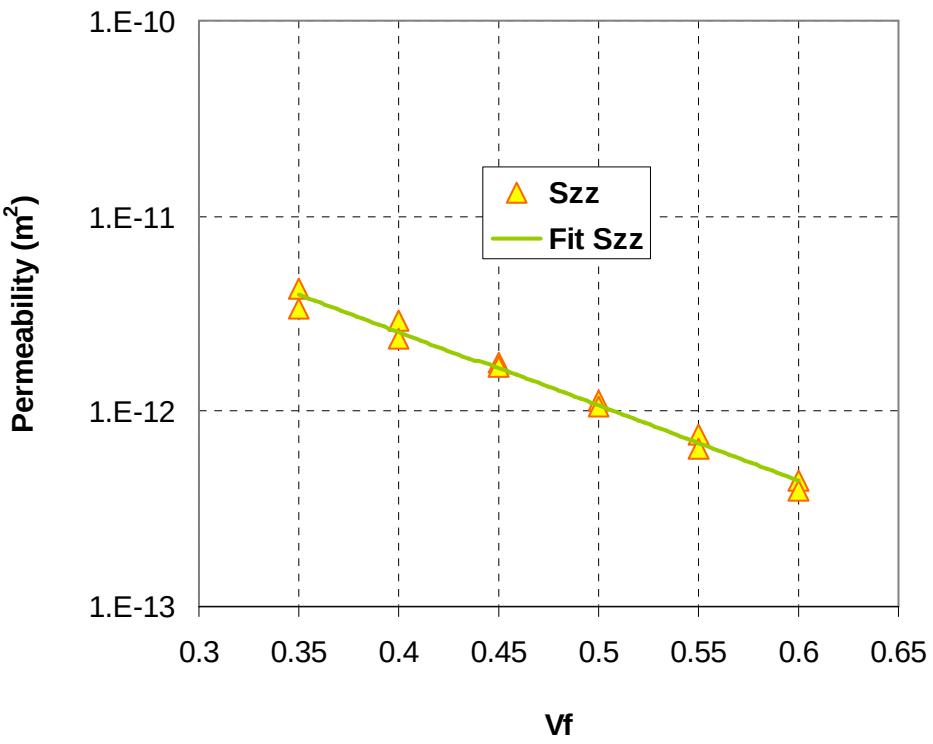

Figure 5.9 Transverse Permeability (*Szz*) test results for S2 glass preform.

The fit constants are given in Table 5.1. It is seen that the transverse permeability (*Szz*) values for the S2 glass preform was about one order of magnitude less when compared to the in-plane permeability (*Sxx* and S_{yy}) values.

Table 5.1 Constants of the exponential fit equation, $S = d\,e^{mVf}$ for S2 Glass in all three directions.

Sxx		***Syy***		***Szz***	
d	***m***	***d***	***m***	***d***	***m***
3.58e-9	-8.00	4.03e-9	-7.77	8.57e-11	-8.78

5.5.2 Acetate Films with Flow Pathways

Acetate films with flow pathways were part of the hybrid preforms and their transverse permeability should also be characterized since this information is required as an input parameter for the simulation model as explained in Chapter 3. Acetate films with four different pathway configurations were tested. These were pathways with 0.41mm, 0.83 mm and 1.59 mm diameters with 2.54 cm spacing and pathways with 0.41mm diameter with 1.27 cm spacing. Figure 5.10 shows the transverse permeability vs. porosity for acetate films with these four pathway configurations. A summary of transverse permeability (*Szz*) test results for acetate films with flow pathways is given in Table 5.2.

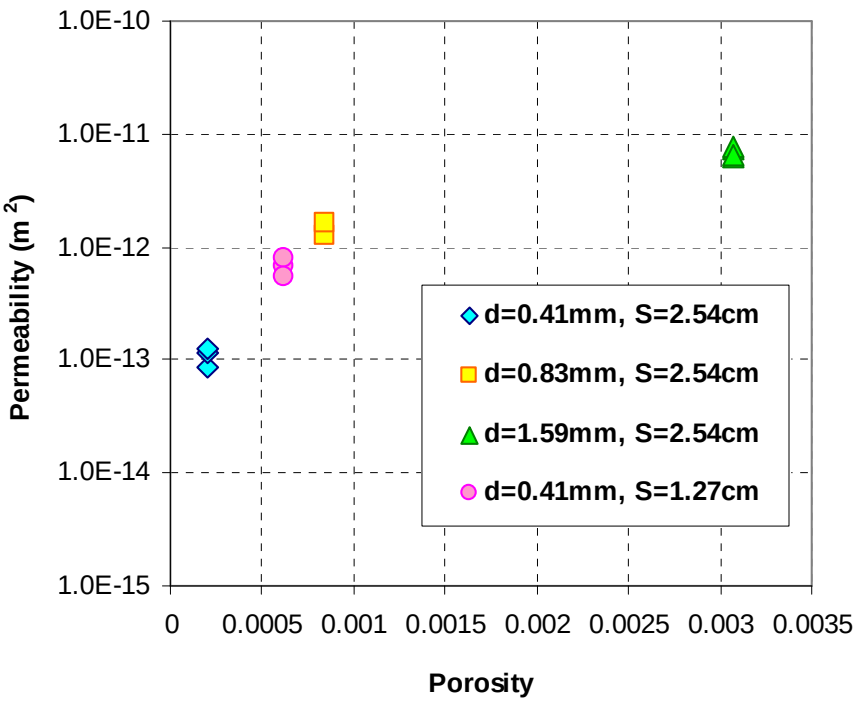

Figure 5.10 Transverse permeability (*Szz*) vs. porosity for acetate films with flow pathways.

Table 5.2 Summary of transverse permeability (*Szz*) tests for acetate films with flow pathways.

Pathway Diameter and Spacing	**Porosity**	**Permeability (m^2)**
d = 0.41 mm	2.05e-04	8.42e-14 (test 1)
S =2.54 cm		1.15e-13 (test 2)
		1.26e-13 (test 3)
		1.08e-13 (avg.)
d = 0.83 mm	8.39e-04	1.27e-12 (test 1)
S =2.54 cm		1.61e-12 (test 2)
		1.44e-12 (avg.)
d = 1.59 mm	3.08e-03	7.45e-12 (test 1) *
S =2.54 cm		6.38e-12 (test 2) *
		6.91e-12 (avg.)
d = 0.41 mm	6.14e-04	6.63e-13 (test 1)
S =1.27 cm		5.47e-13 (test 2)
		7.81e-13 (test 3)
		6.64e-13 (avg.)

While performing the experiments, it was important to place the acetate films such that the flow pathways were in alignment with the holes of the resin distribution plate inside the transverse permeability fixture. Otherwise, the flow through the films will be either partially or completely blocked and the measurements will be inaccurate.

Due to the high porosity of acetate films with 1.59mm flow pathway diameter, there was very minimal pressure drop across the specimens. Thus, hybrid preform tests consisting of alternating layers of S2 glass and acetate films with 1.59 mm pathway diameter were performed. The permeability values denoted with a (*) in Table 5.2 were not directly measured values. They

were calculated using the permeability calculation method for the hybrid preforms, as described in Section 5.4.

Looking at Figure 5.10 and Table 5.2, it is seen that the permeabilities of acetate films increase as their flow pathway size or porosity increases as expected. Acetate films with 0.41 mm pathway diameter and with 1.27cm spacing have a permeability closer to but still less than the permeability of the acetate films with 0.83 mm pathway diameter and with 2.54 cm spacing.

5.5.3 Distribution Medium

Figure 5.11 shows the in-plane permeability test results for the distribution media (DM). Due to the architecture of the distribution media, the permeabilities in x and y in-plane directions were equal to each other. The porosity of the distribution medium was very high and it was very hard to measure the pressure difference in the through thickness direction. Thus, the transverse permeability of the distribution media was calculated in a similar manner to the permeability calculation of the acetate films with 1.59 mm pathway diameter. Hybrid preform tests consisting of two layers of S2 glass and three layers of distribution media were performed.

The measured in-plane values are shown in Figure 5.11. Constants of the exponential fit equation for $Sxx=Syy$ values and the calculated average Szz value using the hybrid calculation method are shown in Table 5.3.

Table 5.3 Constants of the exponential fit equation, $S = d\, e^{mVf}$ for the distribution medium and the calculated average transverse permeability (*Szz*) value for the distribution media.

Sxx= Syy		***Szz* (m^2)**
d	***m***	1.53e-10
1.216e-7	-10.52	

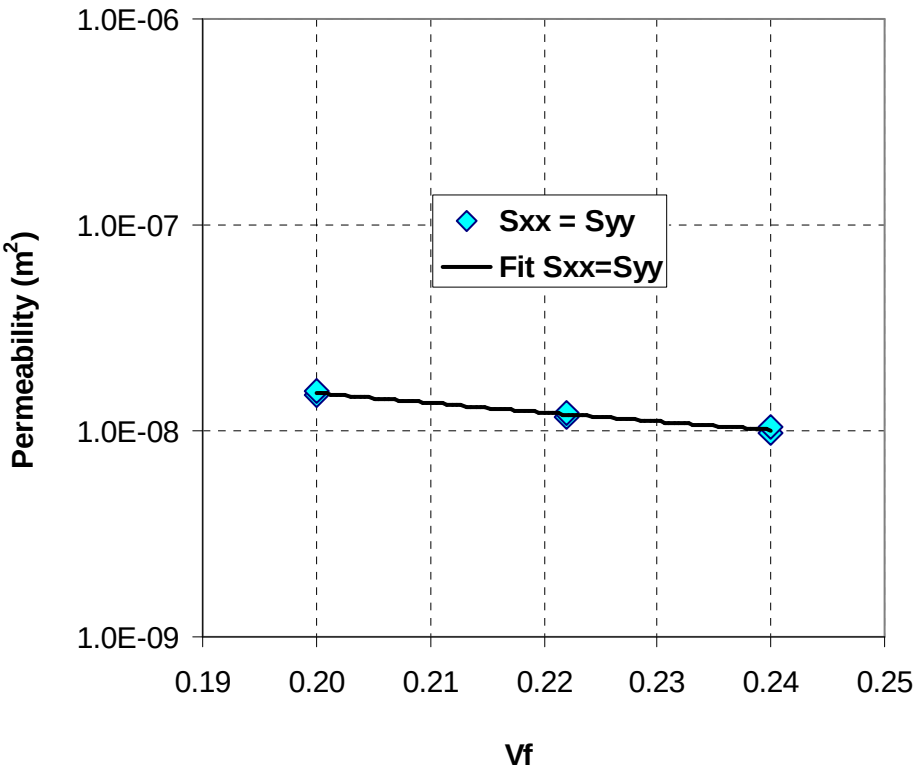

Figure 5.11 Measured in-plane permeability (*Sxx = Syy*) vs. volume fraction for three layers of distribution medium.

5.6 Summary

The second of two important characterization experiments required to construct an accurate model of the VARTM process is the preform permeability characterization. In this chapter, permeability characterization test procedures were discussed and the results of the permeability characterization tests were presented for the S2 glass fabric (in-plane and transverse directions), acetate films (transverse direction) with different diameter and spacing configurations and for the distribution media (DM) (in-plane and transverse directions).

For highly porous media e.g. distribution media (DM) where a minimal pressure drop occurs through the thickness of the preform, an analytical formulation was developed based on one dimensional Darcy's Law and hybrid permeability measurement tests. The transverse permeabilities of the DM and the acetate films with the 1.59 mm flow pathway diameter were calculated using this method. The assumption made in this method was that the middle layer with the unknown permeability has a constant thickness equal to the measured thickness at the load free condition. This assumption was reasonably accurate for the preforms with minimal deformation when compacted. For the outer layers, such as glass or carbon fabrics, it was assumed that each layer has the same compacted thickness and thus the same volume fraction.

The transverse permeability measurements of the S2 glass fabric agreed well with the measurements by Ouagne and Breard [68] made for E glass 5 harness satin weave fabrics and with the predictions of Gokce et al. [69] made for 5 x 4 woven E glass fabrics using a VARTM simulation model. The transverse and in-plane permeability measurements of the DM also agree

well with a previous study by Song [70] and the in-plane DM permeability measurements were in the same order of magnitude with the predictions made by Gokce et al. [69].

Chapter 6

SIMULATION MODEL FOR THE VARTM/CAPRI FML PROCESSES

6.1 The FLUENT Model

A three dimensional simulation model was developed using the computational fluid dynamics (CFD) software FLUENT to monitor the filling process in the VARTM/CAPRI FML processes. The resin flow was modeled as a two-phase fluid flow through the porous medium. A multiphase volume of fluid (VOF) model [71] was adopted to track the resin flow patterns. An Euler explicit time-dependent formulation was used for the solution of the VOF scheme. The model assumed the properties of the resin did not change during the infiltration process. Inertia and capillary effects, and surface tension were not considered due to low Reynolds number and dominant viscous forces [72].

6.1.1 Governing Equations

In the current model, a volume of fluid (VOF) model was adopted to monitor the free boundary at the interface between the two phases; air and resin. In a VOF model, the location of the interface between the two phases is monitored by the solution of the continuity equation for the volume fraction of air, ε_{air} [72] as shown below:

$$\frac{\partial \varepsilon_{air}}{\partial t} + q_i \frac{\partial \varepsilon_{air}}{\partial x_i} = 0 \tag{6.1}$$

where, q_i is the velocity component of resin in x_i direction and t is time.

In the current model, air was chosen as the second phase. In general, the phases can be defined in any order. However, if the initial volume fraction of a phase will be assigned a value of 1 in any portion of the domain, it is recommended that the phase be chosen as the secondary phase for computational reasons [73]. The initial volume fractions of the phases used in the liquid composite molding (LCM) models are typically set as follows. Volume fraction of air is set to 1 at t =0, meaning that no resin is present in the domain prior to the infiltration process. The relation between the two phases any time during the calculation is given by:

$$\varepsilon_{resin} = 1 - \varepsilon_{air} \tag{6.2}$$

where, ε_{resin} is the volume fraction of resin.

The momentum equation is solved for the entire domain [72]:

$$\frac{\partial}{\partial t}(\rho\, q_j) + \frac{\partial}{\partial x_i}(\rho\, q_i q_j) = -\frac{\partial P}{\partial x_j} + \frac{\partial P}{\partial x_i}\eta\left(\frac{\partial q_i}{\partial x_j} + \frac{\partial q_j}{\partial x_i}\right) - \sum_{i=1}^{3}\frac{\eta}{S_{ji}}q_i \tag{6.3}$$

where, $\sum_{i=1}^{3}\frac{\eta}{S_{ji}}q_i$ represents the viscous term and S_{ji} is the permeability tensor.

For each control volume, rule of mixtures relations apply for the density,

$$\rho = \varepsilon_{resin}\rho_{resin} + \varepsilon_{air}\rho_{air} \tag{6.4}$$

and for the viscosity,

$$\eta = \varepsilon_{resin}\eta_{resin} + \varepsilon_{air}\eta_{air} \tag{6.5}$$

where, ρ_{resin} and ρ_{air} are the densities, and η_{resin} and η_{air} are the dynamic viscosities of the resin and air, respectively.

6.1.2 Modeling of the Flow Pathways as Porous Strips

As noted before, during the VARTM/CAPRI FML processes, the flow is only in the through the thickness direction through the flow pathways that have been drilled into the acetate films. The pathways are equally spaced holes that cover the entire length and width of the acetate films. A large number of pathways exist in each layer and they typically have very small diameters compared to the planar dimensions of the preforms. In addition, the overall thicknesses of the preforms used in the FML structures are also typically much smaller compared to the planar dimensions. This brings a potential problem of divergence in the flow solution due to the high aspect ratios of the mesh cells and also the computational burden of using an extremely fine mesh around the small diameter pathways. Hence, in order to generate a more stable and simplified model, each row of pathways along the length of the acetate films was modeled as a *porous strip* of width equal to the diameter of the pathways and with an equivalent permeability. The porous strips are shown in Figure 6.1.

The porous strips were modeled using the "*porous jump*" boundary condition in FLUENT. Porous jump conditions are used to model thin membranes with known velocity (pressure-drop) characteristics [74]. It is essentially a one-dimensional simplification of the porous medium model available for cell zones. This simpler model is more robust and yields better convergence [74].

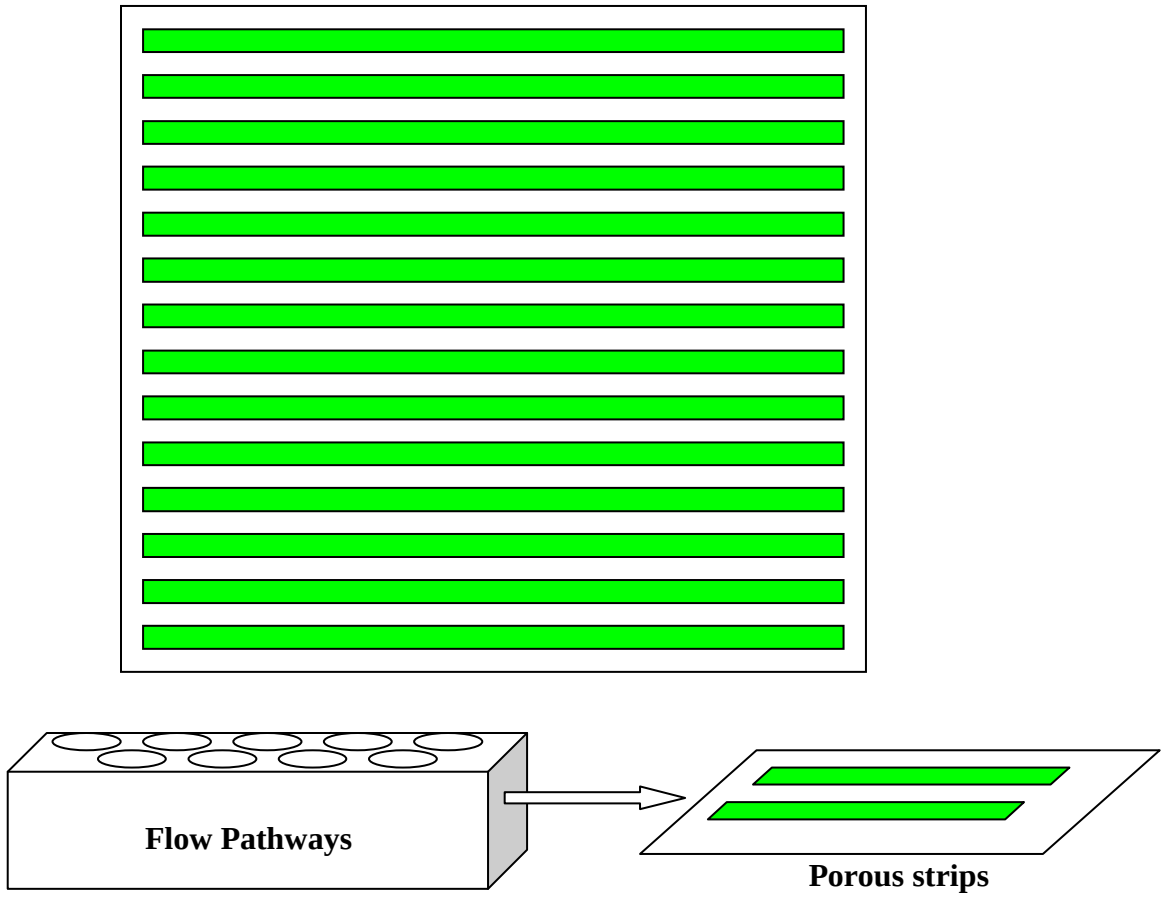

Figure 6.1 Flow pathways modeled as porous strips.

Although the porous strips were created as two dimensional geometries, a thickness was assigned to them per the porous jump formulation in FLUENT. This thickness is equal to the finite thickness of the plates that contain the flow pathways over which the pressure change is defined as a combination of Darcy's Law and an additional inertial loss term as given by [74]:

$$\Delta P = -\left(\frac{\eta}{S} q + C\frac{1}{2}\rho\, q^2\right) l \tag{6.6}$$

where, ΔP is the pressure change, η is the viscosity of the fluid, S is the permeability of the permeable strips, C is the inertial resistance factor, l is the thickness of the acetate film and q is

the velocity normal to the porous face. The inertial resistance C can be neglected for laminar flow and Equation 6.6 reduces to one dimensional Darcy's Law.

6.1.3 Creating the Model and Boundary Conditions

The 3D geometry of the model for the hybrid preform structure was generated using GAMBIT. GAMBIT is a preprocessor program for FLUENT used to build and mesh the models. In the current model, glass fabric preforms and distribution medium were modeled as three dimensional porous volumes and the flow pathways were modeled as a series of parallel porous strips. Each layer of reinforcement was modeled as a 3D volume to monitor the infiltration in each layer whereas multiple layers of distribution medium were modeled as a single 3D volume. Porous strips representing the flow pathways in the acetate films were modeled as two dimensional shared surfaces between two consecutive layers of the reinforcement or between one layer of reinforcement and the distribution medium. In this way, each layer of reinforcement, except the one at the very bottom, had porous strips both at the top and bottom surfaces. The distribution medium had porous strips only at the bottom surface, which were also shared by the top layer of reinforcement. Fourteen parallel porous strips were used to represent the flow pathways in each acetate film for pathways with the 2.54 cm spacing. Twenty-eight parallel porous strips were used to represent the flow pathways in each acetate film for pathways with the 1.27 cm spacing. In order to include the effect of race-tracking on two edges of the mold, two channels, each 4 mm wide, were added to the two edges of the preform.

A three dimensional mesh of the overall geometry is shown in Figure 6.2. The distribution medium (pink) is seen on the top and the fabric preform (green) is seen at the bottom. The injection port is shown to the right. The mesh shown here is composed of 41180 three dimensional hexahedral cells and has 76528 nodes. The geometries of the distribution medium and each layer of the reinforcement were meshed separately. A major planar dimension of 6 mm was assigned to the mesh cells and they were adjusted by GAMBIT to form either square or rectangular elements depending on the geometry. One element was assigned per thickness of every individual layer. Two finer meshes were also used to see the effect of the mesh size on the model results. This will be discussed in Section 6.2.1.

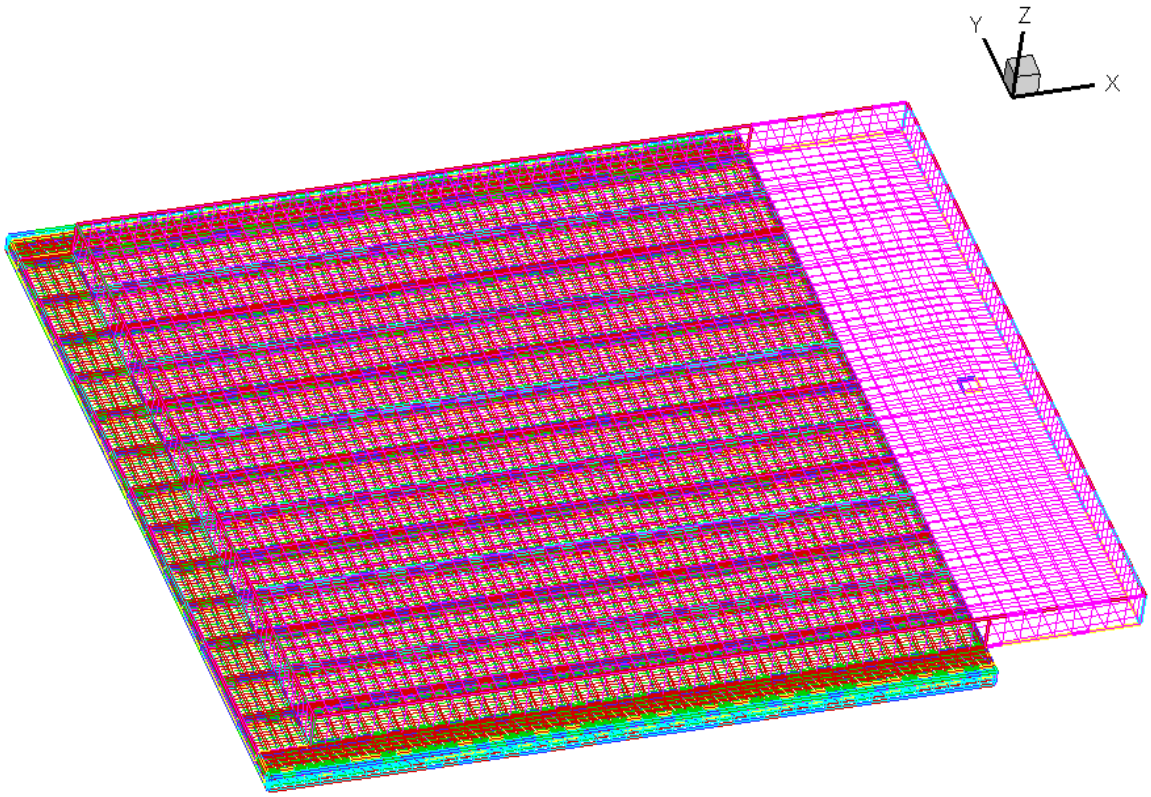

Figure 6.2 Three dimensional mesh created in GAMBIT.

After creating the geometry and meshing all the layers, the boundary conditions and continuum types were defined. A schematic diagram of the preform with the boundary conditions is shown in Figure 6.3. The resin injection port was modeled as a square pressure inlet, which has the same cross sectional area as the circular injection port used in the tests. This was done to preserve the uniformity of the mesh composed of hexahedral cells and to avoid long computation times. A “pressure inlet” boundary condition was defined at the injection port. All the top and side surfaces of the distribution medium were defined as “wall”, except for the left end face which was defined as “pressure outlet” to allow flow of resin into the hybrid preform as shown in Figure 6.3.

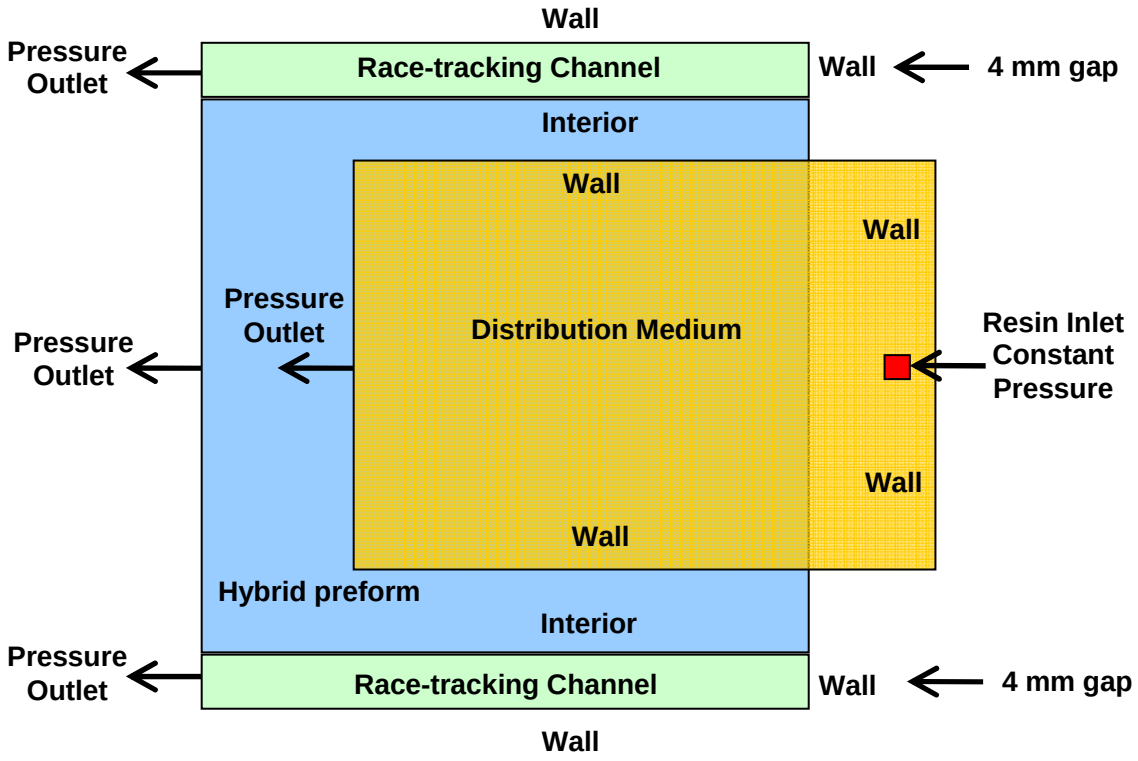

Figure 6.3 Boundary conditions used in the FLUENT model.

“Pressure outlet” boundary conditions were specified at the left-end (resin outlet side) of the race-tracking channels and the preform. The side faces of the glass preform, modeled as race-tracking channels, were defined as an “interior boundary” to allow the flow of resin into these channels.

After the boundary conditions were assigned in GAMBIT, the three dimensional mesh was exported to FLUENT for further processing and calculation. In FLUENT, pressure inlet and outlet conditions, operating conditions, material properties such as density, viscosity, porosity and permeability, the initial conditions of the phases and porous jump conditions were defined.

The pressure at the injection port was set to 1 atm (101.3 kPa) for the VARTM process. The pressure at the injection port was set to 0.5 atm (50.66 kPa) for the CAPRI process. The pressures at the pressure outlet boundary conditions were set to zero for both processes.

One limitation of the VOF model is that it does not allow for regions where no fluid of any type is present [71]. In the VARTM and CAPRI tests, since the preform is held either at full or partial vacuum prior to resin infiltration, regions with no or a minimal amount of air do exist. Thus, the operating pressure was set to zero. Table 6.1 shows the material properties used in the model for the two phases; the resin (motor oil) and air.

Table 6.1 Material properties for the two phases; the resin (motor oil) and air.

Material	Density (kg/m^3)	Viscosity (Pa.s)
Air	1.225	$1.789e^{-5}$
Motor Oil	709	0.24

The initial porosity values used for the glass fabric and the distribution medium were 0.52 and 0.76, respectively. These values were calculated based on the mathematical models fit to the compaction data as described in Chapter 4 and represent the volume fractions when the glass fabric and the distribution medium were fully dry compacted at 1 atm atmospheric pressure. The permeability values in the three principal directions at the specified initial volume fractions were calculated based on the mathematical models fit to the permeability data for the glass fabric and the distribution medium as described in Chapter 5. FLUENT uses viscous resistance ($1/m^2$) which is the reciprocal of the permeability (m^2).

The inputs for the "porous jump" boundary condition (Equation 6.6) were the thickness and the transverse permeability of the porous strips. The thickness value for the acetate films was measured as 0.382 mm per layer and the transverse permeability values depending on the pathway diameters and spacings were based on the average transverse permeability measurements as given in Table 5.2 of Chapter 5.

6.2 VARTM Simulation Results and Comparisons with the Flow Visualization Tests

In this section, the FLUENT model results are compared with the flow visualization test results that were previously discussed in Chapter 3. The flow patterns at the top and bottom surfaces of the hybrid preform are compared with the FLUENT simulation model results for the VARTM and CAPRI processes with different pathway hole diameter and spacing configurations.

Table 6.2 shows the permeability values corresponding to the initial volume fractions of the glass fabric (V_f =0.48) and the distribution medium (V_f =0.24) at 1 atm. (101.3 kPa) pressure. These values were calculated using the mathematical models as described in Chapter 5 and thus, they were based on the measured permeability data. The model results presented in this section use the measured permeability values given in Table 6.2.

Table 6.2 Permeability values in the three principal directions for the glass fabric and the distribution medium.

Material	Sxx (m^2)	Syy (m^2)	Szz (m^2)
Glass Fabric	$7.75e^{-11}$	$9.7e^{-11}$	$1.26e^{-12}$
Distribution Medium	$1.0e^{-8}$	$1.0e^{-8}$	$1.53e^{-10}$

6.2.1 Sample Case

In this sub-section, the results of the VARTM process simulations are presented for the sample case of flow pathways with 0.83 mm diameter and 2.54 cm spacing. The contour plots showing the simulation results were created by using the post-processor data imaging software TECPLOT.

For the top surface of the distribution medium, the comparisons between the experiments and the simulations were made by denoting the times required for the flow front to reach the specified flow front positions. For the bottom surface of the hybrid preform, the comparisons between the experiments and the simulations were made by plotting the flow front positions and patterns at the same time intervals. The color scale bar below the simulation results represents the volume fraction of the resin (phase 1). The color red represents a resin volume fraction of 1, i.e. fully saturated. The color blue represents a resin volume fraction of 0, i.e. completely dry.

In Figures 6.4 and 6.5, the flow patterns on the top and bottom surfaces of the hybrid preform are compared with the FLUENT simulation model results. The flow patterns and infiltration times on the top surface of the distribution medium were captured well; however, the predicted infiltration times were longer than measured. The total infiltration time of the distribution medium was measured as 30 seconds as opposed to the simulated infiltration time of about 70 seconds.

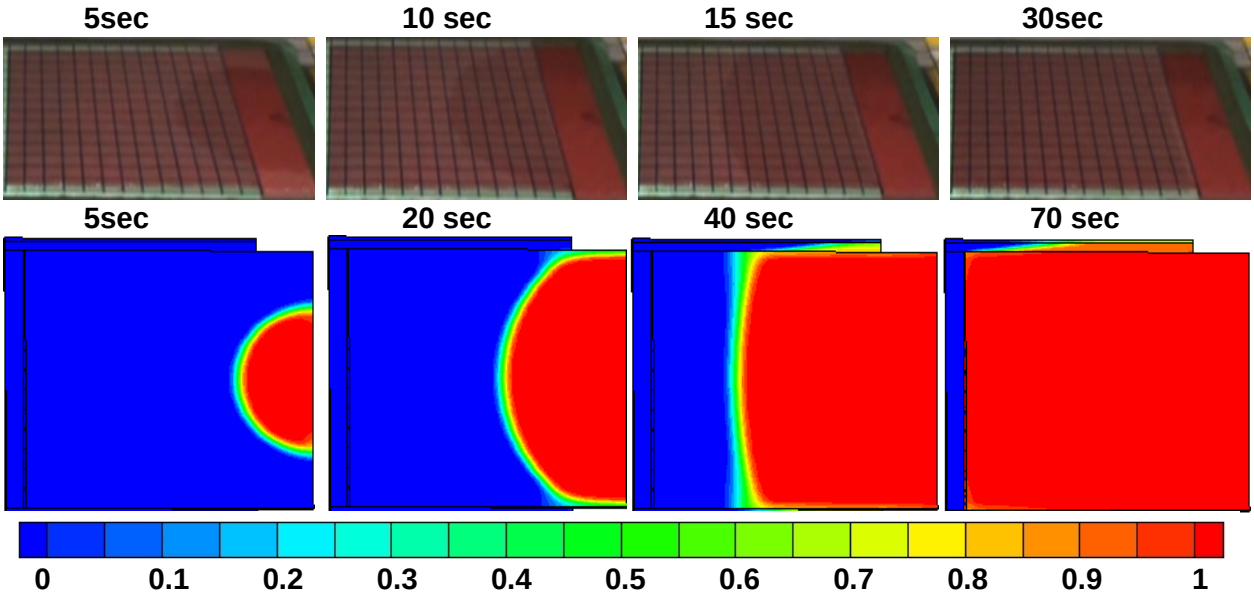

Figure 6.4 Flow patterns on the top surface of the distribution medium. Comparison between the flow patterns observed during the flow visualization test (top) and predicted by the simulation model (bottom) for flow pathways with d=0.83 mm and S=2.54 cm.

During the infiltration of the preform in the transverse direction (Figure 6.5), the dark circles that appeared at the bottom surface were simulated by the porous strips as they turned red. As the circles got larger and merged with the adjacent pathways to form a strip-like pattern, the simulated porous strips seen in red also got thicker. However, the shape of the bulk flow front was not captured well. The total wet-out time for the bottom surface of the hybrid preform was measured as 8.5 minutes. The simulation model did not predict a total wet-out of the preform at the same filling time. The simulation results were based on the measured permeability values for the porous strips.

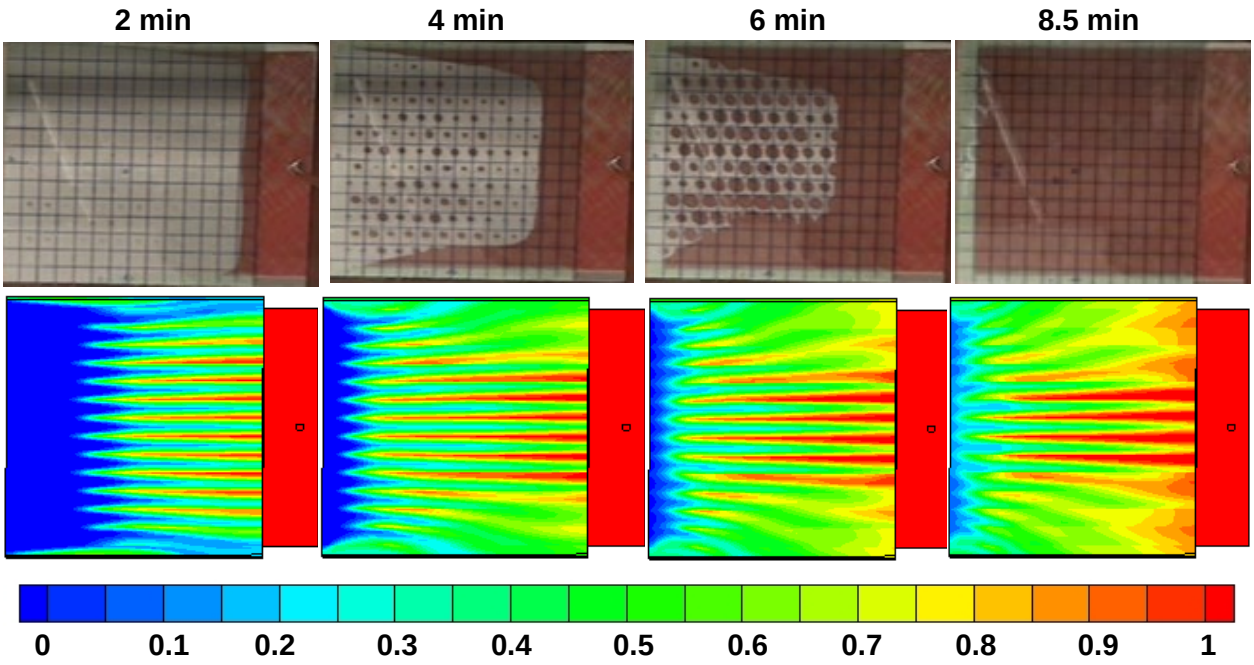

Figure 6.5 Flow patterns on the bottom surface of the hybrid preform. Comparison between the flow patterns observed during the flow visualization test (top) and predicted by the simulation model (bottom) for flow pathways with d=0.83 mm and S=2.54 cm.

Using the current model, the infiltration of individual layers inside the hybrid preform can also be simulated. Figure 6.6 shows the infiltration of the four individual layers of glass fabrics. The simulated flow patterns on the bottom surface of each layer are shown at different time frames. Starting with the layer closest to the top surface of the hybrid preform (top layer), then the middle two layers and the layer closest to the bottom surface of the hybrid preform (bottom layer) are shown form left to right (horizontally) in the figure. The predicted flow patterns for each layer as time evolves are shown from top to bottom (vertically) in the figure. The simulated case shown here was for hybrid preforms with flow pathways of 0.41 mm diameter and 2.54 cm spacing in the VARTM process.

In Figure 6.6, it is seen that the top layers of the preform closer to the distribution medium had a higher amount of infiltration. This is an expected result, since the transverse flow inside the preform took place from top to bottom. The higher amount of infiltration can be observed closer to the sides of the preform and around the porous strips. Layers closer to the top surface of the hybrid preform also indicated a faster progression of the resin when compared with the flow patterns predicted on the layers closer to the bottom surface of the hybrid preform.

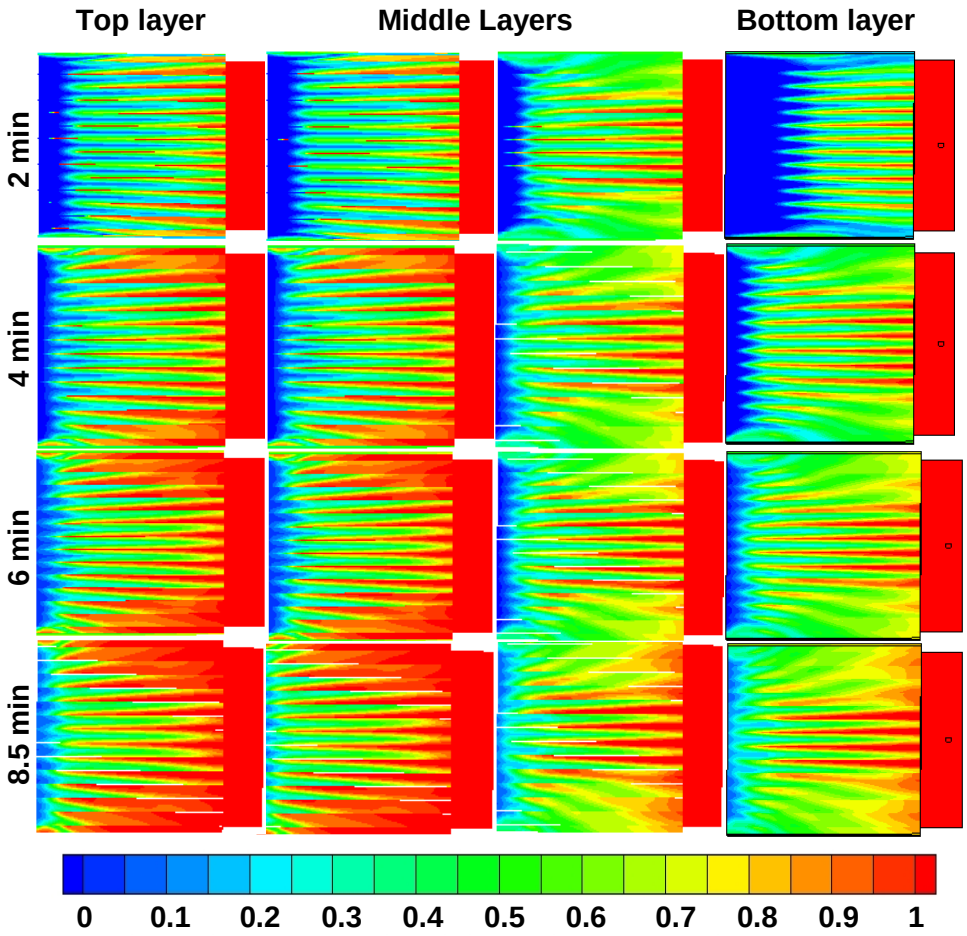

Figure 6.6 The flow patterns predicted by the simulation model on the individual layers. The bottom surfaces of the glass fabrics are shown as time evolves from top to bottom (vertically). Shown for hybrid preform with flow pathways of d=0.83 mm and S=2.54 cm.

Figure 6.7 shows a one-on-one comparison between the flow patterns predicted on the layer closest to the top surface of the hybrid preform (top layer) and the layer closest to the bottom surface of the hybrid preform (bottom layer). The flow patterns observed during the flow visualization test of this case is also shown. Looking particularly closer to the sides of the preform, it is seen that the flow patterns on the top layer show a better match with the flow patterns of the flow visualization test.

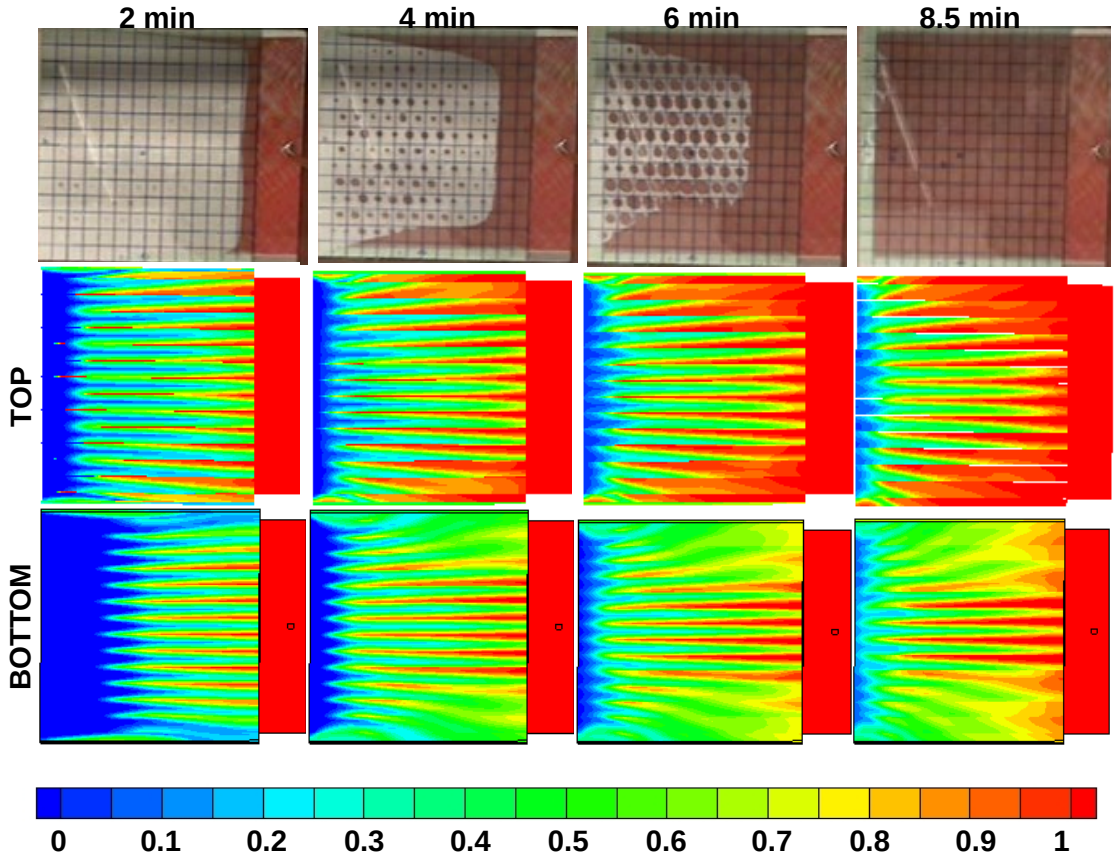

Figure 6.7 Flow patterns predicted by the simulation model on the top and bottom layers of the hybrid preform. Shown for flow pathways of d=0.83 mm and S=2.54 cm.

Using the user defined function (UDF) module in FLUENT, a compaction model was integrated to the existing simulation model in order to take thickness and permeability changes into account during the VARTM/CAPRI FML processes and thus in order to more accurately model these processes.

A UDF is a programmed function that can be dynamically loaded with the FLUENT solver to enhance the standard features of the code [75]. UDFs can be used to define custom boundary conditions, model properties, and source terms for the chosen flow regime. UDFs are written in C programming language and must be defined using `DEFINE` macros supplied by Fluent Inc. [75]. These macros are utilized to access FLUENT solver data and perform specific tasks.

The UDF for the compaction model was based on the compaction and permeability measurements presented in Chapters 4 and 5. The strain was calculated using the mathematical model proposed in Section 4.4.2 and given by Equation 6.7 below. The strain ε_i was updated at every time step *i* based on the fabric pressure or the pressure supported by preform $(P_f)_i$ and the model constants: *a, b* and *c*. Here, *i* represents the number of time steps in the transient solution.

$$\varepsilon_i = a + b\left[\frac{(P_f)_i}{c + (P_f)_i}\right] \tag{6.7}$$

The modeling of the compaction process during the VARTM process was discussed in Section 4.1. Depending on the volume fraction of the resin, two sets of model constants *a, b* and *c* were used; one for dry loading and one for wet unloading. These constants were given in Table 4.1.

The UDF function was programmed to use the model constants for *wet unloading* when the volume fraction of resin was equal and greater than 0.95 (indicating full saturation) and use the model constants for *dry loading* otherwise.

The fabric pressure $(P_f)_i$ was updated based on the resin pressure $(P_{resin})_i$ that was calculated using the VOF solution method. According to the transverse equilibrium equation in the VARTM process as described in Section 4.1, the summation of the resin pressure and the fabric pressure must be equal to the atmospheric pressure of 101.32 kPa. At every iteration, the fabric pressure $(P_f)_i$ was updated based on the resin pressure $(P_{resin})_i$ that was calculated using the VOF model by FLUENT as follows.

$$(P_f)_i = P_{atmospheric} - (P_{resin})_i \tag{6.8}$$

The fiber volume fraction $(V_f)_i$ was also updated based on the strain ε_i.

$$(V_f)_i = \frac{V_{fo}}{1-\varepsilon_i} \tag{6.9}$$

where V_{fo} is the initial fiber volume fraction.

The initial volume fractions used for the dry loading and wet unloading were 0.48 and 0.58, respectively at 101.32 kPa pressure based on the compaction data shown in Figures 4.17 and 4.18. Permeability of the glass fabric preform was calculated using the mathematical model proposed in Section 5.5.1. Permeability in three principal directions was updated based on the fiber volume fraction $(V_f)_i$ and the model constants *d* and *m* as given in Table 5.1.

$$S_i = d.\exp\left(m.(V_f)_i\right) \tag{6.10}$$

Viscous resistance was calculated by taking the reciprocal of permeability S_i. Finally, the thickness change Δt_i was calculated and updated at every time step based on the strain ε_i and the initial thickness t_o as follows:

$$\Delta t_i = \sum (\varepsilon_i * t_o) \tag{6.11}$$

In Figure 6.8, the flow patterns on the bottom surface of the hybrid preform predicted by the simulation models with and without the compaction model are shown in the middle and at the bottom of the figure, respectively. The flow patterns observed in the flow visualization test are shown at the top of the figure. The simulation was performed for the VARTM process and for hybrid preform with flow pathways of 0.83 mm diameter and 2.54 cm spacing.

It is observed that the simulation model with the compaction model improves the flow patterns by enabling a faster infiltration when compared with the flow patterns of the original model. The flow patterns predicted in the distribution medium on the top surfaces of the hybrid preform is not shown here since a noticeable difference was not observed when compared to the model without the compaction model. However, as the infiltration time increases a noticeable improvement is observed on the bottom surfaces as shown in Figure 6.8. The UDF program codes are given in Appendix C.

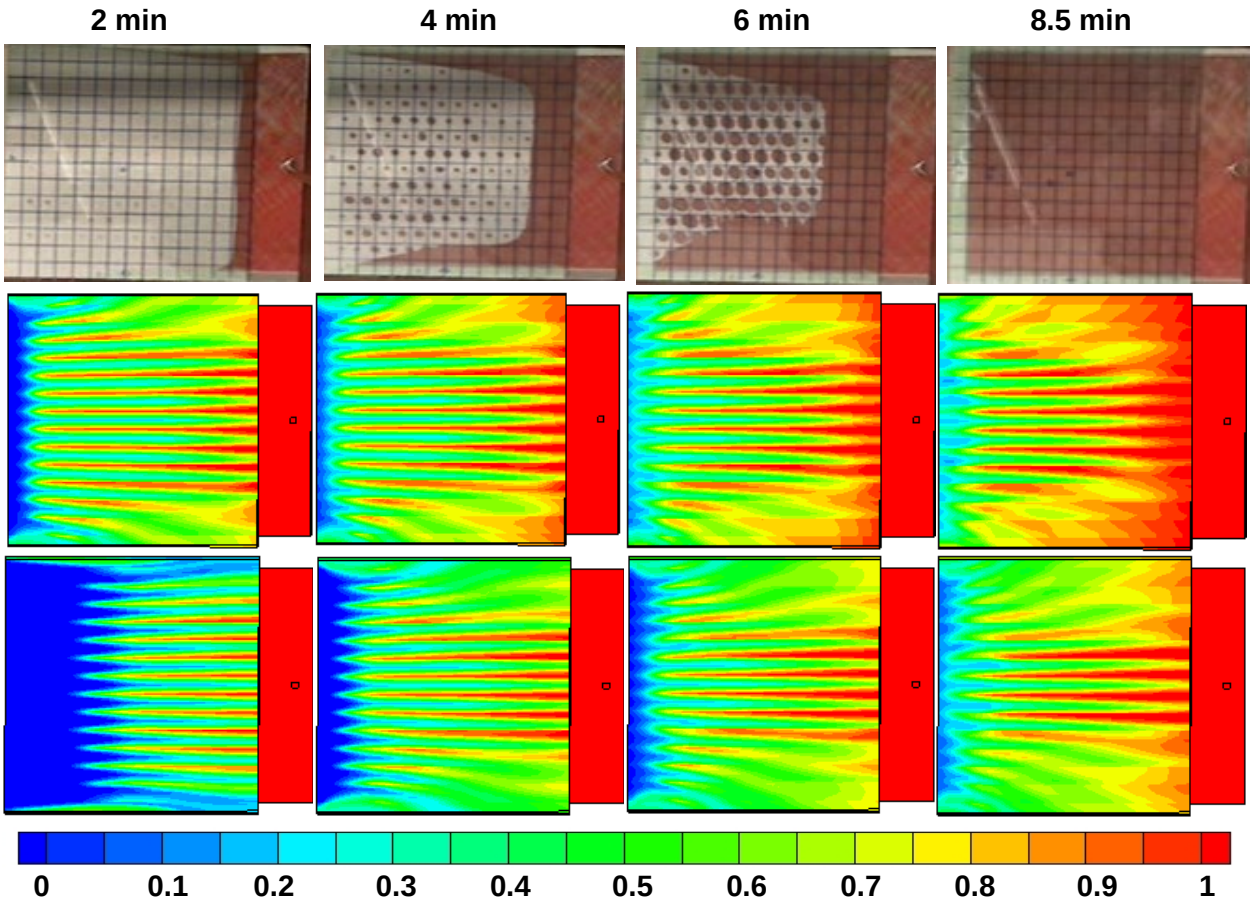

Figure 6.8 Flow patterns on the bottom surface of the hybrid preform. Comparison between the flow patterns predicted by the simulation model with the compaction model (middle) and without the compaction model (bottom). Shown for flow pathways with d=0.83 mm and S=2.54 cm in the VARTM process.

The effect of using a finer mesh or employing a smaller mesh size was also considered. As previously noted, the major planar dimension of the elements used in the original mesh was 6mm and one element was assigned per thickness of every individual layer. In this case study, the original mesh was refined in the in-plane surfaces by using two finer meshes of element sizes of 3 mm and 1.5 mm to see the effect of mesh size on the simulation results. In Figure 6.9, the flow patterns in the distribution medium on the top surface of the hybrid preform with flow pathways of 0.83 mm diameter and 2.54 cm spacing are shown with varying mesh size. For the top surfaces, the model predicted total infiltration times of about 68 and 63 seconds with the 3 mm

and 1.5 mm meshes, respectively compared with the previously predicted value of 70 seconds with the original mesh of 6 mm. The simulated cases shown in this section are for the VARTM process and use the measured strip permeability value.

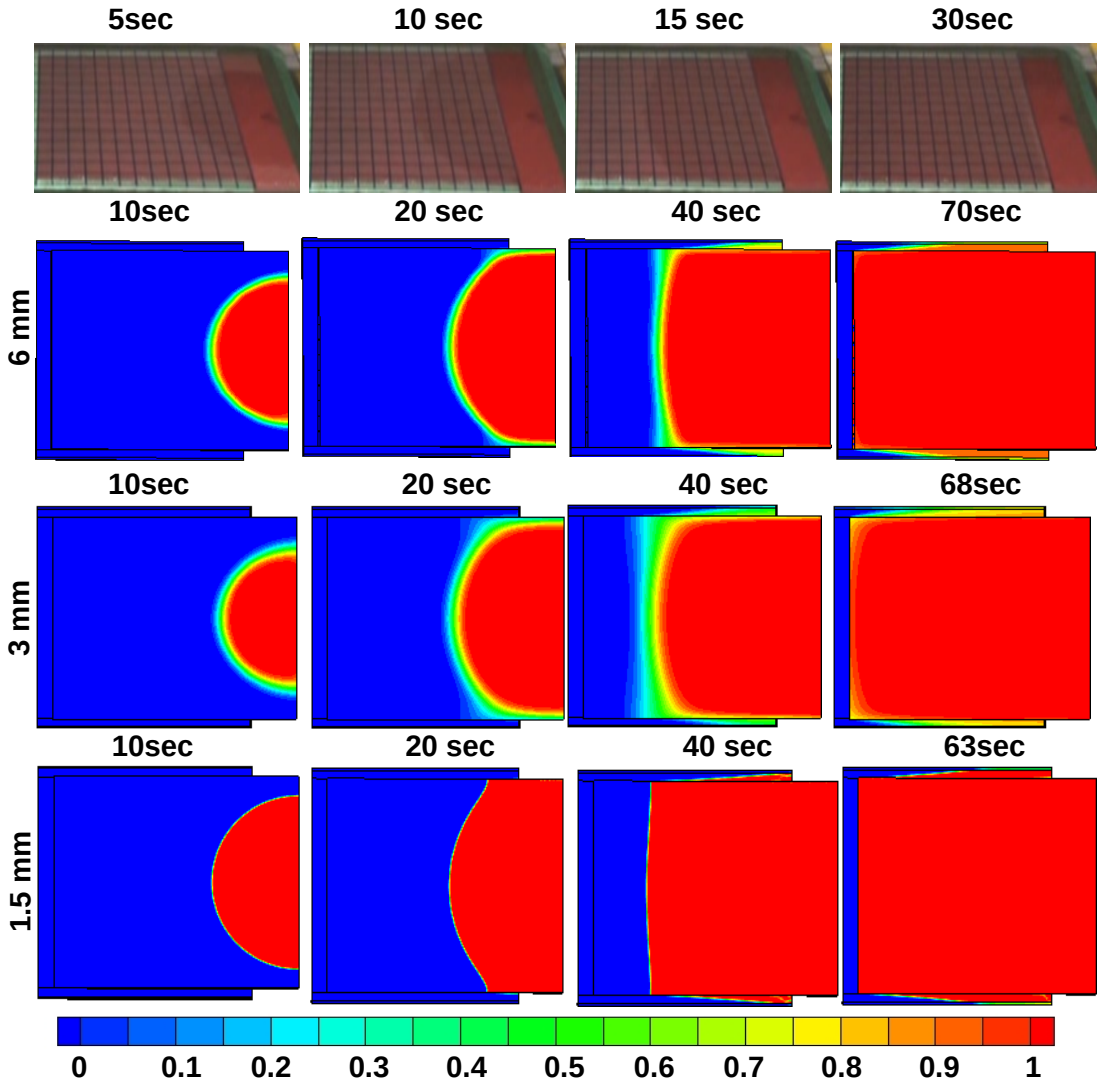

Figure 6.9 Flow patterns on the top surface of the distribution medium. Comparison between the flow patterns predicted by the simulation model with decreasing mesh sizes (6 mm, 3 mm and 1.5 mm) for flow pathways with d=0.83 mm and S=2.54 cm.

The effect of using finer meshes on the predicted flow patterns on the bottom surfaces of the same hybrid preform is shown in Figure 6.10. It is seen that by decreasing the mesh size, the simulated filling patterns of the porous strips slightly improves and the overall amount of infiltration seems to increase, however at a much higher computational cost.

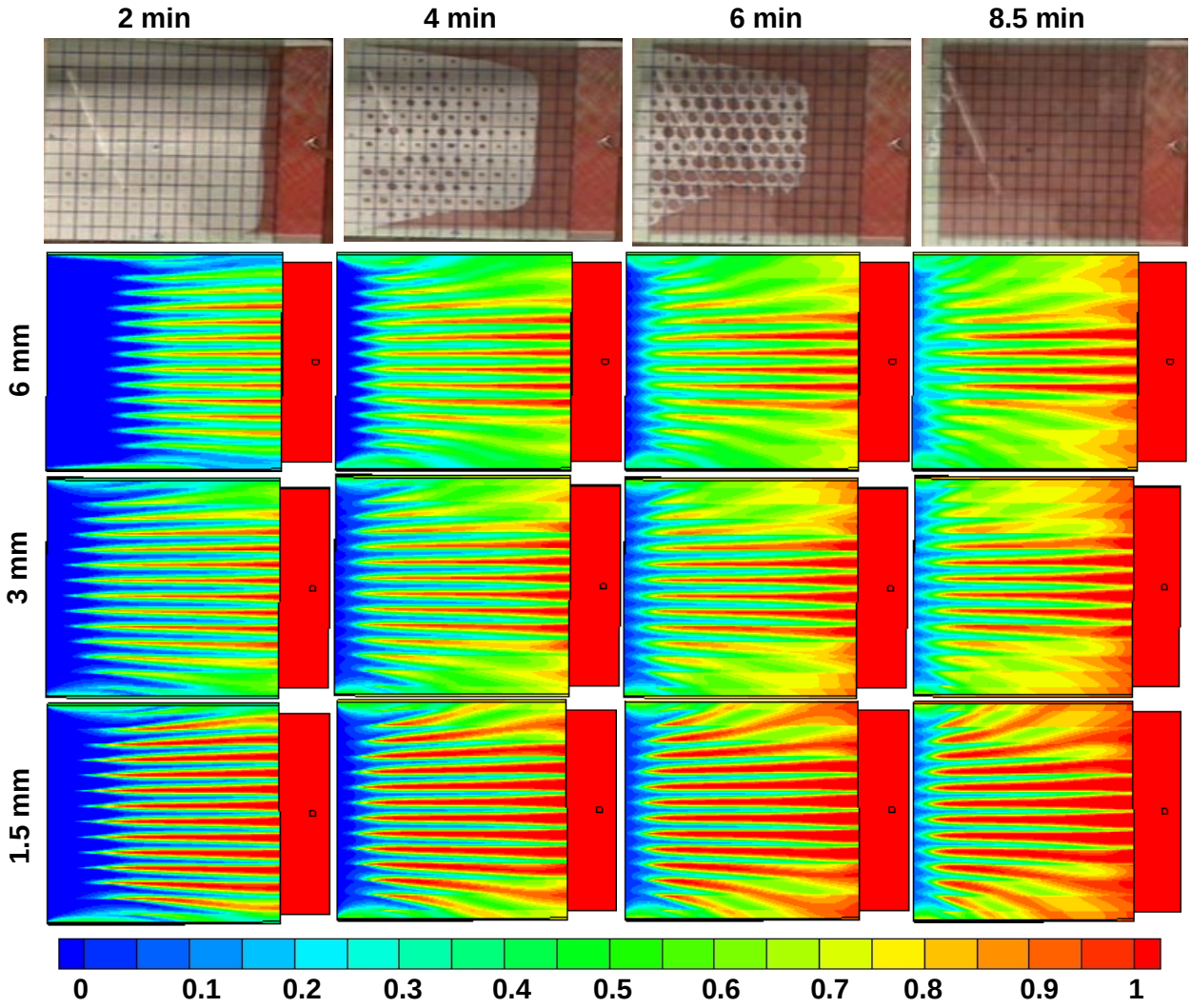

Figure 6.10 Flow patterns on the bottom surface of the hybrid preform. Comparison between the flow patterns predicted by the simulation model with decreasing mesh sizes (6 mm, 3 mm and 1.5 mm) for flow pathways with d=0.83 mm and S=2.54 cm.

The effect of flow pathway diameter and spacing are shown in Figures 6.11-6.16. In Figures 6.11 and 6.12, the flow patterns at the top and bottom surfaces of the hybrid preform are compared with the FLUENT simulation model results for pathways with 0.41 mm diameter and 2.54 cm spacing. Looking at the results, it is seen that the basic shapes of the flow patterns in the distribution medium were captured well. However, the predicted infiltration times were longer than measured. The total infiltration time of the distribution medium was measured to be 30 seconds whereas the predicted total infiltration time was about 70 seconds.

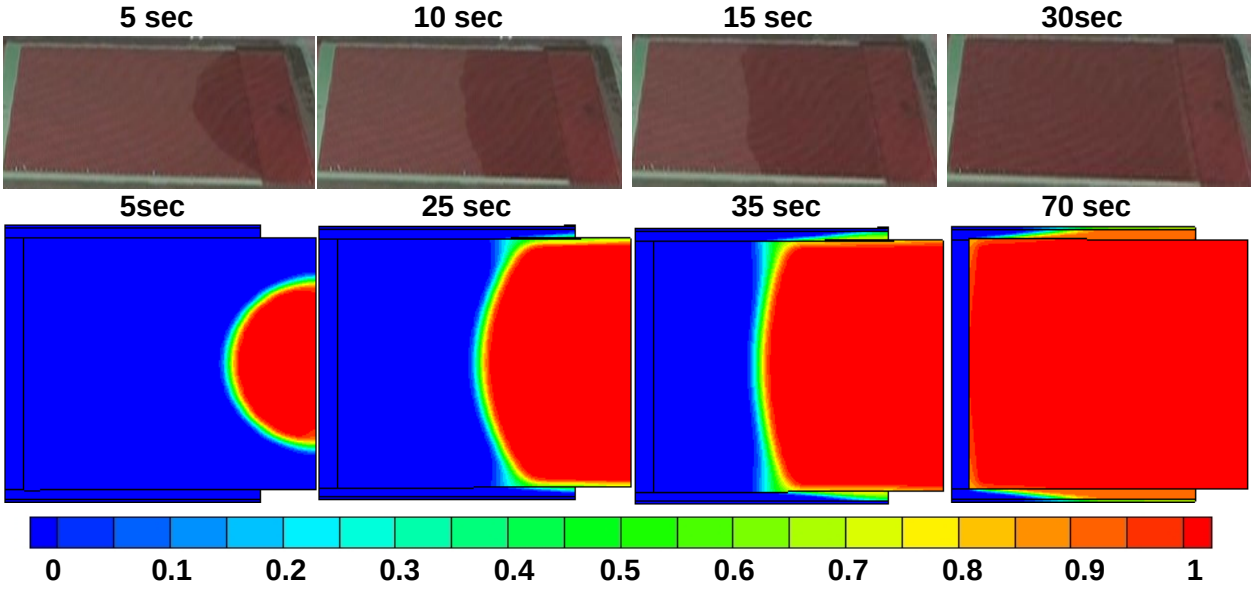

Figure 6.11 Flow patterns on the top surface of the distribution medium. Comparison between the flow patterns observed during the flow visualization test (top) and predicted by the simulation model (bottom) for flow pathways with d=0.41 mm and S=2.54 cm.

In Figure 6.12, the bottom surfaces reveal that the saturated and the unsaturated parts of the hybrid preform were predicted by the model reasonably well. The first two frames indicated no or minimal amount of infiltration which agrees with the simulation results. The amount of infiltration predicted by the model in the latter frames was less than 100 %, but the results still showed that the infiltration occurred and the resin volume fraction was between 0.65 and 0.75.

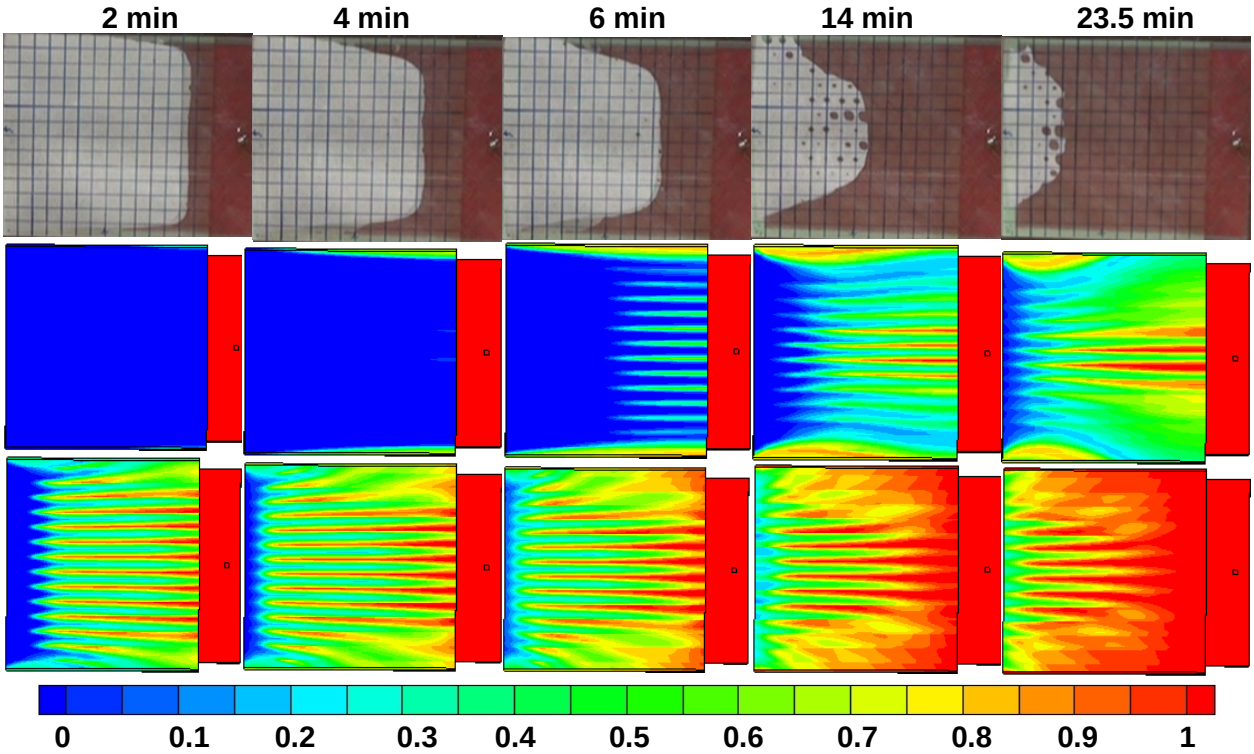

Figure 6.12 Flow patterns on the bottom surface of the hybrid preform. Comparison between the flow patterns observed during the flow visualization test (top) and predicted by the simulation model (bottom) for flow pathways with d=0.41 mm and S=2.54 cm.

Figures 6.13 and 6.14 show the flow patterns at the top and bottom surfaces of the hybrid preform for pathways with 1.59 mm diameter and 2.54 cm spacing. The simulation model seemed to predict the filling times correctly in the beginning of the infiltration process of the distribution medium. However, similar to the previous two cases, the simulated total infiltration time was larger than the measured value as shown in Figure 6.13. It can be concluded that the pathway diameter has no effect on the simulated filling and the total wet-out time of the distribution medium provided that the pathway spacing is kept the same. The simulated total wet-out time of the distribution medium for all pathway sizes with the 2.54 cm spacing was about 70 seconds whereas the measured value was about 30 seconds.

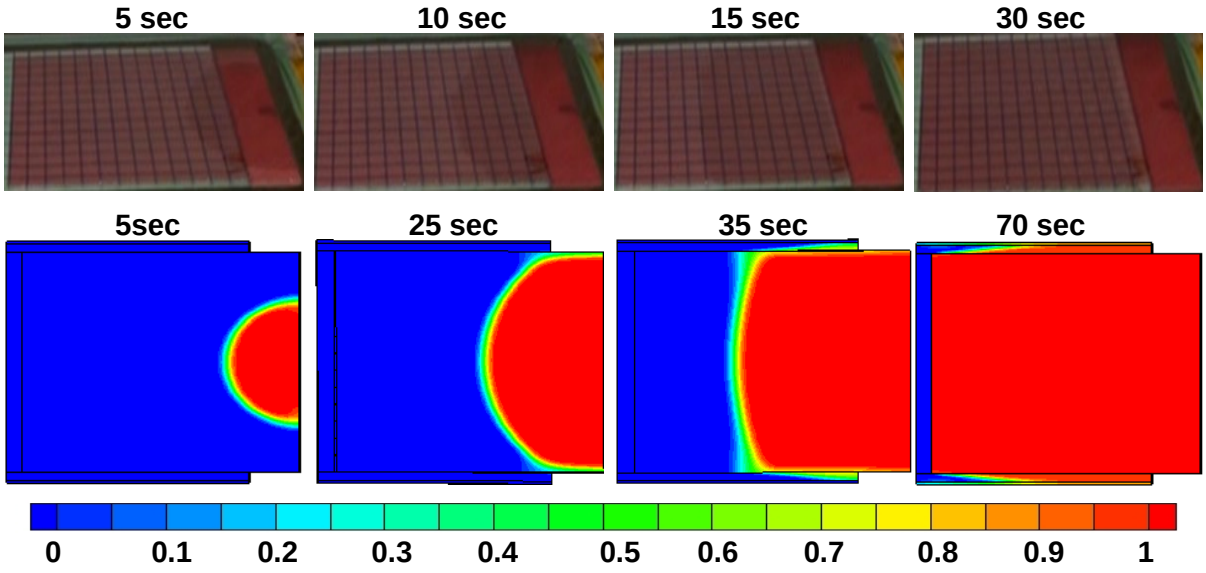

Figure 6.13 Flow patterns on the top surface of the distribution medium. Comparison between the flow patterns observed during the flow visualization test (top) and predicted by the simulation model (bottom) for flow pathways with d=1.59 mm and S=2.54 cm.

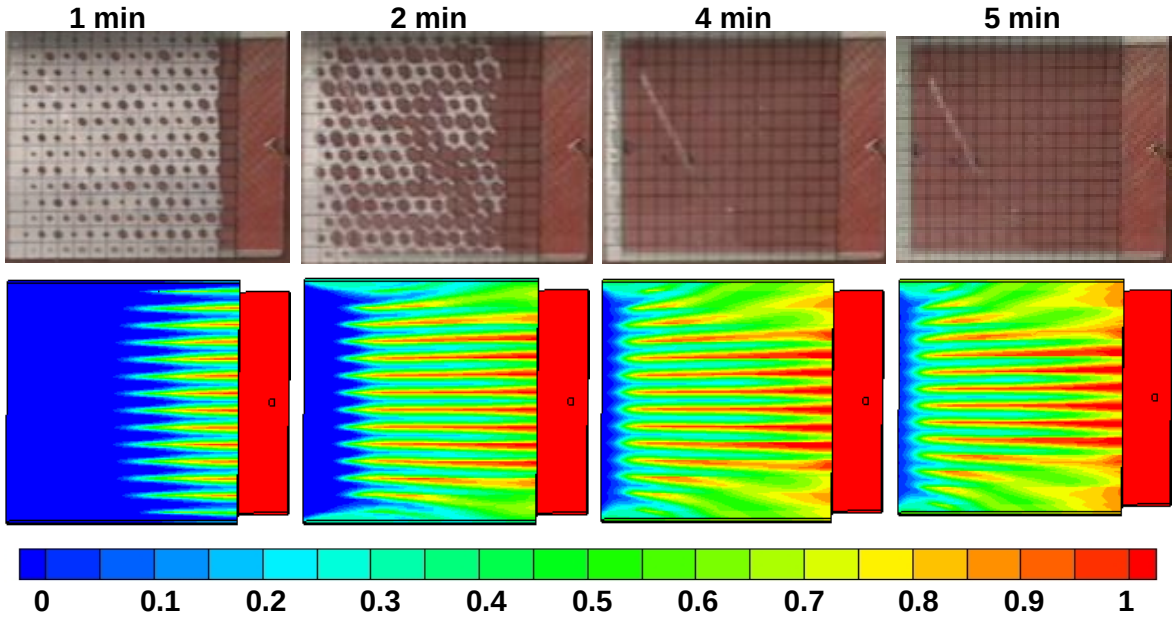

Figure 6.14 Flow patterns on the bottom surface of the hybrid preform. Comparison between the flow patterns observed during the flow visualization test (top) and predicted by the simulation model (bottom) for flow pathways with d=1.59 mm and S=2.54 cm.

The bottom surfaces shown in Figure 6.14 reveal a similar trend as in the previous case of pathways with 0.83 mm diameter. The model was able to simulate the filling of the pathways with the porous strips; however it was unable to match the measured total wet-out time of the hybrid preform and was also unable to capture the shape of the bulk flow front.

In Figures 6.15 and 6.16, the flow patterns at the top and bottom surfaces of the hybrid preform for pathways with 0.41 mm diameter and 1.27 cm spacing is shown. Although the measured total wet-out time for the distribution medium was about 33 seconds which is very similar to the cases discussed so far, the simulated total wet-out time dropped to 55 seconds as compared to the previously simulated value of 70 seconds. A possible reason for this is the existence of porous strips at the bottom surface of the distribution medium. In the model with the 1.27 cm spacing, there were twice as many porous strips compared to the models with the 2.54 cm spacing. Having more flow pathways in the VOF model could allow the second phase-air inside the distribution medium to be displaced at a higher rate by the first phase-resin. This could cause an overall reduction in the filling times. As the overall filling times decreased for the top surfaces, the first two simulated frames shown in Figure 6.15 seem to match the measured filling times reasonably well and then seemed to be lagging the experimental times in the latter frames. The bottom surfaces shown in Figure 6.16 reveal that the simulated frames captured the bulk flow front and the filling patterns well compared to the previous three cases with the 2.54 cm pathway spacing. An exception to this is seen at the last frame shown in Figure 6.16 where the model was unable to simulate the total wet-out time of the hybrid preform.

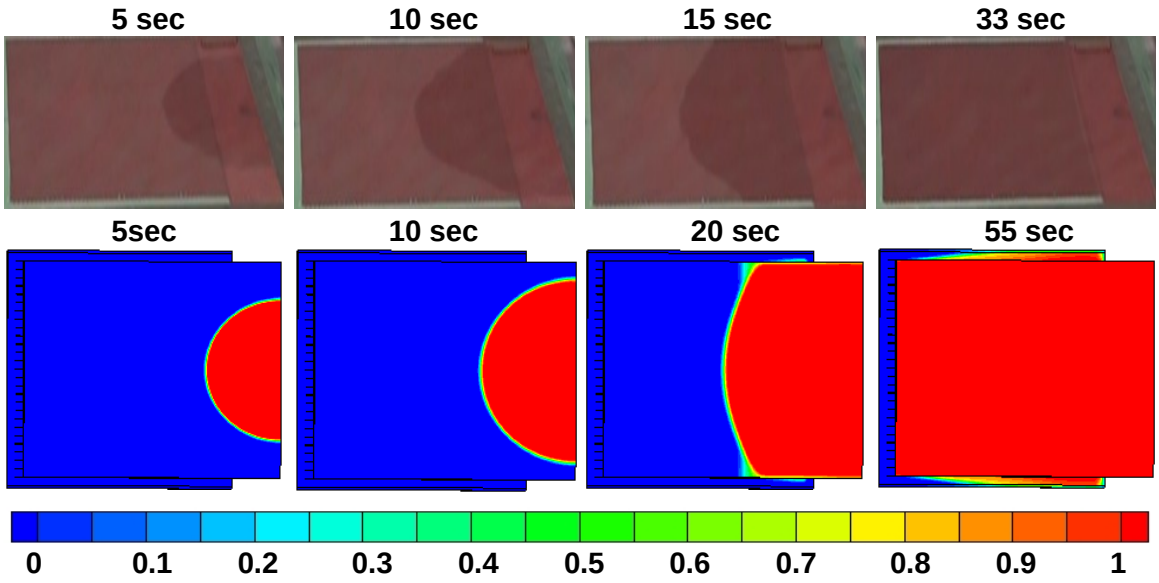

Figure 6.15 Flow patterns on the top surface of the distribution medium. Comparison between the flow patterns observed during the flow visualization test (top) and predicted by the simulation model (bottom) for flow pathways with d=0.41 mm and S=1.27 cm.

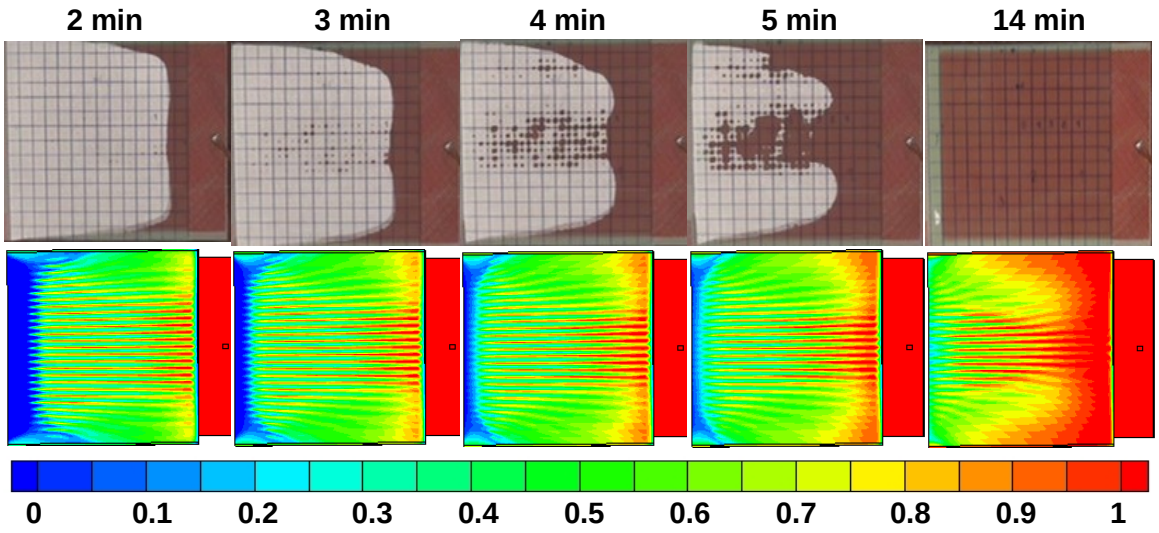

Figure 6.16 Flow patterns on the bottom surface of the hybrid preform. Comparison between the flow patterns observed during the flow visualization test (top) and predicted by the simulation model (bottom) for flow pathways with d=0.41 mm and S=1.27 cm.

6.2.2 Case Studies

In this section, the effects of permeability of the porous strips and the transverse permeability of the distribution medium on the flow patterns are discussed. Due to some discrepancies observed between the infiltration times of the experiments and of the model simulations in the previous sections, the transverse permeability of the porous strips was calculated by using an alternative approach to observe the impact of strip permeability on the flow patterns and infiltration times of the bottom surfaces.

An equivalent permeability expression was previously derived by Roy et al. [76] by equating the flow rate passing through an equivalent porous medium (porous strips in this study) to the flow rate passing through a set of holes (flow pathways in this study). The relation for the equivalent permeability of a porous strip is,

$$S_{strip} = S_{pathway}\,\phi_{strip} \tag{6.12}$$

where $S_{pathway}$ is the permeability of an individual pathway and ϕ_{strip} is the porosity of the strip or the plate with the holes on it. The porosity of a strip can be calculated as follows:

$$\phi_{strip} = \frac{Area\ of\ \ pathways}{Area\ of\ \ strip} = \frac{n\,\pi\,R^2}{w\,h} \tag{6.13}$$

where *n* is the number of the pathways, *R* is the radius of the pathway, and *w* and *h* are the width and length of the strip, respectively.

In the current model, the width of each strip was chosen to be equal to the corresponding flow pathway diameter and the length of each strip was chosen to be equal to the distance between the centers of the first and last flow pathway on a porous strip.

The equivalent permeability of a circular hole, in the case of fully developed laminar flow of an incompressible fluid along the length of the hole, can be derived by using Hagen-Poiseuille flow relations [77]. The complete derivation is given in Appendix A. The equivalent permeability of a circular hole is given by

$$S_{pathway} = \frac{R^2}{8} \tag{6.14}$$

Substituting Equations 6.13 and 6.14 into Equation 6.12 gives:

$$S_{strip} = \frac{n \pi R^4}{8 w h} \tag{6.15}$$

For Equation 6.15 to be valid, the flow must be in the fully developed region free of any entrance length effects. Thus, the entrance length should be much smaller than the acetate film thickness. In the current case, the calculated entrance length is about 1 to 2 orders of magnitude smaller than the acetate film thickness depending on the flow rates measured based on different pathway configurations. The calculations are shown in Appendix B. The porosity and equivalent permeability of the porous strips calculated using Equation 6.15 are given in Table 6.3 for different pathway diameters and spacings.

Table 6.3 The porosity and calculated equivalent permeabilities (based on Equation 6.15) of the porous strips.

Pathway Diameter (mm) and Spacing (cm)	S_{strip} (m^2)	ϕ_{strip}
0.41, 2.54	7.22e-11	0.0137
0.83, 2.54	5.97e-10	0.0276
1.59, 2.54	4.18e-9	0.0529
0.41, 1.27	1.43e-10	0.0273

The flow patterns on the top surface of the distribution medium are shown in Figure 6.18 where the measured porous strip permeability of 1.44e-12 m^2 (middle) and the calculated porous strip permeability 5.97e-10 m^2 (bottom) were used for preforms having pathways with the 0.83 mm diameter and 2.54 cm spacing. It is seen that the infiltration of the distribution medium was not affected by the change in porous strip permeability and the total wet-out time remained the same.

The model results shown in Figure 6.17 agrees well with the previously shown results for preforms with the pathways with the 2.54 cm spacing but with different diameters where the simulated infiltration times for the top surfaces remained about the same despite different strip permeabilities. However, the strip permeability is expected to have an impact on the infiltration time of the bottom surface of the hybrid preform.

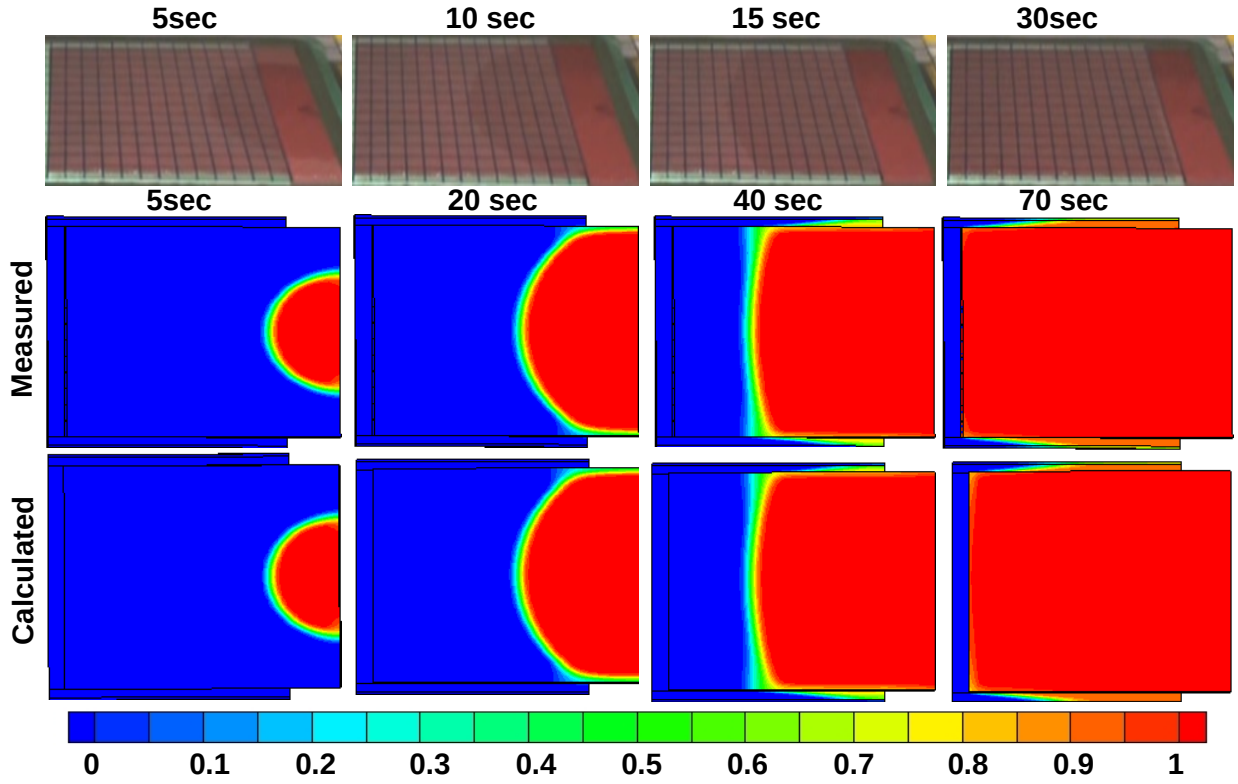

Figure 6.17 Flow patterns on the top surface of the distribution medium. Comparison between the flow patterns predicted by the two simulation models using calculated vs. measured strip permeability values of 1.44e-12 m^2 (middle) and 5.97e-10 m^2 (bottom) for flow pathways with d=0.83 mm and S=2.54 cm.

The effect of using the measured permeability versus using calculated porous strip permeability based on the alternative approach, on the bottom surfaces is shown for pathways with 0.41mm diameter and 0.83 mm diameter with 2.54 cm spacing in Figures 6.18 and 6.19, respectively. The simulated flow patterns using the measured and calculated strip permeability are shown at the middle and bottom of each figure, respectively.

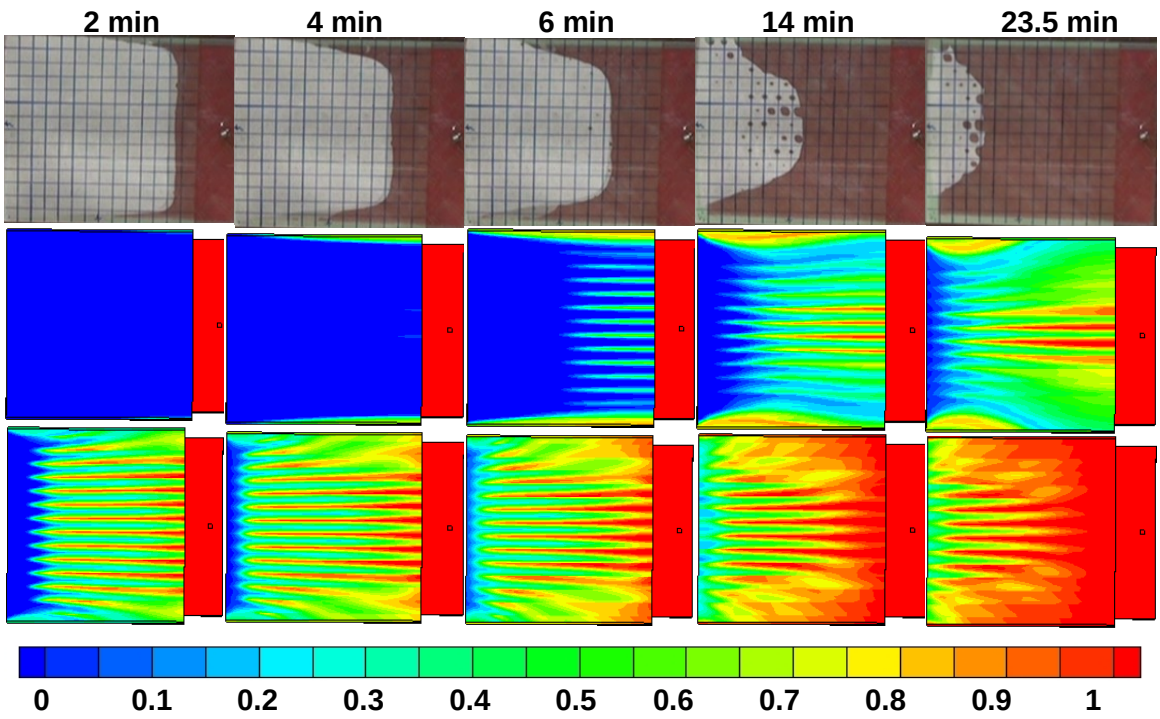

Figure 6.18 Flow patterns on the bottom surface of the hybrid preform. Comparison between the flow patterns predicted by the two simulation models using the measured vs. calculated strip permeability values of 1.08e-13 m^2 (middle) and 7.22e-11 m^2 (bottom) for flow pathways with d=0.41 mm and S=2.54 cm.

Figure 6.18 reveals that using the calculated strip permeability changed the simulated flow patterns at the bottom surface of the hybrid preform significantly. The preform got infiltrated significantly more and the flow pathway filling patterns were better simulated by the porous strips compared with the case using the measured porous strip permeability. However, the position of the bulk flow front was not captured well in either case. The top surfaces are not shown for the comparisons made here since strip permeability was shown to have no effect on the flow patterns or the infiltration times of the top surfaces of the hybrid preform.

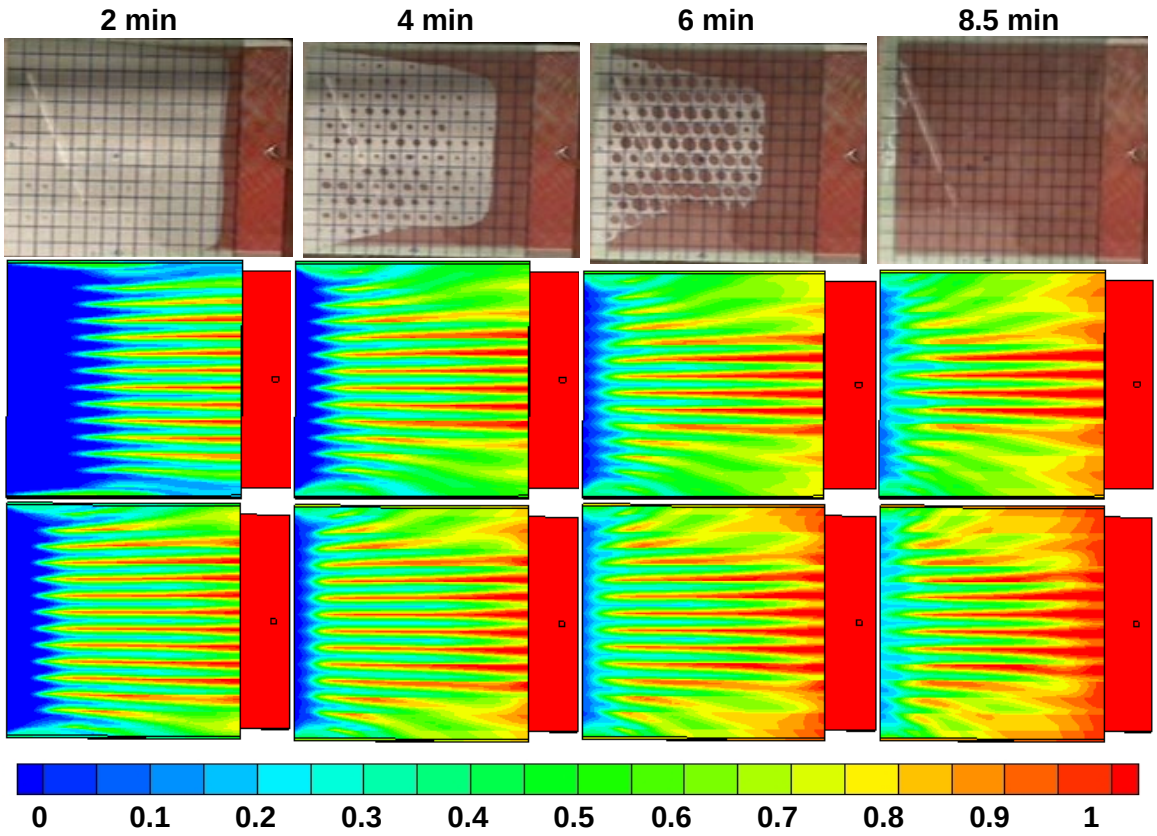

Figure 6.19 Flow patterns on the bottom surface of the hybrid preform. Comparison between the flow patterns predicted by the two simulation models using the measured vs. calculated strip permeability values of 1.44e-12 m^2 (middle) and 5.97e-10 m^2 (bottom) for flow pathways with d=0.83 mm and S=2.54 cm.

It was observed that using the measured versus calculated strip permeability had a significant effect on the flow patterns of the bottom surface of the hybrid preform with flow pathways of 0.41 mm diameter and 2.54 cm spacing. This is shown in Figure 6.18. It was also observed that the flow patterns were mainly dominated by the in-plane flow due to the small size of the flow pathways in this case.

However, as shown in Figures 6.19 and 6.20, in the case of flow pathways with the diameters of 0.83 mm and 1.59 mm, the transverse flow seemed to dominate the flow patterns. In addition, it

was observed that using the measured versus calculated strip permeability did not have a significant impact on the flow patterns in these two cases.

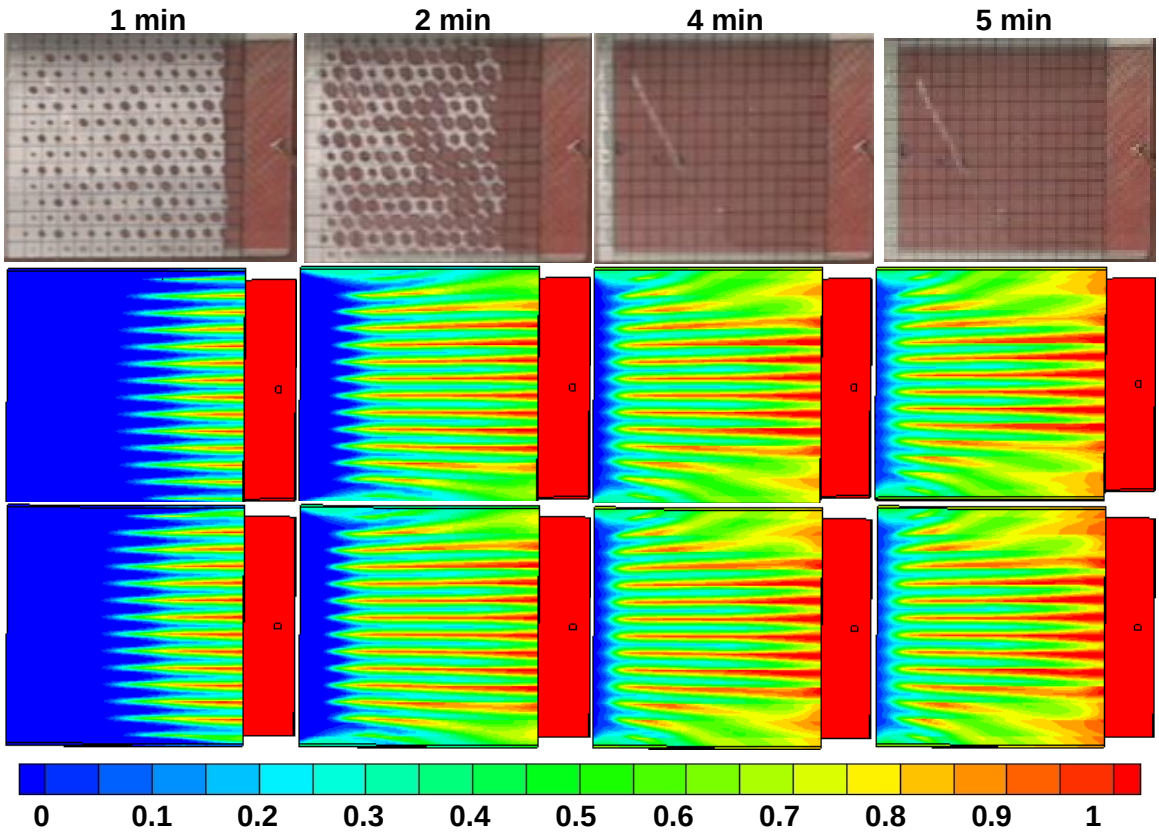

Figure 6.20 Flow patterns on the bottom surface of the hybrid preform. Comparison between the flow patterns predicted by the two simulation models using the measured vs. calculated strip permeability values of 6.91e-12 m^2 (middle) and 4.18e-9 m^2 (bottom) for flow pathways with d=1.59 mm and S=2.54 cm.

Looking at the comparisons made in Figure 6.18-6.20, it is seen that the strip permeability does not have a significant impact on the predicted flow patterns on the bottom surface of the hybrid preforms with the larger pathways where transverse flow seems to dominate within the preform. In contrast, the strip permeability seems to have a significant impact on the flow patterns on the bottom surface of the hybrid preform with the small pathways where in-plane flow seems to dominate within the preform.

The effect of transverse permeability of the distribution medium on the flow patterns in the distribution media can be observed in Figure 6.21. Looking at the model results presented in Section 6.2.1, it can be observed that the simulated total infiltration time for the distribution medium in the VARTM process was about twice of the total infiltration time measured during the flow visualization tests.

An attempt was made to find a value of transverse permeability for the distribution medium to be used as an input to the model instead of the originally used value so that the simulated total infiltration time would closely match the measured total infiltration time. Several simulations with varying values from 1.0e-9 m^2 to 1.0e-8 m^2 for the transverse permeability (Szz) of the distribution medium was performed as shown in Figure 6.21. The value originally used in the simulations was the measured Szz value of the distribution medium of 1.53e-10 m^2 as given in Table 5.3.

Looking at Figure 6.21, it is seen that for flow pathways with the 0.83mm diameter and 2.54 cm spacing, the simulated top flow patterns and the total infiltration time of the distribution medium closely matches with the observations of the flow visualization tests when a value of 1.0e-8 m^2 was chosen for the transverse permeability of the distribution medium. This was also verified by performing flow simulations for hybrid preforms with the 0.41 mm and 1.59 mm diameters and with the spacing of 2.54 cm.

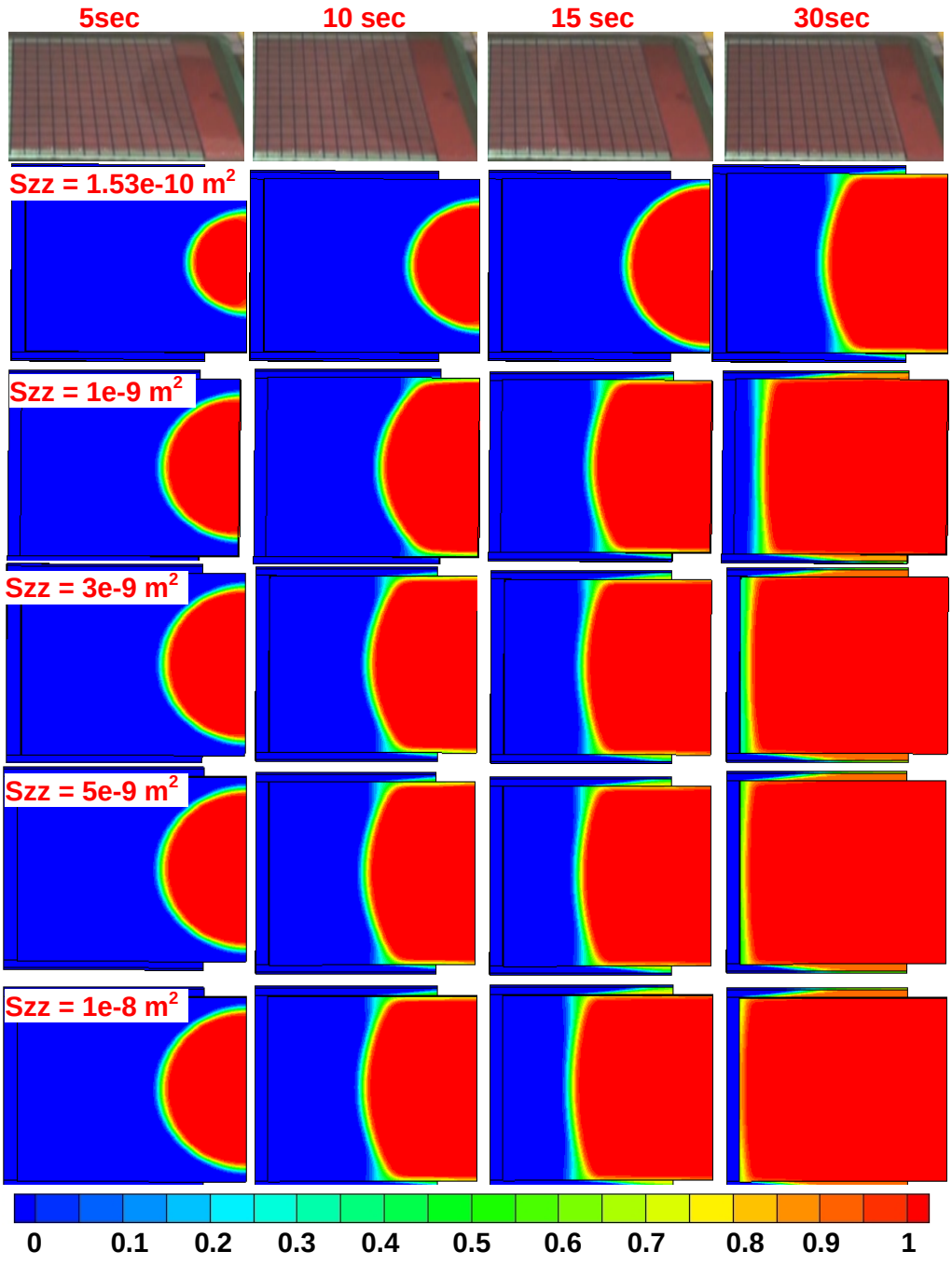

Figure 6.21 Flow patterns on the top surface of the distribution medium with d=0.83 mm and S=2.54 cm. Comparison between the flow patterns predicted by simulation models using varying transverse permeability (Szz) values of the distribution medium.

Figures 6.22-6.25 show the effect of using the value of 1.0e-8 m^2 versus the measured value of 1.53e-10 m^2 for the transverse permeability (Szz) of the distribution medium in the flow simulations. Flow patterns on the bottom surface of the hybrid preform are shown. The simulation results with the measured value of 1.53e-10 m^2 are shown at the bottom of each figure and the results with the value of 1.0e-8 m^2 are shown in the middle of each figure beneath the flow patterns observed in the flow visualization tests.

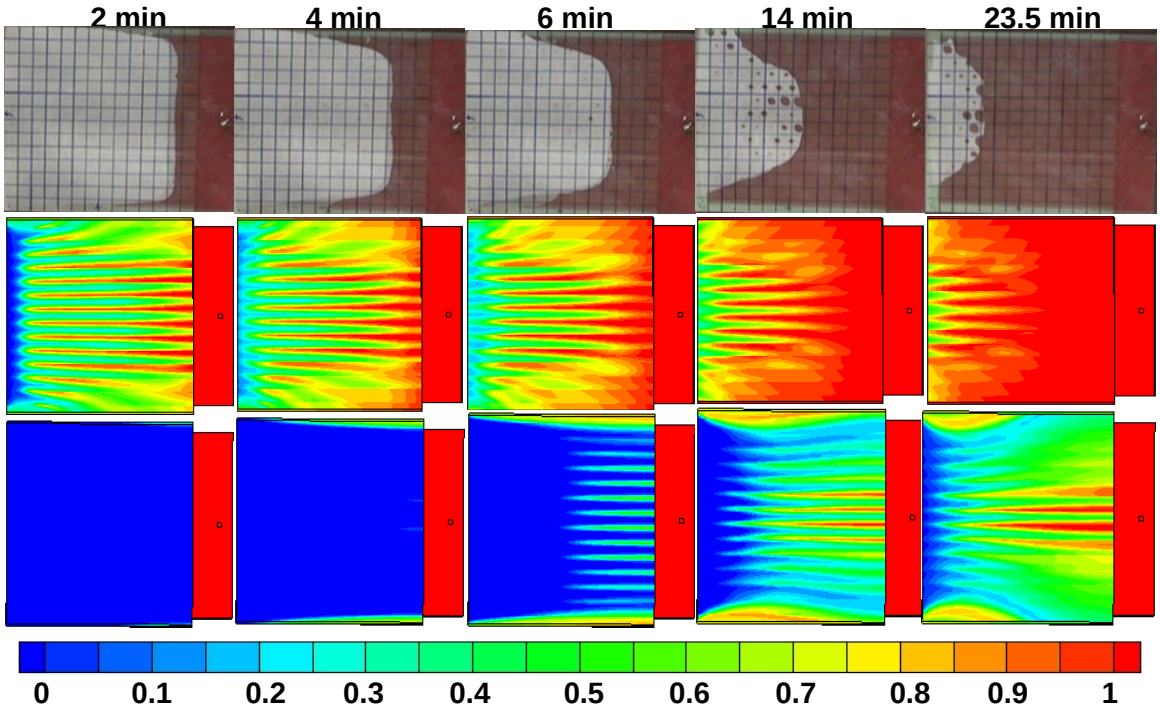

Figure 6.22 Flow patterns on the bottom surface of the hybrid preform. Comparison between the flow patterns predicted by two simulation models using a distribution medium transverse permeability (Szz) of 1.0e-8 m^2 (middle) and the measured value of 1.53e-10 m^2 (bottom) for flow pathways with d=0.41 mm and S=2.54 cm.

Figure 6.22 shows that the amount of infiltration on the bottom surface of the hybrid preform significantly increased when the value of 1.0e-8 m^2 was used for the transverse permeability of the distribution medium. This was shown for flow pathways with the 0.41 mm diameter and 2.54

cm spacing. The shape of the bulk flow front was captured better and a noticeable improvement was observed when compared with the predicted flow patterns using the measured value of 1.53e-10 m^2.

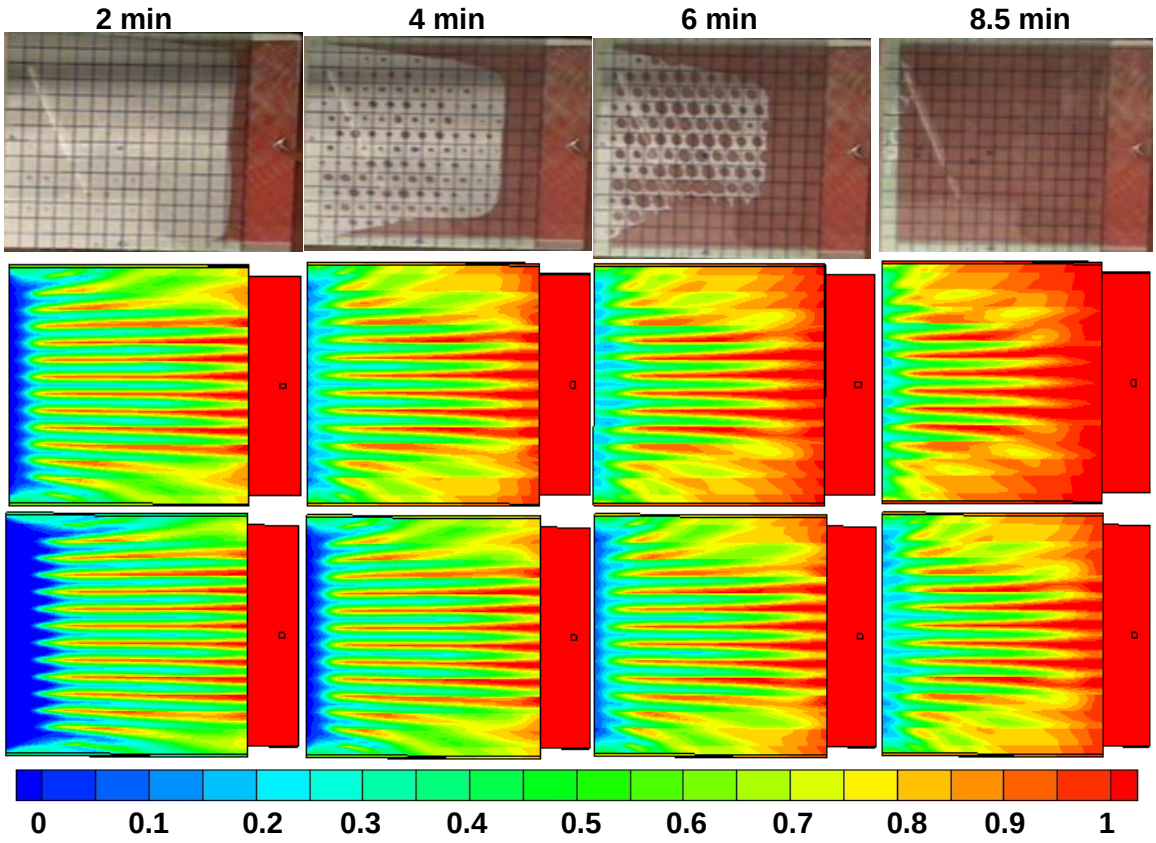

Figure 6.23 Flow patterns on the bottom surface of the hybrid preform. Comparison between the flow patterns predicted by two simulation models using a distribution medium transverse permeability (Szz) of 1.0e-8 m^2 (middle) and the measured value of 1.53e-10 m^2 (bottom) for flow pathways with d=0.83 mm and S=2.54 cm.

Figures 6.23-6.25 show that the predicted flow patterns on the bottom surface of the hybrid preform improved to some extent but not significantly when the value of 1.0e-8 m^2 was used for the transverse permeability of the distribution medium.

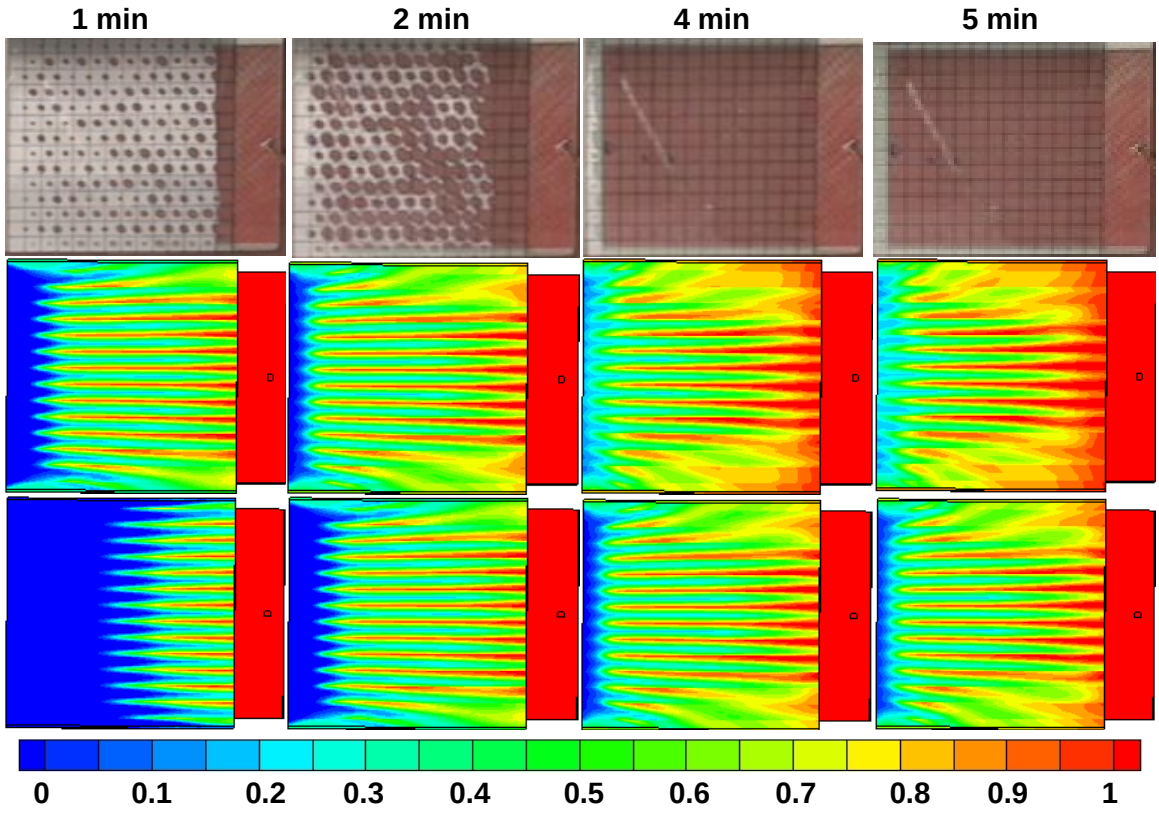

Figure 6.24 Flow patterns on the bottom surface of the hybrid preform. Comparison between the flow patterns predicted by two simulation models using a distribution medium transverse permeability (Szz) of 1.0e-8 m^2 (middle) and the measured value of 1.53e-10 m^2 (bottom) for flow pathways with d=1.59 mm and S=2.54 cm.

Despite the fact that the simulation results seemed to improve with the higher transverse permeability value of 1.0e-8 m^2 used for the distribution medium , the total wet-out times for the bottom surfaces of the hybrid preforms were still not captured well. This could be related to the fact that the two phase VOF model which assumed that air existed within the flow domain at all times. Hence, it could take longer time than simulated to displace all the air inside the preform so that the contour plot that shows the volume fraction of the resin could turn completely red; indicating no or minimal air remaining. This is contrary to the actual processes where there is vacuum inside the fixture. Thus, this could potentially allow for shorter measured total wet-out times than the simulated ones.

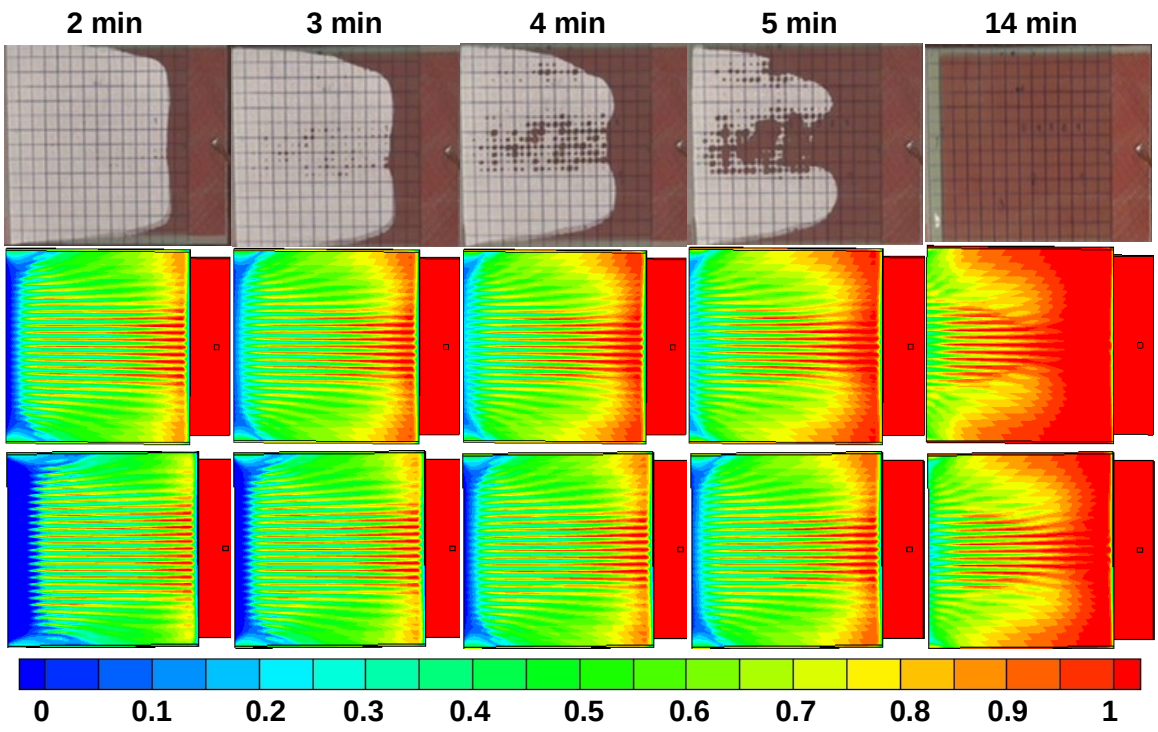

Figure 6.25 Flow patterns on the bottom surface of the hybrid preform. Comparison between the flow patterns predicted by the simulation model using a distribution medium transverse permeability (Szz) of 1.0e-8 m^2 (middle) and the measured value of 1.53e-10 m^2 (bottom) for flow pathways with d=0.41 mm and S=1.27 cm.

6.3 CAPRI Simulation Results and Comparisons with the Flow Visualization Tests

In this section, the CAPRI process simulation results will be compared to the flow visualization experiment results. Figures 6.26 and 6.27 show the simulation results for the hybrid preform with 0.41 mm pathway diameter and with 2.54 cm spacing at the top and bottom surfaces, respectively. It is seen that the simulated flow progression and the flow patterns at the top surfaces match very well with the experiments. The total infiltration time for the distribution medium in the CAPRI process was measured and simulated as 140 and 142 seconds, respectively.

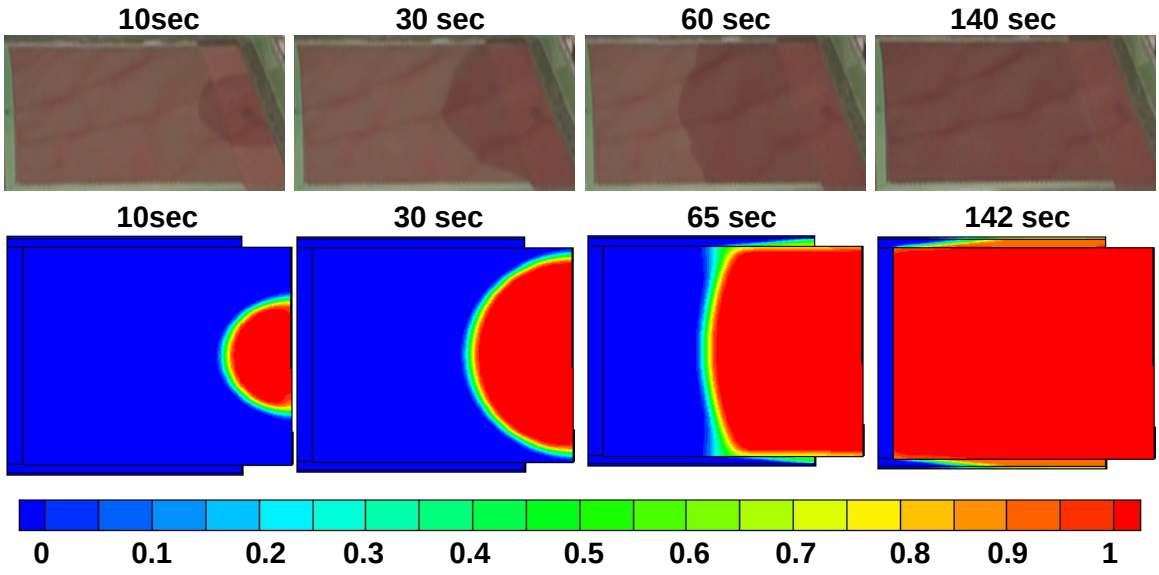

Figure 6.26 Flow patterns on the top surface of the distribution medium. Comparison between the flow patterns observed during the flow visualization test (top) and predicted by the simulation model (bottom) for flow pathways with d=0.41 mm and S=2.54 cm.

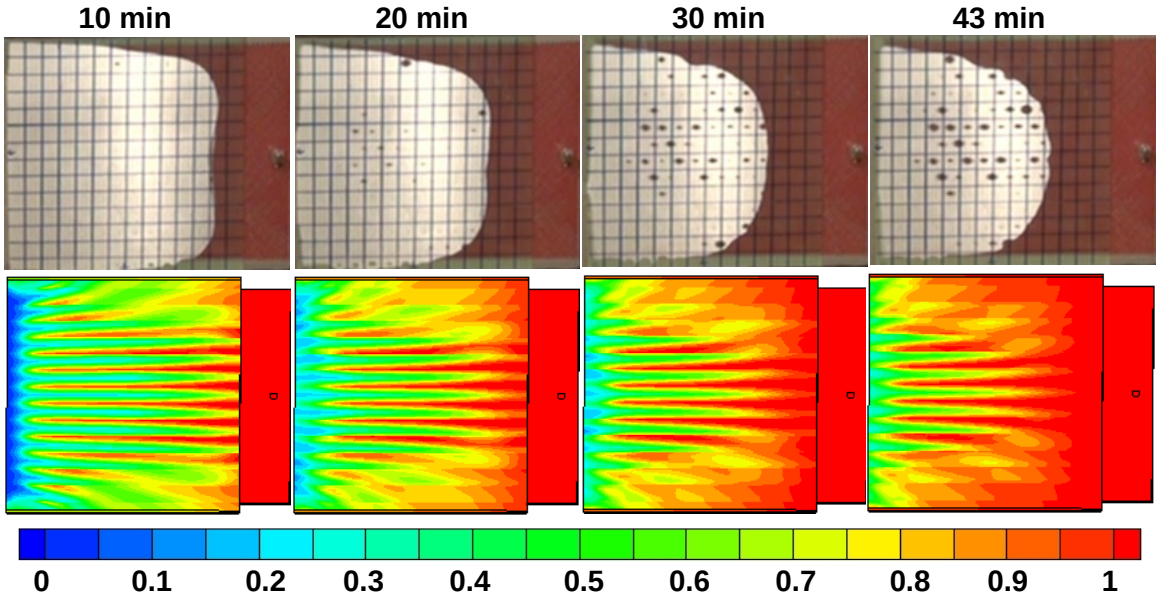

Figure 6.27 Flow patterns on the bottom surface of the hybrid preform. Comparison between the flow patterns observed during the flow visualization test (top) and predicted by the simulation model (bottom) for flow pathways with d=0.41 mm and S=2.54 cm.

The bottom surfaces as shown in Figure 6.27 revealed that the simulated filling patterns of the pathways by the porous strips and the simulated position of the bulk flow front agreed quite well with the experiments.

For pathways with 0.83mm diameter and 2.54 cm spacing, although the simulated times matched quite well with the experiments as shown in Figure 6.28, the total infiltration time for the distribution medium was measured as 160 seconds as opposed to the simulated value of the 140 seconds. The bottom surfaces as shown in Figure 6.29 reveal that the model was able to capture the filling patterns and the flow front position at the first two frames and then started to lag the experiment results. The simulated porous strips at 47 minutes were not completely filled as opposed to the experimental observations where the hybrid preform seemed to be completely wet-out at this time.

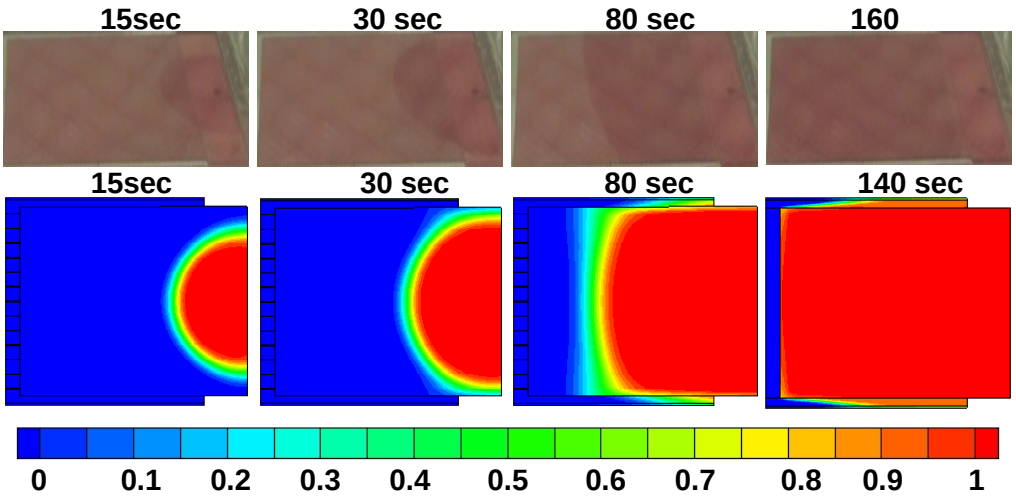

Figure 6.28 Flow patterns on the top surface of the distribution medium. Comparison between the flow patterns observed during the flow visualization test (top) and predicted by the simulation model (bottom) for flow pathways with d=0.83 mm and S=2.54 cm.

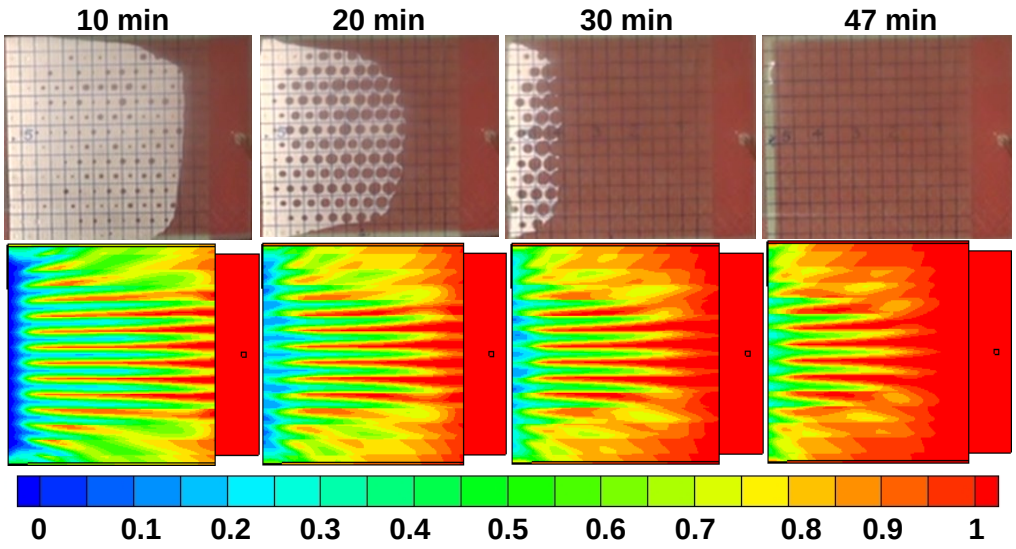

Figure 6.29 Flow patterns on the bottom surface of the hybrid preform. Comparison between the flow patterns observed during the flow visualization test (top) and predicted by the simulation model (bottom) for flow pathways with d=0.83 mm and S=2.54 cm.

Similar to the VARTM tests for the preform having pathways with 0.41mm diameter and 1.27 cm spacing, a reduction in the total infiltration time of the distribution medium was seen in the CAPRI tests with the same pathway configuration as shown in Figure 6.30. The simulated filling times and flow patterns for the top surfaces agreed quite well with the experiments except the frame showing the total infiltration time of 85 seconds. Another common result between the VARTM and CAPRI process simulations was that the simulated total infiltration time of the distribution medium remained the same for each process type regardless of the pathway diameter while keeping the same spacing. It is seen that the simulated total infiltration time of the distribution medium in the CAPRI process was twice (140 seconds vs. 70 seconds) compared with the VARTM process. The simulation results for the bottom surfaces in the case of the hybrid preform having pathways with 0.41mm diameter and 1.27 cm spacing is shown in Figure 6.31. Although the model seemed to capture the basic shape of the bulk flow front well, it could not capture the complex filling pattern of the pathways as measured in the experiments.

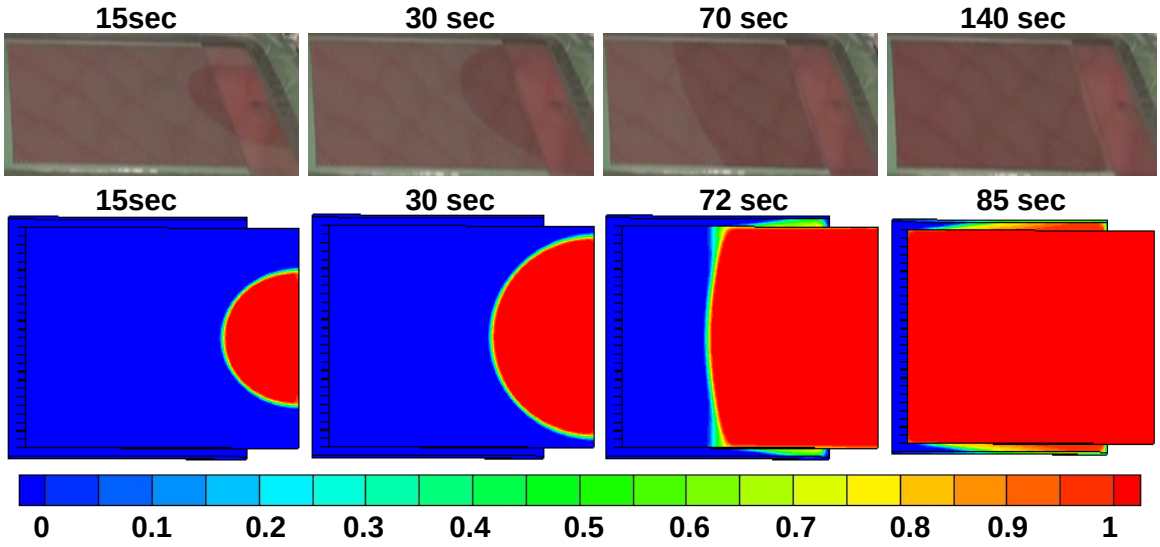

Figure 6.30 Flow patterns on the top surface of the distribution medium. Comparison between the flow patterns observed during the flow visualization test (top) and predicted by the simulation model (bottom) for flow pathways with d=0.41 mm and S=1.27 cm.

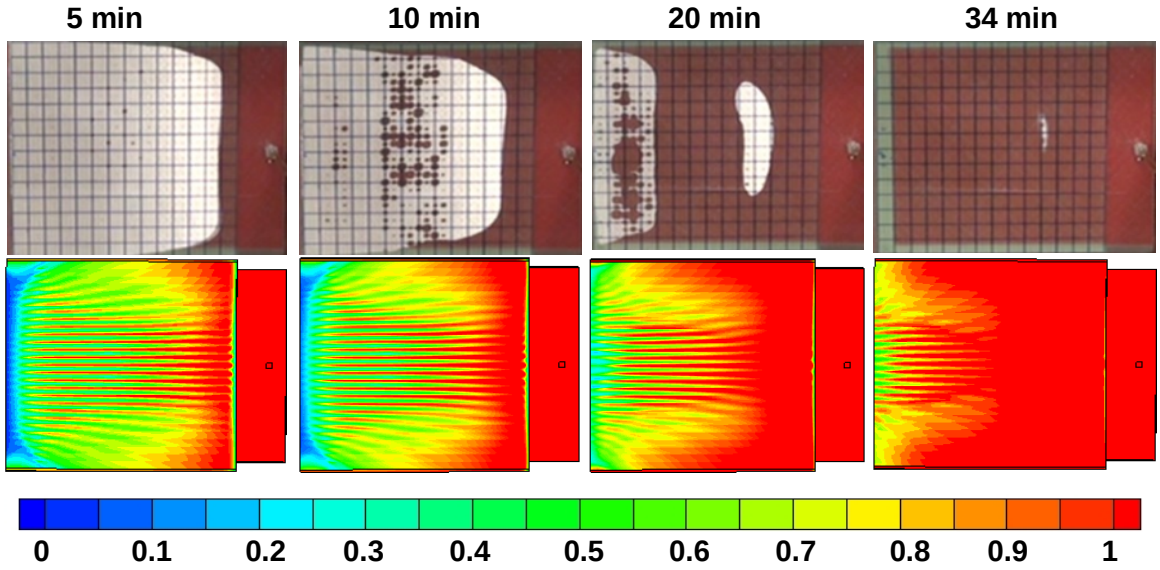

Figure 6.31 Flow patterns on the bottom surface of the hybrid preform. Comparison between the flow patterns observed during the flow visualization test (top) and predicted by the simulation model (bottom) for flow pathways with d=0.41 mm and S=1.27 cm.

6.4 Simulation Model Comparison for a Manufactured FML Part

In this section, flow patterns observed during the infiltration and manufacture of an actual FML panel is presented and compared with the flow patterns predicted by the developed simulation model. At NASA Langley Research Center, an FML panel was infiltrated with the SC-85 epoxy resin system. The FML panel was formed by stacking alternating layers of treated and primed 2024-T3 aluminum sheets of 0.381 mm thick and eight-harness satin weave S-glass fabric preforms. The hybrid preform consisted of five layers of aluminum sheets and four layers of S-glass fabric. The flow pathways in the aluminum sheets had a diameter of 0.41 mm and a spacing of 1.27 cm.

The hybrid preform was infused by a CAPRI/FML type of process on a steel tool. The tool and the resin pot were preheated to 27°C prior to the infiltration by using an air circulating oven. After the FML panel was completely resin infused, the system was cured at 38°C for two hours and at 71°C for six hours. A thermocouple was attached on to the vacuum bag to monitor the temperature of the resin.

In the flow simulations, the pressure at the injection port was set to 0.5 atm (50.66 kPa) for the CAPRI process. A resin viscosity of 0.516 Pa.s and a density of 1190 kg/m^3 were used. Figures 6.32 and 6.33 show the flow patterns on the top surface of the distribution medium and the flow patterns predicted by the simulation model at the chosen time frames. As shown in Figure 6.32, the model was able to capture the shape and position of the flow front in the distribution medium on the top surface of the hybrid preform.

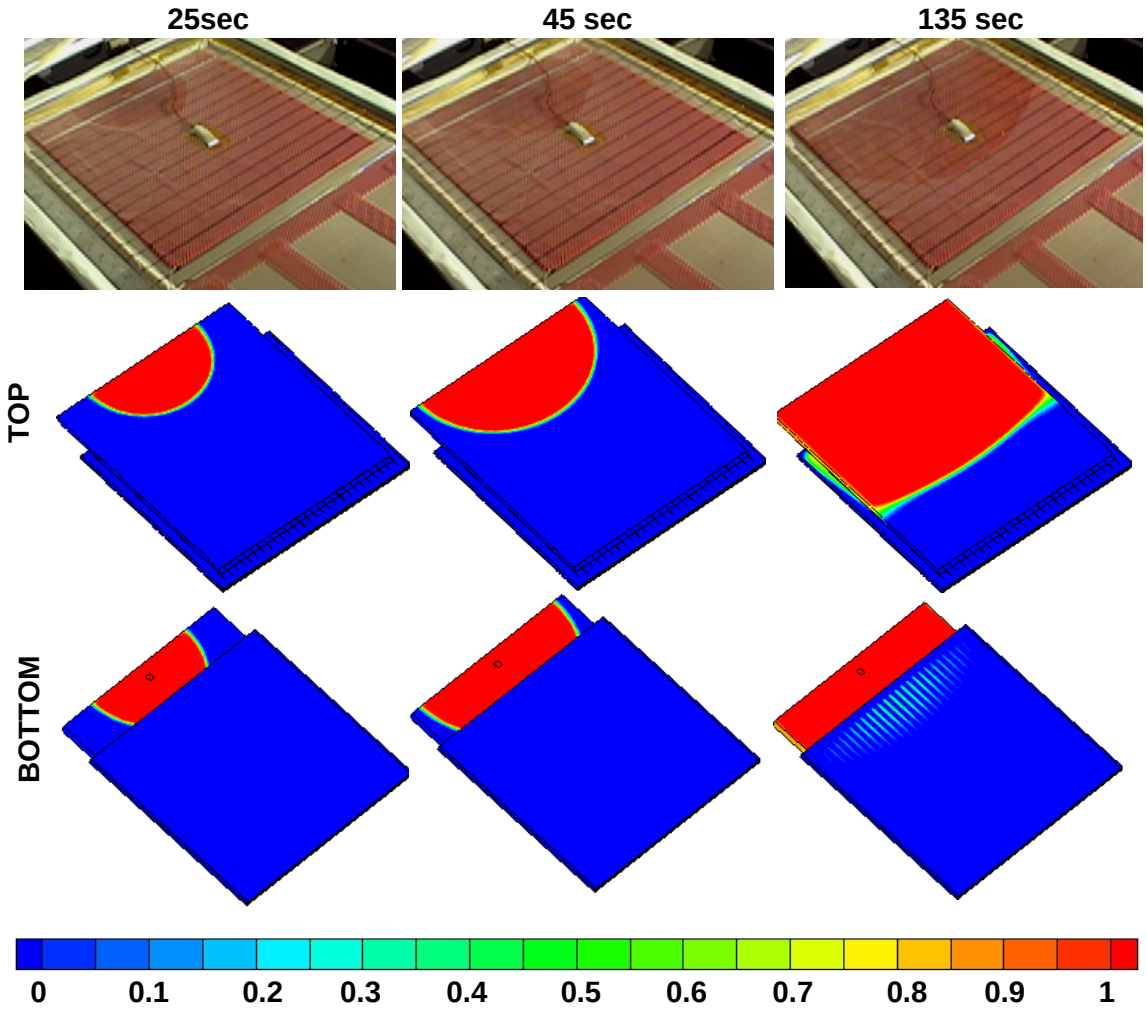

Figure 6.32 Flow patterns on the top surface of an FML panel observed during an FML/CAPRI process and flow patterns on the top and bottom surfaces predicted by the simulation model. Flow pathways of d=0.41 mm and S=1.27 cm were used.

According to the actual test results, the distribution medium was completely infiltrated at 4 minutes and 25 seconds, as shown in Figure 6.33. The total infiltration time of the distribution medium was predicted as 4 minutes by the simulation model. The complete infiltration of the hybrid preform was completed in about an hour. The flow patterns and the infiltration times predicted by the simulation model of a CAPRI/FML process agreed quite well with the actual test measurements.

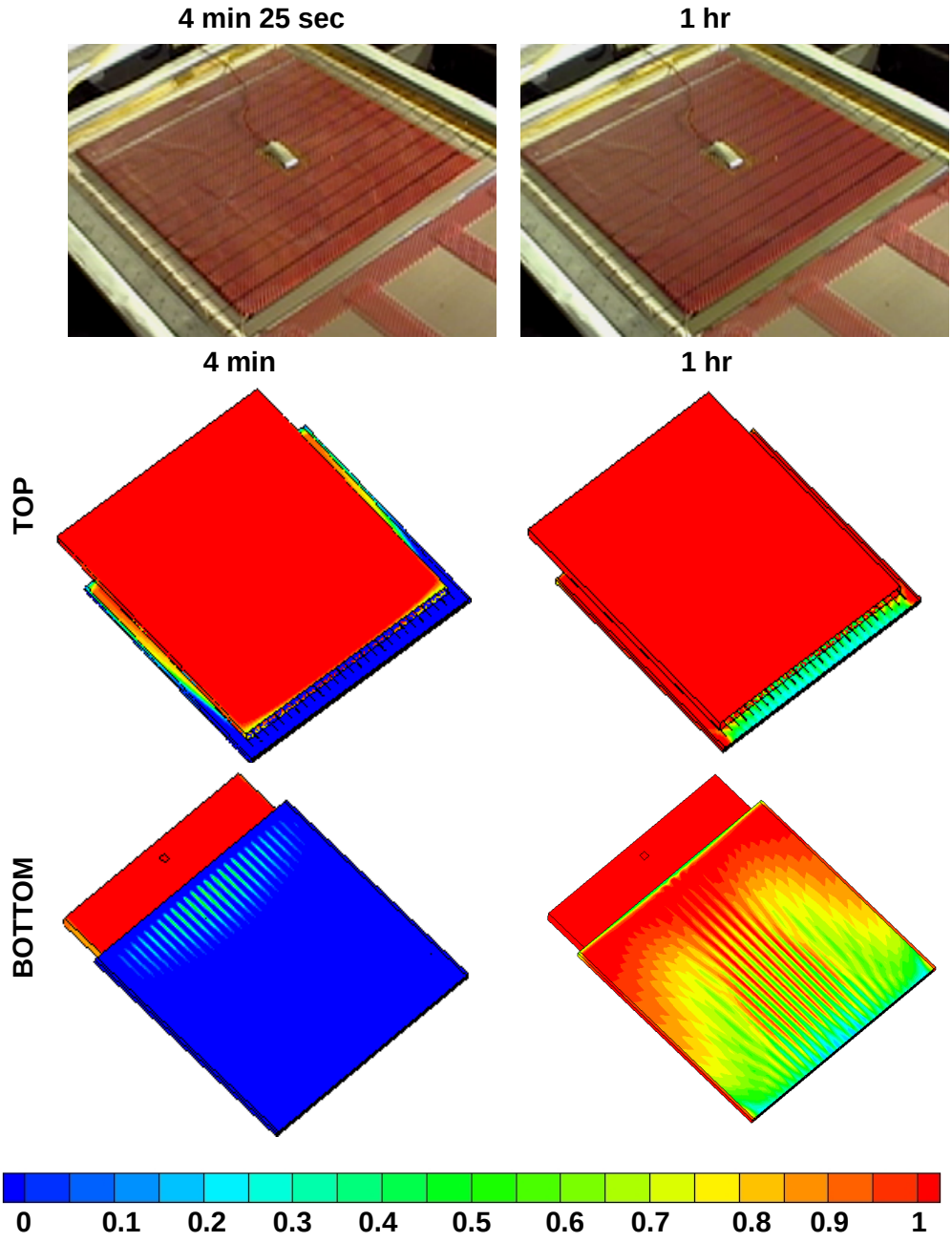

Figure 6.33 Flow patterns on the top surface of an FML panel observed during an FML/CAPRI process and flow patterns on the top and bottom surfaces predicted by the simulation model. Flow pathways of d=0.41 mm and S=1.27 cm were used.

6.5 Summary

In this chapter, the results of the FLUENT simulation model of the VARTM/CAPRI FML processes was presented and compared with the flow visualization experiments. The three dimensional model used the VOF two phase resin-air model to track the flow patterns and used the mathematical models for the compaction and permeability data of the preform materials to determine the inputs to the simulations. Inside the hybrid preform, the pathways on the acetate films were modeled as porous strips to create a simpler, a more stable and robust model. The permeability of the porous strips was determined using two techniques: calculated using the relation given in Equation 6.10 based on Hagen-Poiseuille flow relations and using the measured experimental values given in Chapter 5.

Initial results for the top surfaces showed that the simulations lagged the experimental total wet-out times of the distribution medium with the current inputs; the total wet-out time for the top surfaces was measured as 30 seconds versus the simulated time of 70 seconds. Both the calculated and measured permeability values were used for the porous strips. Results with the 2.54 cm pathway spacing and with different pathway diameters and strip permeabilities showed that the flow patterns for the top surfaces were very similar and the total wet-out times were about the same for each case. Thus, it was concluded that the pathway diameter and strip permeability had no effect on the infiltration of the distribution medium provided that the pathway spacing was the same for all cases.

For the preforms with the 1.27 cm spacing, the simulated total wet-out time for the top surfaces still lagged the measured time however by a smaller fraction. The measured total wet-out time

for the top surfaces was 33 seconds versus the simulated time of 55 seconds. This was tied to the fact that the VOF model could be showing a faster simulated infiltration in the case of the 1.27 cm pathway spacing compared to the model with the 2.54 cm pathway spacing due to the existence of twice as many porous strips at the bottom surface of the modeled distribution medium and thus allowing the air included in the model to be displaced by the resin through the strips at a faster rate.

It was found out that the strip permeability had no effect on the flow patterns of the top surfaces (distribution medium) provided that the pathway spacing was kept the same. This was an expected result since flow pathways or porous strips exist only at the bottom surface, not inside of the distribution medium. When the results of the models using the calculated and measured strip permeabilities were compared, it was seen that when the transverse flow inside the preform tends to dominate over the in-plane flow; typically for larger pathway diameters, no significant differences were observed in the results between the two cases. For the preforms having pathways with 0.41 mm diameter and 2.54 cm spacing, it was observed that the model with the measured strip permeability gave unsatisfactory results and was not able to capture the flow patterns well when compared with the model with the calculated strip permeability. However, in other cases, i.e. preforms with 0.83 mm and 1.59 mm pathway diameter with the 2.54 cm spacing, no significant differences were observed between using the calculated versus measured strip permeability values. To summarize, the strip permeability has no effect on the flow patterns and infiltration times of the top surfaces. For the bottom surfaces, the strip permeability has some effect for the smaller diameter pathways whereas no significant impact on the flow patterns and times was observed for the larger diameter pathways.

In order to match the experimental total wet-out time of the distribution medium, a different value for the transverse permeability of the distribution medium was used. This value was found to be 1.0e-8 m^2 by making several simulations of the top surface with varying Szz values for the distribution medium. When the simulations were re-run with the new value, the VARTM simulations for the top surfaces showed a much shorter total wet-out time of about 30 seconds closely matching the experimental measurements for the cases with the 2.54 cm spacing. Using the new value also seemed to slightly improve the flow patterns at the bottom surfaces in the VARTM process by showing an overall higher amount of infiltration of the hybrid preform and faster flow front progression. However, the overall impact on the bottoms surfaces was not significant.

Using the new transverse permeability value of 1.0e-8 m^2 for the distribution medium for the CAPRI process simulations, although not shown, would obviously not have the same effect as shown with the VARTM process simulations. The CAPRI process simulations performed with the originally used measured value of the transverse permeability for the distribution medium already proved close to satisfactory results at the top and bottom surfaces of the hybrid preform. The simulated total wet-out time for the distribution medium of about 140 seconds seemed to relatively match the measured times of 140 seconds and 160 seconds for the pathways with the 2.54 cm spacing and with the 0.41 mm and 0.83 mm, respectively. Thus, rerunning the simulations with the much higher Szz value of 1.0e-8 m^2 would definitely result in an over reduction in the simulated times at the top surface and the measured times would lag the simulated times.

Decreasing the mesh size seemed to improve the simulation results at the top and bottom surfaces although it did not affect the results significantly. At the top surfaces, the total wet-out time reduced up to 10% with the finer meshes. As for the bottom surfaces, the infiltration of the porous strips became more visible and the overall infiltration of the hybrid preform increased. Observing the individual layers proved that the amount of infiltration of the individual layers was not uniform. The layers closer to the distribution medium showed a higher amount of infiltration and showed flow patterns that were slightly better matching with the measured results.

Overall, it can be concluded that the simulation model is most sensitive to the inputs used for the transverse permeability of the distribution medium rather than the inputs used for the porous strip permeability. Comparing the two processes of VARTM and CAPRI, it was observed that the simulated flow patterns and the infiltration times for the CAPRI process agree better with the experimental observations. The flow patterns and the infiltration times predicted by the simulation model for a CAPRI/FML type of process agreed quite well with the observations of an actual FML panel infiltration test performed at the NASA Langley Research Center. Finally, it was shown that further improvements in the simulation model of the VARTM process can be made by the addition of the compaction model as a user defined function to the solver.

Chapter 7

SUMMARY AND CONCLUSIONS

7.1 Summary and Conclusions

In this study, a combined experimental and numerical study was performed to investigate the manufacture of FMLs by the Vacuum Assisted Resin Transfer Molding (VARTM) and Controlled Atmospheric Pressure Resin Infusion (CAPRI) processes.

The compaction behaviors of the preform materials used in the FML structures were characterized under different test conditions and the pressure vs. fiber volume fraction data was fit to mathematical models. Similarly, the permeabilities in the principal material directions were measured and the fiber volume fraction vs. permeability data was fit to mathematical models. The mathematical models proposed for the compaction and permeability characterization studies were used to determine the input parameters of the simulation model such as initial volume fraction, permeability and the model constants for the user defined compaction model.

Flow visualization studies were performed to analyze the infiltration of the FMLs using the VARTM and CAPRI processes. It was found out that FMLs can be successfully infiltrated by these processes when flow pathways were machined into the acetate films. In most cases, the hybrid preforms were completely infiltrated with no dry spots.

A simulation model of the hybrid preform structure of the FMLs was developed using the commercial software package FLUENT. The model was used to predict the flow patterns and the infiltration times at the top and bottom surfaces of the hybrid perform during the resin infusion stage of the VARTM and CAPRI processes. The simulation model results were compared with the results of the flow visualization tests.

The results of the flow simulation studies when compared with the flow visualization tests revealed that the diameter of the flow pathways inside the hybrid preform and thus the permeability of the porous strips used to model them did not have an effect the flow patterns on the top surface of the hybrid preform. Hence, the total infiltration time for the distribution media when tested with hybrid preforms with different pathway configurations remained about the same. An exception to this was seen for the simulated case of the hybrid preform with the smaller 1.27 cm spacing. This was related to the physics of the two phase VOF model. With the smaller spacing and more pathways on each acetate layer, twice as many porous strips with higher strip permeability existed in the model. This could allow the air to be displaced faster through the porous strips at the bottom surface of the distribution media and thus resulting in shorter simulated filling times when compared with the larger 2.54 cm spacing models with less number of strips and with lower strip permeability.

The transverse permeability of the porous strips was predicted by using two methods. One was experimentally measuring the permeability of a downsized acetate film specimen of about one seventh of the original size of an acetate film. The porosity of the downsized specimen was about the same of the original specimen. For highly porous media such as acetate films with the 1.59 mm diameter and the distribution media, where a direct permeability measurement of the

individual layers was not possible, permeability measurements were done with the downsized hybrid specimens. An analytical relation was used to relate the hybrid permeability measurement results and the bulk permeability of the specimens. The hybrid measurements typically included the specimen tested in the middle and two layers of glass fabric at the top and bottom surfaces. The assumption made in this method was that the middle layer had a thickness equal to the measured thickness at the load free condition. This assumption is reasonably accurate for preforms with minimal deformation when compacted such as the acetate films. However, some error is present when this assumption is applied for the distribution media. To be able to solve the analytical relations with the same number of unknowns, the glass fabric layers at the top and bottom surfaces were assumed to have the same compacted thickness and thus the same volume fraction. Some minor error in the results is also expected to be involved here due to this assumption.

The second method of predicting permeability was using an expression derived based on the Hagen-Poiseuille flow relations. This relation required using the porosity values of the porous strips used in the model. For this relation to hold, the flow should be free from the effects of all body forces including gravity and the flow should be in the fully developed region i.e. free from any entrance length effects. The difference between the permeability values predicted using the two methods were about two orders of magnitude as seen in Tables 5.2 and 6.3. This is somewhat an expected result. The first method measures the permeability of an acetate specimen representing a full size acetate film of the same porosity. The second method calculates a predicted permeability of a single porous strip valid under fully developed laminar flow conditions and the calculation was mainly based on the calculated strip porosity. The porosity of

a single layer of acetate film is obviously different than the porosity of a single porous strip and thus their permeabilities are also expected to be different. No constitutional relation between the permeability and porosity was established in this study for acetate films or for porous strips.

Despite the fact that the predicted transverse permeability values were different for the two methods, they were both used in the FLUENT simulation model in place of the porous strip permeability that was modeled using the "porous jump" boundary condition. The simulation results showed that no significant differences in the flow patterns were observed when the measured versus calculated strip permeability values were used to simulate the infiltration processes where the transverse flow dominated over the in-plane flow. This was proved to be true for the hybrid preforms with flow pathways of 0.83 mm and 1.59 mm diameters. As for the preforms with flow pathways of 0.41 mm diameter, where the in-plane flow was dominant, differences were observed between the simulated cases using the measured versus calculated strip permeability values. It was shown that the transverse permeability of the distribution media had the most significant impact on the simulation model results.

It was also seen that the simulations of the CAPRI/FML process showed a closer match with the experimental flow patterns and the infiltration times when compared with the VARTM process simulations. This could be due to the preform being kept at less than full vacuum conditions in the CAPRI process and thus allowing for longer infiltration times.

The developed flow simulation model was able to capture the shape of the flow patterns and predict the progression of the flow front reasonably well for most cases. However, in some cases

there were differences in the absolute times due to the two phase nature of the model and the simplified approach used to model the flow through the acetate films by porous strips. Finally, it was shown that further improvements in the simulation model can be made by the addition of a compaction model that is capable of dynamically updating the permeability and thickness with time, and capable of choosing the correct preform compaction equations depending on the wet or dry status of the preform.

In conclusion, the results of this study proved the feasibility of fabricating high quality FML parts using the VARTM and CAPRI processes when flow pathways were included in the hybrid preform structure. This study also demonstrated the complexity of the infiltration process of the FML structures during the VARTM and CAPRI processes.

The developed model is useful in modeling hybrid preform structures with a reduced computational cost and has the flexibility of modeling multi layered parts with any desired configuration and properties. The model can be used as a computational tool for the manufacturing process development of FMLs. This study is expected to be especially useful in modeling large sized hybrid aerospace structures for improved fiber volume fractions and uniform part thicknesses.

7.2 Future Work

Although the predicted transverse permeability value for the distribution media agrees well with the data available in literature, there was no data available for the acetate films. Thus, a direct permeability measurement technique for highly porous media such as the distribution media and the acetate films with large flow pathways could be developed by using a different transverse permeability fixture and possibly by using pressure transducers than can detect very small pressure changes. By this way, the errors associated with the assumptions made during the hybrid permeability calculations could be eliminated.

During the flow visualization tests, further enhancements of the processing conditions can be done such as regarding the issues of preform lay-up that affects race-tracking and flow pathway alignment, better visualization of the fixture by possibly using two cameras rather than one and better visualization of the testing fluid by improving the lighting conditions or by using a darker colored testing fluid and keeping the vacuum levels similar in each test of the same type.

Although the infiltration test results during the manufacture of an actual FML panel was acquired and used for comparison purposes, an actual FML part was not manufactured in this study. The manufacture of an FML part can be performed with the available resources and studies for mechanical testing and laminate quality should be performed. Resin characterization studies can also be done using low-viscosity polyimide resin systems that are suitable for VARTM/CAPRI FML processes. Cure kinetics and rheology characteristics should be measured and fit to mathematical models.

The multiphase VOF model gave satisfactory results in most cases. However, the physics of the model included air in the domain throughout the flow calculations although very minimal or no air existed in the actual processes. This is the limitation of the VOF model in modeling liquid composite molding processes in which vacuum is introduced. The VOF model could be better suited for processes like Resin Transfer Molding (RTM). The predicted flow patterns at the intermediate time frames compared reasonably well with the experimental observations, however the predicted total infiltration times were significantly higher than measured. This is possibly due to the higher period of time required to displace all the air inside the preform in the simulated cases. Further research can be done on how to modify the VOF model to handle situations where the interface between the vacuum and the resin needs to be modeled so that the advancement of resin can be monitored more accurately.

As noted before, the generated contour plots for the volume fraction of the resin displays the colors between red and blue corresponding to the volume fractions of 1 and 0, respectively. This means that the colors in between these two colors represent other volume fractions. For instance, the color green represents a volume fraction of about 0.5 and the color yellow represents a volume fraction of about 0.75. Looking at the flow patterns captured during the flow visualization tests, it is very hard to make this distinction in volume fractions. When the resin arrives at a certain position, it is interpreted as completely filled or a volume fraction of 1 although it might actually have a lower volume fraction such as 0.75. Thus, when comparing the flow patterns predicted by the simulation model with the flow patterns observed during flow visualization tests, the comparisons shouldn’t be mainly based on the color red or blue. An alternative approach could be lowering the default volume fraction value of 0.95 for the color red

displayed in the contour plots. Lowering it to 0.80 for instance would make the contour plots display the color red sooner when the compared with the plots with the default value of 0.95. By this way, the infiltration process can be viewed as progressing faster and the simulated infiltration times would be reduced.

VITA

GÖKER TUNÇOL was born in İzmir, Turkey on September 25, 1980. He received his B.Sc. degree in Mechanical Engineering from Middle East Technical University (METU), Ankara, Turkey, in 2003. During his B.S. degree, he and his teammate constructed a line tracking robot and received 3 awards for: Best Overall Design, Best prediction and a 3rd place among 15 projects in the Mechanical Engineering Design Competition held on January 23, 2003 at Middle East Technical University in association with Queens University, Canada. He had his M.Sc. degree in Mechanical Engineering from Koc University, Istanbul, Turkey in 2005. Since 2005, he has enrolled to the Ph.D. program in Mechanical Engineering at Michigan State Univeristy as a teaching and research assistant. He has been studying in the "Modeling the Vacuum Assisted Resin Transfer Molding (VARTM) Process for Fabrication of Fiber/Metal Hybrid Laminates" project since then. He and his coworkers published two articles at the Journal of Composites Science and Technology and at the Journal of Composites Part A: Applied Science and Manufacturing, in 2007. He likes to play tennis and have a good time with the loved ones in his spare time. He frequently misses the Bosphorus and the heavenly beautiful Aegean region.

APPENDICES

APPENDIX A

Please note the change in nomenclature for this section of the Appendix as follows:

u: volume averaged velocity

μ : viscosity of the fluid

∇P : pressure gradient vector

K: permeability tensor of the preform which can be written as:

Fully Developed Circular Pipe Flow and Equivalent Permeability

By deriving an analytical equivalent permeability expression for a circular pipe, the validity of this method can be further tested. One of the classical flow problems is considered here: Poiseuille flow where fluid flows through a circular channel due to a longitudinal pressure gradient as shown in Figure A.1.

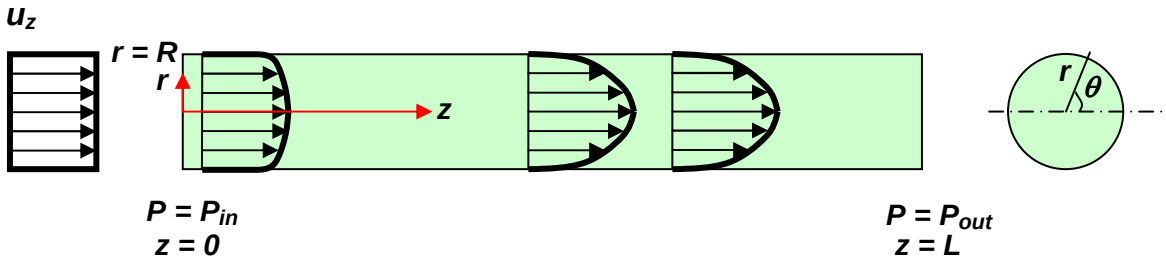

Figure A.1 Poiseuille flow: pressure driven circular pipe flow.

Assumptions:

- Incompressible: $\rho = \text{constant}$
- Fully-developed flow: $\frac{\partial u}{\partial z} = 0$
- No body forces ($F_B = 0$).
- Quasi-steady flow: $\frac{\partial u}{\partial t} = 0$
- Axisymmetric: $\frac{\partial u}{\partial \theta} = 0$, $u_\theta = 0$

Boundary Conditions:

$$u_r(r = R) = 0, \quad u_z(r = R) = 0, \quad P(z = 0) = P_{in}, \quad P(z = L) = P_{out}.$$

Continuity Equation:

$$\frac{1}{r}\frac{\partial (r u_r)}{\partial r} + \frac{1}{r}\frac{\partial u_\theta}{\partial \theta} + \frac{\partial u_z}{\partial z} = 0$$

$$\frac{1}{r}\frac{\partial (r u_r)}{\partial r} = 0 \Rightarrow \quad r u_r \neq f(r) \Rightarrow \quad r u_r = c_1 \Rightarrow \quad u_r = \frac{c_1}{r}$$

$$\Rightarrow \quad u_r(R) = 0 = \frac{c_1}{R} \Rightarrow \quad c_1 = 0 \quad \textit{and} \quad u_r = 0 \quad \textit{for all r values.} \tag{A.1}$$

Momentum Equation in r direction:

$$\rho\left[\frac{\partial u_r}{\partial t} + u_r\frac{\partial u_r}{\partial r} + \frac{u_\theta}{r}\frac{\partial u_r}{\partial \theta} - \frac{u_\theta^2}{r} + u_z\frac{\partial u_r}{\partial z}\right] =$$

$$-\frac{\partial P}{\partial r} + \mu\left[\frac{\partial}{\partial r}\left[\frac{1}{r}\frac{\partial (r u_r)}{\partial r}\right] + \frac{1}{r^2}\frac{\partial^2 u_r}{\partial \theta^2} + \frac{\partial^2 u_r}{\partial z^2} - \frac{2}{r^2}\frac{\partial u_\theta}{\partial \theta}\right] + F_{Br}$$

$$\Rightarrow \quad -\frac{\partial P}{\partial r} = 0 \Rightarrow \quad P \neq P(r) \Rightarrow \quad P = P(z). \tag{A.2}$$

Momentum Equation in z direction:

$$\rho\left[\frac{\partial u_z}{\partial t} + u_r\frac{\partial u_z}{\partial r} + \frac{u_\theta}{r}\frac{\partial u_z}{\partial \theta} + u_z\frac{\partial u_z}{\partial z}\right] = -\frac{\partial P}{\partial z} + \mu\left[\frac{1}{r}\frac{\partial}{\partial r}\left[r\frac{\partial u_z}{\partial r}\right] + \frac{1}{r^2}\frac{\partial^2 u_z}{\partial \theta^2} + \frac{\partial^2 u_z}{\partial z^2}\right] + F_{Bz}$$

$$\Rightarrow \qquad \frac{\partial P}{\partial z} = \mu \frac{1}{r}\frac{\partial}{\partial r}\left[r\frac{\partial u_z}{\partial r} \right].$$

Left side is a function of *z*, and right side is function of *r*. For this equality to hold:

$$\frac{\partial P}{\partial z} = \mu \frac{1}{r}\frac{\partial}{\partial r}\left[r\frac{\partial u_z}{\partial r} \right] = \text{constant}, \quad \text{which implies: } \frac{\partial P}{\partial z} = \frac{dP}{dz} = \frac{P_{out} - P_{in}}{L}$$

$$\Rightarrow \qquad \mu \frac{1}{r}\frac{\partial}{\partial r}\left[r\frac{\partial u_z}{\partial r} \right] = \frac{P_{out} - P_{in}}{L} \tag{A.3}$$

Using the boundary condition, $u_r(r = R) = 0$, and solving for $u_z(r)$:

$$u_z(r) = \frac{P_{out} - P_{in}}{4\mu L}\left(r^2 - R^2 \right) \quad \text{and} \quad u_{z,\max} = u_z(r = 0) = -\frac{P_{out} - P_{in}}{4\mu L} R^2 . \tag{A.4}$$

Volumetric flow rate:

$$\dot{Q} = \int_A u_z dA = \int_0^R u_z 2\pi r dr = \int_0^R \frac{P_{out} - P_{in}}{4\mu L}\left(r^2 - R^2 \right) 2\pi r dr$$

$$\Rightarrow \qquad \dot{Q} = -\frac{\pi\left(P_{out} - P_{in} \right)}{8\mu L} R^4 . \tag{A.5}$$

Mean (Average) Velocity:

$$u_{z,mean} = \frac{\dot{Q}}{A} = \frac{-\frac{\pi\left(P_{out} - P_{in} \right)}{8\mu L} R^4}{\pi R^2} = -\frac{\left(P_{out} - P_{in} \right)}{8\mu L} R^2 = \frac{dP}{dx}\frac{R^2}{8\mu} . \tag{A.6}$$

Using Darcy's Law:

$$u = -\frac{K}{\mu}\frac{dP}{dx} \ , \ \frac{dP}{dx}\frac{R^2}{8\mu} = -\frac{K}{\mu}\frac{dP}{dx} \qquad \Rightarrow K = \frac{R^2}{8} \text{ for a pipe with circular cross-section.} \tag{A.7}$$

APPENDIX B

Calculation of entrance length L_e :

For laminar flow, the entrance length L_e for a cylindrical hole can be found by:

$$\frac{L_e}{d} = 0.06\, R_e \tag{B.1}$$

where R_e is the Reynold's number based on hole diameter.

$$R_e = \frac{\rho V L}{\mu} \tag{B.2}$$

where ρ is the fluid density, V is the mean flow velocity, L is the hole diameter and μ is the dynamic fluid viscosity. In this study, ρ = 790 kg/m^3, μ =0.24 Pa.s, L=0.41, 0.83, 1.59 mm. For fully developed conditions to hold, L_e should be much smaller than the hole length which is equal to the the acetate film thickness used in this study. Considering the largest hole diameter of 1.59 mm and plugging in all the values, the entrance length was found as a function of the mean velocity as follows:

$$L_e = 4.48\text{e-}4\, V \tag{B.3}$$

The value of the mean velocity V during the permeability measurement tests of the acetate films with the 1.59 mm diameter was 0.0105 m/s based on the flow rate of 8.33e-8 m^3/s. Plugging the mean velocity in Equation B.3 gives:

L_e = 4.7e-6 m and the acetate film thickness was 3.82e-4 m.

Thus, L_e << 3.82 e-4 m !!!

If the calculation above is repeated for the 0.41 mm hole diameter, it was found that:

$$L_e = 2.97 \text{ e-5 } V \quad \text{(B.4)}$$

The value of the mean velocity V during the permeability measurement tests of the acetate films with the 0.41 mm diameter was 0.38 m/s based on the flow rate of 2.0e-7 m^3/s. Plugging the mean velocity in Equation B.4 gives:

L_e = 1.13e-5 m and the acetate film thickness was 3.82e-4 m.

Thus, L_e<< 3.82 e-4 m !!!

Having considered the largest and smallest hole diameters, it can be concluded that the flow is laminar and fully developed, and thus Hagen–Poiseulle relations hold.

APPENDIX C

The UDF program codes of the integrated compaction model discussed in Section 6.5 are given here. There are three program codes: one for every principal direction x, y and z. The programming language used was C. Viscous resistance is reciprocal of permeability.

/* Viscous Resistance Profile UDF in a Porous Zone, X direction */

```
#include "udf.h"
#include <math.h>
DEFINE_PROFILE(vis_res,t,i)
{ real x[ND_ND];
  real p1, va, vb, vc, vk, vm, vn, e, e2, vf0, vf02, sax, sbx, vf, vf2;
  cell_t c;
  va=-0.0165; vb=0.3521; vc=8.970; vk=0.0828; vm=0.3678; vn=29.6068;
  vf0=0.48; vf02=0.58;
  sax= 3.58e-9; sbx= -8;
  begin_c_loop(c,t) {
   p1=(101325.00-C_P(c,t))/1000.00;
if (THREAD_ID(t)==1&& C_VOF(c,t)>=0.95)
   { e=va+vb*(p1/(vc+p1));
   vf=vf0/(1-e);
   F_PROFILE(c,t,i) =1/(sax*exp(vf*sbx)); }
else
   { e2=vk+vm*(p1/(vn+p1));
   vf2=vf02/(1-e2);
   F_PROFILE(c,t,i) =1/(sax*exp(vf2*sbx)); } }
  end_c_loop(c,t) }
```

/* Viscous Resistance Profile UDF in a Porous Zone, Y direction */

```
#include "udf.h"
#include <math.h>
DEFINE_PROFILE(vis_res,t,i)
{ real x[ND_ND];
  real p1, va, vb, vc, vk, vm, vn, e, e2, vf0, vf02, say, sby, vf, vf2;
  cell_t c;
  va=-0.0165; vb=0.3521; vc=8.970; vk=0.0828; vm=0.3678; vn=29.6068;
  vf0=0.48; vf02=0.58;
say= 4.03e-9; sby= -7.77;
begin_c_loop(c,t) {
   p1=(101325.00-C_P(c,t))/1000.00;
if (THREAD_ID(t)==1&& C_VOF(c,t)>=0.95)
   { e=va+vb*(p1/(vc+p1));
   vf=vf0/(1-e);
   F_PROFILE(c,t,i) =1/(say*exp(vf*sby)); }
else
   { e2=vk+vm*(p1/(vn+p1));
   vf2=vf02/(1-e2);
   F_PROFILE(c,t,i) =1/(say*exp(vf2*sby)); } }
  end_c_loop(c,t) }
```

/* Viscous Resistance Profile UDF in a Porous Zone, Z direction */

```
#include "udf.h"
#include <math.h>
DEFINE_PROFILE(vis_res,t,i)
{ real x[ND_ND];
  real p1, va, vb, vc, vk, vm, vn, e, e2, vf0, vf02, saz, sbz, vf, vf2;
  cell_t c;
  va=-0.0165; vb=0.3521; vc=8.970; vk=0.0828; vm=0.3678; vn=29.6068;
  vf0=0.48; vf02=0.58;
saz= 8.57e-11; sbz= -8.78;
begin_c_loop(c,t) {
   p1=(101325.00-C_P(c,t))/1000.00;
if (THREAD_ID(t)==1&& C_VOF(c,t)>=0.95)
   { e=va+vb*(p1/(vc+p1));
   vf=vf0/(1-e);
   F_PROFILE(c,t,i) =1/(saz*exp(vf*sbz)); }
else
   { e2=vk+vm*(p1/(vn+p1));
   vf2=vf02/(1-e2);
   F_PROFILE(c,t,i) =1/(saz*exp(vf2*sbz)); } }
  end_c_loop(c,t) }
```

BIBLIOGRAPHY

BIBLIOGRAPHY

1. Vlot, A., L. B. Vogelesang and T. J. de Vires, "Fiber Metal Laminates for High Capacity Aircraft," Proceeding of 30th International SAMPE Techinical Conference, SAMPE, Corvina, CA, pp.456, 1998.

2. Miller J.L., Progar D.J., Johnson W.S., "Preliminary Evaluation of Hybrid Titanium Composite Laminates", Journal of Adhesion, 54(1-2), 223-240, 1995.

3. From the official website of AIRBUS SAS, http://www.airbus.com/en/A380.

4. A. C. Loos, R. J. Cano, B. J. Jensen, E. S. Weiser, "Manufacture of Layered Fiber/Metal Hybrid Composites by the VARTM Process".

5. Jensen, B. J., R. J. Cano, S. J. Hales, J. A. Alexa and E. S. Weiser, "Fabrication of Fiber Metal Laminates by Non-Autoclave Processes," in *CD proceedings of NASA Fundamental Aeronautics 2007 Annual Meeting, October 30 – November 1, 2007*, New Orleans, LA, NASA, Washington, DC, (2007).

6. Jensen, B.J., Cano, R.J., Hales, S.J., Alexa, J.A. and Weiser, E.S., "Fabrication of Fiber Metal Laminates by Non-Autoclave Processes," SAMPE Technical Conference, June 5–7, 2007, Baltimore, MD, (2007).

7. Seemann, W.H., "Plastic Transfer Molding Techniques for the Production of Fiber Reinforced Plastic Structures," U.S. Patent 4,902,215.

8. Seemann, W.H., "Unitary Vacuum Bag For Forming Fiber Reinforced Composite Articles," U.S. Patent 5,316,462, 1994.

9. S.G. Advani and E.M. Sozer, "Process modeling in Composites Manufacturing", New York, Marcel Dekker, Inc., Chapter 2: Overview of Manufacturing Processes, Part 5.2: Liquid Composite Molding, pp 49, 2003.

10. Senibi, S., R.L. Sadler, and V. S. Avva, "Resin Transfer Molding (RTM): Experiments with Vacuum Assisted Methods," Proceedings of 46th International SAMPE Techinical Conference, SAMPE, Corvina, CA, pp.1049, 1995.

11. Nguyen, L. B., T. Juska and S. J Mayes, "Evaluation of Low Cost Manufacturing Technologies for Large Scale Composite Ship Structures," Proceedings of the AIAA/ASME/ASCE/AHS/ASC Structures, Structural Dynamics, and Materials Conference, 38, 992, 1997.

12. Lewit, S .M. and J. C. Jakubowski, “Low Cost VARTM Process for Commercial and Military Applications,” Proceedings of the 42nd SAMPE International Symposium, pp. 1173, 1997

13. Thomas, L. R., A. K. Miller and A. L. Chan. “Fabrication of Complex High-Performance Composite Structures at Low Cost using VARTM,” Proceedings of the 47th SAMPE International Symposium, 570, 2002.

14. R.J. Johnson and R. Pitchumani, “Active Control of Reactive Resin Flow in a Vacuum Assisted Resin Transfer Molding (VARTM) Process”, Journal of Composite Materials, 42(12), 1205-1229, 2008.

15. Correia, F. Robitaille, A. C. Long, C. D. Rudd, P. Simacek, S. G. Advani, “Use of Resin Transfer Molding Simulation to Predict Flow, Saturation, and Compaction in the VARTM Process”, Transactions of the ASME, 26, 210-215, 2004.

16. P. Simacek and Suresh G. Advani, “Desirable Features in Mold Filling Simulations for Liquid Composite Molding Processes”, Polymer Composites, 25 (4), 355-367, 2004.

17. R. Chen, C. Dong, Z. Liang, C. Zhang, B. Wang, “Flow Modeling and Simulation for Vacuum Assisted Resin Transfer Molding Process with the Equivalent Permeability Method”, Polymer Composites, 25(2), 146-164, 2004.

18. Chensong (Jonathan) Dong, “Development of a Process Model for the Vacuum Assisted Resin Transfer Molding Simulation by the Response Surface Method”, Composites, Part A 37, 1316–1324, 2006.

19. M. Grujicica, K.M. Chittajallua, S. Walsh, “Non-isothermal Preform Infiltration during the Vacuum-Assisted Resin Transfer Molding (VARTM) Process”, Applied Surface Science 245, 51–64, 2005.

20. J. Li, C. Zhang, R. Liang, B. Wang, S. Walsh, “Modeling and Analysis of Thickness Gradient and Variations in Vacuum-Assisted Resin Transfer Molding Process” Polymer Composites, 473-482, 2008.

21. Y.S. Song, J.R. Youn “Modeling of Resin Infusion in Vacuum Assisted Resin Transfer Molding”, Polymer Composites, 391-395, 2008.

22. M.K. Yoon and D.F. Dolan, “Homogenous Modeling of VARTM Processes with Hybrid Layered Media”, Journal of Composite Materials, 42(8), 805-824, 2008.

23. Q. Govignon, S. Bickerton, P.A. Kelly, “Simulation of the reinforcement compaction and resin flow during the complete resin infusion process”, Composites Part A 41, 45–57, 2010.

24. Robitaille F, Gauvin R., “Compaction of textile reinforcements for composites manufacturing. II: Compaction and relaxation of dry and H_2O saturated woven reinforcements”, Polymer Composites 19, 543–57, 1998.

25. Z. Cai and T. G. Gutowski, “The 3D Deformation Behavior of a Lubricated Fiber Bundle”, Composite Materials, 26(8), 1207- 1237, 1992.

26. T.G. Gutowski and G. Dillon, “The Elastic Deformation of Lubricated Carbon Fiber Bundles: Comparison of Theory and Experiments”, Composite Materials, 26(16), 2330-2347, 1992.

27. T.G. Gutowski, Z. Cai, S. Bauer, D. Boucher, J. Kingery, and S. Wineman, “Consolidation Experiments for Laminate Composites”, Composite Materials, 21(7), 650-669, 1987.

28. T.G. Gutowski, T. Morigaki, Z. Cai, “The consolidation of laminate composites”, Composite Materials, 21,172–88, 1987.

29. Min Li, Yizhuo Gu, Zuoguang Zhang, Zhijie Sun, “A Simple Method for the Measurement of Compaction and Corresponding Transverse Permeability of Composite Prepregs”, Polymer Composites, 2007.

30. P. Hubert, A. Poursartip, “A method for the direct measurement of the fibre bed compaction curve of composite prepregs”, Composites: Part A 32, 179–187, 2001.

31. M. Schuster, A. Ogale, L. Peetz, J. Schuster, P. Mitschang, “Analysis of sewed preforms by visual on-line monitoring of stitch-hole variations under compaction”, Composites Science and Technology 68, 312–320, 2008.

32. M.J. Buntain, S. Bickerton, “Modeling forces generated within rigid liquid composite molding tools. Part A: Experimental study”, Composites: Part A 38, 1729–1741, 2007.

33. S. Bickerton, M.J. Buntain, “Modeling forces generated within rigid liquid composite molding tools. Part B: Numerical analysis”, Composites: Part A 38, 1742–1754, 2007.

34. P.A. Kelly, R. Umer, S. Bickerton, “Viscoelastic response of dry and wet fibrous materials during infusion processes”, Composites: Part A 37, 868–873, 2006.
35. A.A. Somashekar, S. Bickerton, D. Bhattacharyya, “Exploring the non-elastic compression deformation of dry glass fiber reinforcements”, Composites Science and Technology 67, 183–200, 2007.

36. Baoxing Chen, Eric J. Lang, Tsu-Wei Chou, “Experimental and theoretical studies of fabric compaction behavior in resin transfer molding”, Materials Science and Engineering A317, 188–196, 2001.

37. Teresa Kruckenberg, Lin Ye, Rowan Paton, “Static and vibration compaction and microstructure analysis on plain-woven textile fabrics”, Composites Part A 39 488–502, 2008.

38. Andersson HM, Lundstrom TS, Gebart BR, Synnergren P. “Application of digital speckle photography to measure thickness variations in the vacuum infusion process”, Polymer Composites, 24(3):448–55, 2003.

39. B. Yenilmez, M. Senan, E. M. Sozer, “Variation of part thickness and compaction pressure in vacuum infusion process”, Composites Science and Technology 69, 1710–1719, 2009.

40. T. Wang, C. H. Wu, L. J. Lee, “In-plane permeability measurement and analysis in Liquid Composite Molding”, Polymer Composites, 15(4), 278-288, 1994.

41. T. Wang, C. H. Wu, L. J. Lee, “Trans-plane permeability measurement and its applications in Liquid Composite Molding”, Polymer Composites, 15(4), 289-298, 1994.
42. Darcy, H., Lesfontaines publiques delavillede, 1856.

43. A.W. Chan, D.E. Larive, R.J. Morgan, “Anisotropic Permeability of Fiber Preforms: Constant Flow Rate Measurement”, Journal of Composite Materials, 27(10), 996-1008, 1993.

44. R.S. Parnas, J.G. Howard, T.L. Luce, S.G. Advani, “Permeability Characterization. Part 1: A proposed Standard Reference Fabric for Permeability”, Polymer Composites, 16(6), 429-445, 1995.

45. R. Gauvin, F. Trochu, Y. Lemenn, L. Diallo, “Permeability Measurement and Flow Simulation through Fiber Reinforcement”, Polymer Composites, 17(1), 34-42, 1996.

46. A. Hammami, “Key Factors Affecting Permeability Measurement in the Vacuum Infusion Molding Process”, Polymer Composites, 23(6), 1057-1067, 2002.

47. L. Ding, C. Shih, Z. Liang, C. Zhang, B. Wang “In situ measurement and monitoring of whole-field permeability profile of fiber preform for liquid composite molding processes”, Composites Part A(34), 779-789, 2002.

48. S. Drapier, J. Monatte, O. Elbouazzaoui, P. Henrat, “Characterization of transient through thickness permeabilities of non crimp new concept (NC2) multi-axial fabrics”, Composites Part A(36), 877-892, 2005.

49. A. Gokce, M. Chohra, S.G. Advani, S. M. Walsh, “Permeability estimation algorithm to simultaneously characterize the distribution media and the fabric preform in VARTM”, Composites Science and Technology, 65, 2129-2139, 2005.

50. H. Talvensaari, E. Ladstatter, W. Billinger, “Permeability of stitched preform packages”, Composite Structures, 71, 371-377, 2005.

51. M. Nordlund, T.S. Lundstrom, V. Frishfelds, A. Jakovics, “Permeability Network Model for Non-Crimp Fabrics”, Composites Part A(37), 826-835, 2006.

52. C. Dong, “A Fast Permeability Measurement Method Based On Hybrid Fiber Preforms”, ASME 127, 670-676, 2005.

53. Y.J. Lee, J.H. Wu, Y. Hsu, C.H. Chung, “A Prediction Method on In-Plane Permeability of Mat/Roving Fibers Laminates In VARTM”, Polymer Composites, 665-670, 2006.

54. A. Endruweit, L.T. Harper, T.A. Turner, N.A. Warrior, A.C. Long, “Random Discontinuous Carbon Fiber Preforms: Experimental Permeability Characterization and Local Modeling”, Polymer Composites, 570-580, 2010.

55. C. Niggemann, Y. S. Song, J. W. Gillespie and D. Heider, “Experimental Investigation of the Controlled Atmospheric Pressure Resin Infusion (CAPRI) Process”, Journal of Composite Materials, 42(11), 1049-1061, 2008.

56. Williams D. C., Grove M. S. and J. Summerscales, “The Compression Response of Fiber-Reinforced Plastic (FRP) Plates during Manufacture by the Resin Infusion under Flexible Tooling (RIFT) method,” Composites: Part A, Vol. 29A, 111-114, 1998.

57. R.A. Saunders, C. Lekakou, M.G. Bader, “Compression in the processing of polymer composites, 1. A mechanical and microstructural study for different glass fabrics and resins”, Composites Science and Technology 59, 983-993, 1999.

58. R.A. Saunders, C. Lekakou, M.G. Bader, “Compression in the processing of polymer composites, II. Modelling of the viscoelastic compression of resin-impregnated fibre networks”, Composites Science and Technology 59, 1483-1494, 1999.
59. R. A. Saunders, C. Lekakou and M. G. Bader, “Compression and microstructure of fibre plain woven cloths in the processing of polymer composites”, Composites Part A 29A, 443-454, 1998.

60. Nell Pearce and John Summerscales, “The compressibility of a reinforcement fabric”, Composites Manufacturing 6, 15-21, 1995.

61. Rigas J. E., T. J. Mulkern, S. M. Walsh, and S. P. Nguyen, “Effects of Processing Conditions on Vacuum Assisted Resin Transfer Molding Process (VARTM),” Army Research Laboratory Report ARL-TR-2480, 2001.

62. Brian W. Grimsley, Pascal Hubert, Xiaolan Song, Roberto J. Cano, Alfred C. Loos, and R. Byron Pipes, “Flow and Compaction during the Vacuum Assisted Resin Transfer Molding Process,” Proceedings of 33rd International SAMPE Technical Conference, SAMPE, Corvina, CA, 140 -153, 2001.

63. Grimsley, B.W., Cano R.J., Hubert, P., Loos, A.C., Kellen C.B. and Jensen, B.J., “Preform characterization in VARTM process model development,” In: CD Proceedings of 36th International SAMPE Technical Conference, SAMPE, Corvina, CA, 14, 2004.

64. Govignon, Q., S. Bickerton, et al. "Full field monitoring of the resin flow and laminate properties during the resin infusion process." Composites Part a-Applied Science and Manufacturing 39(9), 1412-1426, 2008.

65. Dave R., J. L. Kardos, and M. P. Dudukovic, “A Model for Resin Flow during Composite Processing: Part 1 General Mathematical Development,” Polymer Composites, 8(29), 1987.

66. Hammami A. and B. R. Gebart, “Analysis of the Vacuum Infusion Molding Process,” Polymer Composites, 21(1), 28-40, 2000.

67. Grimsley, B. W. December 2005. “Characterization of the Vacuum Assisted Resin Transfer Molding Process for Fabrication of Aerospace Composites,” M. S. Thesis, Department of Materials Science and Engineering, Virginia Polytechnic Institute and State University, Blacksburg, VA.

68. P. Ouagne, J. Breard, “Continuous Transverse Permeability of Fibrous Media”, Composites: Part A 41, 22–28, 2010.

69. Ali Gokce, Mourad Chohra, Suresh G. Advani, Shawn M. Walsh, “Permeability Estimation Algorithm to Simultaneously Characterize The Distribution Media and The Fabric Preform in Vacuum Assisted Resin Transfer Molding Process”, Composites Science and Technology 65, 2129–2139, 2005.
70. Song, X. “Vacuum Assisted Resin Transfer Molding (VARTM): Model Development and Verification,” Ph.D. Dissertation, Department of Engineering Science and Mechanics, Virginia Polytechnic Institute and State University, Blacksburg, VA, 2003.

71. Fluent 6.3 User’s Guide, 23.3.1 Overview and Limitations of the VOF Model, Ansys Inc., http://my.fit.edu/itresources/manuals/ fluent6.3 /help / html/ ug/ node 881.htm.

72. Y. Kuan and A. S. Gizawy, “Numerical Characterization of Mold Injection in Resin Transfer Molding Process”, Advances in Polymer Technology, 19(3), 173–179 2000.

73. Fluent 6.3 User’s Guide, Defining Phases for the VOF Model, http://jullio.pe.kr /fluent6.1/help/html/ug/node772.htm.

74. Fluent 6.3 User’s Guide, 7.22 Porous Jump Boundary Conditions, http://my.fit. edu/itresources/manuals/fluent 6.3 /help/html/ug/node288.htm.

75. Fluent 6.3 User’s Guide for User Defined Functions (UDF), http://my.fit.edu/ itresources/manuals/fluent6.3/help/html/udf/main_pre.htm.

76. Tonmoy Roy, Hua Tan and Krishna M. Pillai, “A Method to Estimate the Accuracy of 1-D Flow Based Permeability Measuring Devices”, Journal of Composite Materials, Vol. 41, 2037-2055, 2007.

77. Tuncol G., “Monitoring of Resin Flow and Cure in Resin Transfer Molding (RTM) Process,” M.S. Thesis, Chapter 6: Calculation of the Equivalent Permeability of Race-tracking Channels using Stokes Flow Model and Finite Difference Method, Department of Mechanical Engineering, Koc University, Istanbul, Turkey 2005.